

**Search for a Higgs boson in the $H \rightarrow ZZ$
and $ZH \rightarrow ll + \text{invisible}$ channels with the ATLAS detector**

Thesis submitted in accordance with the requirements of
the University of Liverpool for the degree of Doctor in Philosophy

by

Joseph Price

April 2013



Abstract

A pre-data sensitivity study to search for a high mass Standard Model (SM) Higgs ($m_H = 200$ GeV) in ATLAS using the $H \rightarrow ZZ \rightarrow lll$ channel is presented. It is found that it would be possible to exclude a SM Higgs in part of this high mass region with limited luminosity. Using this channel a search at the LHC for the SM Higgs boson in the first ~ 40 pb $^{-1}$ of data was conducted and is presented in this thesis, along with the results from the $H \rightarrow ZZ \rightarrow ll\nu\nu$ and $H \rightarrow ZZ \rightarrow llqq$ channels using a similar dataset [1]. It is found that the channel with the best sensitivity to a SM Higgs with mass greater than 200 GeV is the $H \rightarrow ZZ \rightarrow ll\nu\nu$ channel.

A search for the SM Higgs boson using the $H \rightarrow ZZ \rightarrow ll\nu\nu$ channel is presented, using 4.7 fb $^{-1}$ of data at a centre-of-mass energy of $\sqrt{s} = 7$ TeV. A Higgs boson with a mass between 320 and 560 GeV is excluded at a 95% confidence level using this channel alone. This analysis was published in 2011 and updated in 2012 [2, 3], and results from this search are used in the ATLAS paper [4], describing the discovery of a new Higgs-like boson with $\sim m_H = 125$ GeV.

Finally a direct search is performed for anomalous invisible decays of the Higgs boson candidate at ~ 125 GeV using both the 4.7 fb $^{-1}$ 2011 dataset and the 13 fb $^{-1}$ 2012 dataset at centre-of-mass energy $\sqrt{s} = 7$ and 8 TeV respectively. An upper limit of 65% is set on the allowed $H \rightarrow inv$ branching fraction at 95% confidence level. Additional searches are performed using the same dataset on further invisibly decaying Higgs-like bosons at masses between 115 and 300 GeV. No excess is observed. This analysis was published as a preliminary result in March 2013 [5], and a paper using the full 2011 and 2012 datasets is scheduled to be published in the summer of 2013.

Acknowledgements

I would firstly like to thank all of the staff and students at the HEP group at Liverpool University. In particular I would like to thank Joost Vosseveld, who has been exceptional in everything over the last 4 years. Special thanks also to Carl Gwilliam, for teaching me how to code from scratch, and to Andrew Mehta for his advice on all things physics. Thanks for putting up with my questions. Thanks also to the computing staff at Liverpool for their technical support.

I would like to thank the STFC and the ATLAS experiment for allowing me such a wonderful opportunity, and all my colleagues on ATLAS with whom I have worked, particularly the people in the HSG2 working group who have always lended me their full support; German, Kostas, Hongtao, Hideki, Andy, Josh and Lailin. Thanks to Dr. A. Webber, Dr. T. Proctor, Josh, Dr. W. Martin, Ed, Joel, Nick, Kara and Sarah for putting up with me whilst I was at CERN. Thanks also to the CERN cricket club and whoever put a snooker table in building 565.

I would like to thank the staff at Cardiff University, especially Prof. P. Mauskopf and Prof. P. Coles for their lectures and for their help with my PhD application. I would also like to thank all of my friends at Cardiff who made studying there such an enjoyable experience; particularly Alec, Pat, Ro, Charlotte, Steve, Gav, Matt, Tom and Adam. Even James.

Finally I would like to thank my friends back home; Blackie, Oli, Alex (a.k.a the cheif), Sully, Lisa and Amanda (and all the rest), and mostly my Mum, Dad and Brother for their continuous support and advice. Thank you.

Contents

1	Introduction	7
2	Theory	8
2.1	Introduction to the Standard Model	8
2.1.1	Fermions	8
2.1.2	Bosons	9
2.1.3	Particle summary	9
2.2	Electro-weak theory	10
2.2.1	Masses in the Standard Model	10
2.2.2	Particle interactions	11
2.3	The Higgs mechanism	14
2.3.1	Spontaneous symmetry breaking	14
2.3.2	Spontaneous breaking of a global U(1) symmetry	15
2.3.3	Spontaneous breaking of a local U(1) symmetry	16
2.3.4	Spontaneous breaking of SU(2) symmetry	18
2.3.5	Masses of the electro-weak bosons	19
2.4	Searches for the Higgs boson	20
2.4.1	SM Higgs production at the LHC	21
2.5	Beyond the Standard Model	23
2.5.1	The hierarchy problem	23
2.5.2	Neutrino masses	23
2.6	Dark matter and the Higgs boson	24
2.7	Supersymmetry	24
3	The ATLAS Detector	25
3.1	The Large Hadron Collider	25
3.2	The aims of the ATLAS experiment	26
3.3	Co-ordinate system and units	27
3.4	Detector overview	27
3.5	Inner Detector	29
3.5.1	Pixel detector	31
3.5.2	Silicon Tracker (SCT)	31

3.5.3	Transition Radiation Tracker (TRT)	32
3.5.4	Inner detector performance	32
3.6	Calorimeters	32
3.6.1	Electro-magnetic calorimeters	34
3.6.2	Hadronic calorimeters	36
3.6.3	Calorimeters summary	36
3.7	Muon spectrometer	37
3.8	Triggers	39
3.9	Luminosity	40
3.10	Summary	41
4	Reconstruction	42
4.1	Data	42
4.1.1	The 2010 dataset	43
4.1.2	The 2011 dataset	44
4.1.3	The 2012 dataset	45
4.1.4	Pileup	46
4.2	Muons	46
4.3	Electrons	47
4.4	Jets	52
4.4.1	b -Jets	52
4.5	Overlap removal	54
4.6	Missing transverse energy	54
5	Search for the SM Higgs boson in the $H \rightarrow ZZ \rightarrow llll$ channel	56
5.1	The $H \rightarrow ZZ \rightarrow llll$ channel	56
5.2	Signal samples	57
5.3	Background samples	58
5.3.1	ZZ background	59
5.3.2	$Z + jets$ background	61
5.3.3	$t\bar{t}$ background	61
5.4	Event selection	62
5.4.1	Preselection	63

5.4.2	Z candidate selection	63
5.4.3	ZZ candidate selection	63
5.5	Systematic uncertainties	64
5.6	Results	65
5.7	Expected exclusion limits	66
5.7.1	The treatment of systematic uncertainties	68
5.7.2	Presentation of the limits	69
5.8	Conclusions	71
5.9	Studies on the 2010 data	72
5.10	Electrons in the crack region	72
5.11	Results from 2010 dataset	75
6	Search for the SM Higgs boson in the $H \rightarrow ZZ \rightarrow ll\nu\nu$ channel	78
6.1	The $H \rightarrow ZZ \rightarrow ll\nu\nu$ channel	78
6.1.1	Expected sensitivity with 1fb^{-1}	80
6.2	Background samples	80
6.2.1	ZZ background	81
6.2.2	WZ and WW background	81
6.2.3	Z + jets background	82
6.2.4	$t\bar{t}$ and single top background	84
6.2.5	Inclusive W background	84
6.2.6	QCD background	85
6.3	Signal samples	85
6.4	The 2011 dataset	87
6.4.1	Pile-up in the data and MC samples	87
6.4.2	Triggers	89
6.5	Event selection	89
6.5.1	Preselection	89
6.5.2	$H \rightarrow ZZ \rightarrow ll\nu\nu$ selection	90
6.6	Background control regions and data driven estimates	94
6.6.1	ZZ background	94
6.6.2	Top and W control regions	94
6.6.3	WZ control regions	97

6.6.4	$Z + jets$ control regions	98
6.6.5	Data-driven estimate of multijet production	99
6.7	Systematic uncertainties	101
6.8	Results	106
6.9	Exclusion limits	108
6.10	Conclusion	112
7	Search for the invisible decay of the Higgs boson using the $ZH \rightarrow ll + inv$ channel	114
7.1	Discovery of a new boson	114
7.2	Introduction of the $ZH \rightarrow ll + inv$ decay channel	114
7.3	Models involving an invisibly decaying Higgs	115
7.4	Production mechanism and signature	115
7.5	The 2012 dataset	116
7.6	Event selection	116
7.7	Signal samples	119
7.8	Backgrounds	120
7.8.1	Standard Model ZZ background	120
7.8.2	Standard Model WZ and WW background	121
7.8.3	$Z+jets$ background	121
7.8.4	$t\bar{t}$ and single top background	121
7.8.5	Inclusive W jet background	123
7.8.6	SM Higgs simulation	124
7.8.7	QCD data driven estimation	125
7.9	Systematic uncertainties	125
7.10	Results	127
7.11	Limits	129
7.12	Conclusion	131
8	Summary	133
8.1	Current status of the new boson	134
8.2	Mass measurement	135
8.3	Spin and parity measurement	135

Chapter 1

Introduction

The Large Hadron Collider (LHC) started colliding protons together with a centre-of-mass energy of $\sqrt{s} = 7$ TeV in early 2010, and nominal data taking started later on in the year. The experiments at the LHC have since been at the forefront of particle physics, extending our knowledge of the Standard Model (SM), the current model used to describe the fundamental particles and their interactions. The ATLAS (A Toroidal LHC ApparatuS) detector, which is located at one of the four interaction points along the LHC ring, has surpassed its expected performance for each year of running, and has recorded over 25 fb^{-1} of data. The excellent performance of the detector, and of the other detectors at the LHC, has resulted in hundreds of published papers on a wide variety of particle physics phenomenon. These include SM validation, detailed studies of CP violation, Higgs boson searches, searches for super symmetry and exotic physics. In July 2012, two of the experiments at CERN; ATLAS and CMS, announced that they had discovered a new particle, thought to be the Higgs boson, which had been predicted over 45 years earlier. Since then the properties of this new particle have been studied.

The outline of this thesis is as follows. The first section introduces the Standard Model, and focuses on the theory behind the Higgs boson; how it has been searched for previously, and how it is produced at the LHC. This is followed by a description of the ATLAS detector and the methods used to identify and accurately reconstruct the particles and physics signatures produced in high energy collisions. There are then three analysis chapters. The first describes a pre-data taking study on the search for the SM Higgs boson in the $H \rightarrow ZZ \rightarrow llll$ channel and presents the expected exclusion limits with 1 fb^{-1} of data. Also presented in this section are first exclusion limits in the $H \rightarrow ZZ \rightarrow llll$, $H \rightarrow ZZ \rightarrow ll\nu\nu$ and $H \rightarrow ZZ \rightarrow llqq$ channels based on the $\sim 40 \text{ pb}^{-1}$ 2010 dataset. This is followed by a description of the search for the SM Higgs in the $H \rightarrow ZZ \rightarrow ll\nu\nu$ channel with the full 2011 dataset, which corresponds to 4.7 fb^{-1} of data. The work presented in this chapter contributed directly towards the Higgs discovery paper produced in July 2012. The final chapter describes the search for an invisibly decaying Higgs boson in the $ZH \rightarrow ll + inv$ channel. A signal in this search channel would represent a Beyond Standard Model (BSM) process. No such signal is observed and limits on the invisible decay of the Higgs candidate, as well as exclusion limits on other invisibly decaying Higgs-like particles, are set.

Chapter 2

Theory

In this chapter an overview of the Standard Model of particle physics is given, with an emphasis on the Higgs boson. Firstly the particles comprising the SM are introduced. This is followed by an overview of how mass terms can be identified in the Lagrangian. Some beyond the Standard Model theories are discussed briefly.

2.1 Introduction to the Standard Model

The Standard Model of particle physics is a theory in which the fundamental constituents of matter and the interactions between them are described. It is an incomplete theory as it only describes three of the four known fundamental forces observed in nature; electro-magnetism, the weak force and the strong force. It does not describe gravity, which as the weakest of all the forces is 10^{39} times weaker than the next weakest force [6]. As such its effects at the particle level in the presence of the other forces are as yet inaccessible.

The SM is a highly accurate theory that has been tested to extremely high precision [7]. Notably the prediction of the magnetic dipole moment of the electron agrees to within 10 parts in a billion with the measured value.

Within the SM the particles are split up into two categories; fermions, which have half integer spin, and bosons, which have integer or zero spin. The fermions are the constituents of matter and bosons are the particles that mediate the forces between them. Every fermion has a corresponding anti-particle with opposite charge.

2.1.1 Fermions

Fermions are split up into 2 categories; particles that interact via the strong force, called quarks, and particles that don't, called leptons. Both quarks and leptons are made up of 2 flavours, separated by a unit charge, and each flavour has 3 generations that differ only in mass.

The charged leptons are electrons, muons and taus. By convention the leptons are said to be negatively charged, and the corresponding anti-leptons positively charged. Leptons interact with both the electro-magnetic and weak forces. Each charged lepton and anti-lepton has a neutral partner, called an

electron, muon or tau neutrino or anti-neutrino. The neutrinos are not charged, and only interact via the weak force. The masses of the neutrinos are much smaller than the electron mass.

There are 6 quarks; 3 with charge $+2/3$ called the up, charm and top quark (u, c, t), and 3 with charge $-1/3$, called the down, strange and bottom quark (d, s, b). The signs of the charges are inverted for the anti-quarks. Because they are charged, all of the quarks can interact via the electro-magnetic force. Quarks are the only fermions that also interact via the strong force, because they have a conserved quantum number called colour. Colour charge is the strong force equivalent of the positive and negative charge of electro-magnetism. The main difference is that in the strong force there are three possible charges; red, blue or green. Each quark carries a charge corresponding to one of these colours. Individual quarks have not been observed, they are only ever seen in colourless states as either mesons (doublets) or as baryons (triplets).

2.1.2 Bosons

Each fundamental force has associated with it at least one boson. For electro-magnetism this boson is the photon. The photon is a massless boson with spin 1 and no charge.

There are 3 massive bosons that mediate the weak force, the neutral Z boson and the charged W^+ and W^- bosons. The W bosons only couple to left handed fermions, and as such the weak interaction is parity violating. All 3 electro-weak bosons have spin 1. The W bosons can couple to the photon because they are charged. There also exists self coupling between the electro-weak bosons, such that a three-point ZWW vertex and a four-point $WWWW$ vertex are possible.

There are 8 gluons that mediate the strong interaction. They carry colour charge and therefore are self interacting. They do not carry electro-magnetic charge and do not interact via the weak force.

2.1.3 Particle summary

	Fermions			Bosons
	I	II	III	
Quarks	u	c	t	γ
	d	s	b	g
Leptons	e	μ	τ	Z, W^+, W^-
	ν_e	ν_μ	ν_τ	H

Table 1: The particle content of the Standard Model.

A summary table of the fundamental particles is given in table 1. In total there are 61 distinguishable fundamental particles predicted by the theory; 6 leptons and the corresponding anti-leptons, 3 lots of 6 quarks and the corresponding anti-quarks, 8 gluons, 3 weak bosons, a photon and a Higgs boson. All of these particles have been experimentally verified to exist, with the exception of the Higgs boson. A candidate boson has been identified that has the expected properties of the Higgs boson, but further testing is required to completely confirm this to be the case. The Higgs boson is the particle left over from a process called spontaneous symmetry breaking, the mechanism through which the weak vector bosons obtain their mass.

2.2 Electro-weak theory

The following sub-section firstly highlights how mass terms can be obtained from the Lagrangians of the SM. The electro-magnetic and electro-weak theories are then introduced, and by imposing an invariance of the corresponding Lagrangians under a local gauge symmetry the electro-weak interactions between the fermions and bosons are determined. This then highlights the need for the Higgs mechanism.

2.2.1 Masses in the Standard Model

To obtain the equations of motion for a given system one starts by specifying a Lagrangian density, \mathcal{L} , then one applies the Euler-Lagrange equation. Take for example the Lagrangian density for a spinless boson

$$\mathcal{L} = \frac{1}{2}(\partial_\mu\phi\partial^\mu\phi) - \frac{1}{2}\left(\frac{mc}{\hbar}\right)^2\phi^2. \quad (1)$$

Here ϕ is the scalar field variable, and μ runs from 0 to 3. The Euler-Lagrange equation is

$$\partial_\mu\left(\frac{\partial\mathcal{L}}{\partial(\partial_\mu\phi)}\right) = \frac{\partial\mathcal{L}}{\partial\phi}, \quad (2)$$

which when applied to the Lagrangian given in equation 1 yields the familiar Klein-Gordon equation

$$\partial_\mu\partial^\mu\phi + \left(\frac{mc}{\hbar}\right)^2\phi = 0. \quad (3)$$

The second term on the left hand side is identified as the mass term, which originates from the ϕ^2 term in the interaction Lagrangian. It is true that all mass terms in the final equations of motion originate from the terms in the interaction Lagrangian that are quadratic in the field variable. In what follows the convention of setting $c = \hbar = 1$ is followed.

2.2.2 Particle interactions

The underlying theory behind the SM is Quantum Field Theory (QFT). In this theory there exist fields that permeate all space, and the bosons and fermions in the SM are the elementary quanta of excitations of their associated fields. By imposing local gauge invariance on the Lagrangians that describe the dynamics of the fermionic fields one can determine the nature of the interactions between the fermions. One dimensional local gauge transformation takes the form

$$\psi(x) \rightarrow \psi'(x) = e^{i\theta(x)}\psi(x), \quad (4)$$

where ψ , the fermionic field, and θ , the generator of the transformation, both depend on x , the space-time co-ordinate. The simplest form of local gauge invariance is one in which the generators of the transformation commute (the generators are Abelian). Physically this corresponds to a theory in which the mediating bosons have no self coupling. Such transformations belong to the U(1) gauge group, and are used to describe electro-magnetic interactions in the theory QED.

The remainder of this sub-section describes the procedure of applying a local gauge invariance to firstly electro-magnetic, and then electro-weak interactions. The latter will result in four massless bosons which are associated with the three boson of the weak interaction and the photon.

Starting from the Dirac Lagrangian, which describes the free fermionic fields

$$\mathcal{L}_D = i\bar{\psi}\gamma^\mu\partial_\mu\psi - m\psi\bar{\psi}, \quad (5)$$

and imposing an Abelian local gauge invariance requires one to introduce a vector field (A_μ) that couples to the fermion field (ψ_μ) and that also changes under local gauge transformations by

$$A_\mu \rightarrow A'_\mu = A_\mu + \frac{1}{q}\partial_\mu\theta(x), \quad (6)$$

where q can be the charge of any fermion. The changes to the overall Lagrangian from the local gauge transformations of the ψ and A_μ fields exactly cancel out, and one is left with a locally gauge invariant Lagrangian

$$\mathcal{L}'_D = i\bar{\psi}\gamma^\mu\partial_\mu\psi - m\psi\bar{\psi} + q(\bar{\psi}\gamma^\mu\psi)A_\mu. \quad (7)$$

To complete the Lagrangian one must add a term which describes this new vector field outside of the presence of the fermion field. This free field term takes the general form [6]

$$\mathcal{L}_{\text{FREE}} = \frac{-1}{4} F^{\mu\nu}F_{\mu\nu} + m_A^2 A^\nu A_\nu, \quad (8)$$

where $F^{\mu\nu} = \partial^\mu A^\nu - \partial^\nu A^\mu$ and the factor of $-1/4$ has been introduced to ensure the Euler-Lagrange equations coincide with Maxwell's equations [8]. The first term of equation 8 is invariant under the

Abelian local gauge transformation given in equation 6. The second term however, is not. From the discussion in section 2.2.1 the term on the right hand side of equation 8 can be identified as a mass term. To restore local gauge invariance one must impose the condition that the boson associated with the vector field described by equation 8 is massless, reducing equation 8 to the first term only. This constraint can be thought of as QFT imposing the condition that the force carrying particle of the interactions described by the $U(1)$ gauge group must be massless.

The total local gauge invariant Lagrangian describing a fermionic field coupled to a massless vector field is

$$\mathcal{L}_{\text{QED}} = \frac{-1}{4} F^{\mu\nu} F_{\mu\nu} + \bar{\psi}(i\not{D}_\mu - m)\psi \quad (9)$$

where $D_\mu = \partial_\mu + iqA^\mu$, which is simply a change of notation that incorporates the changes to the Lagrangian which result from the transformations in equations 6 without altering the form of the Dirac equation.

To describe the weak force, in which the mediating bosons have self-interactions, one must extend the local gauge transformations to the non-Abelian case. Such transformations are described by the more complicated $SU(2)_L$ group, where the subscript L denotes the fact that only left handed fermions interact with the weak force. Furthermore, the electro-magnetic theory can be incorporated into the weak theory by considering the group $SU(2)_L \oplus U(1)$. This will only modify the Lagrangian for the left handed components of the fermion fields, the Lagrangian for the right handed components of the fermion fields will still be given exactly by equation 9. The local gauge transformations take the form

$$\begin{aligned} \psi_L(x) &\rightarrow \psi'_L(x) = U\psi_L(x), \\ \bar{\psi}_L(x) &\rightarrow \bar{\psi}'_L(x) = \bar{\psi}_L(x)U^\dagger, \end{aligned} \quad (10)$$

where U is a unitary matrix, and ψ_L is now a spinor. Adopting this notation means that the transformations can be extended (or reduced) to any dimensionality, but for $SU(2)$ U is a 2×2 matrix. Any such unitary matrix can be expressed in the form $U = e^{iH}$, where H is a hermitian matrix. Furthermore H can be expressed in terms of four real parameters, θ , a_1 , a_2 and a_3 , in the form $H = \theta I + \vec{\tau} \cdot \vec{a}$, where $\vec{\tau}$ are the Pauli spin matrices, $\vec{\tau} \cdot \vec{a}$ is shorthand for $\tau_1 a_1 + \tau_2 a_2 + \tau_3 a_3$ and I is the identity. In this case the unitary matrix now takes the form $U = e^{i\theta(x)} e^{i\vec{\tau} \cdot \vec{a}(x)}$ where θ and \vec{a} depend on x . Making the $SU(2)_L \oplus U(1)$ group locally gauge invariant can now be reduced to considering transformations of the form

$$\psi_L(x) \rightarrow \psi'_L(x) = e^{i\vec{\tau} \cdot \vec{a}(x)} \psi_L(x) = S \psi_L(x) \quad (11)$$

since it has already been shown that transformations with generators of the form $e^{i\theta(x)}$ can be made locally gauge invariant.

Following the same procedure as for the U(1) gauge field, an interaction term between the fermion fields and the gauge field is added to the Dirac Lagrangian. In this case 3 such gauge fields are required, denoted by $\vec{W}_\mu = W_\mu^1, W_\mu^2, W_\mu^3$. The interaction term has the following form

$$\mathcal{L}_I = i\bar{\psi}_L (ig_W \vec{\tau} \cdot \vec{W}_\mu) \psi_L, \quad (12)$$

where the weak coupling parameter g_W has been introduced. The way in which the W_μ fields change under a local gauge transformation can be determined by applying the local gauge transformations given in equation 11 to the fermion fields, and requiring that the total Lagrangian is invariant. It can be shown that the transformation

$$\vec{\tau} \cdot \vec{W}_\mu(x) \rightarrow \vec{\tau} \cdot \vec{W}'_\mu(x) = S (\vec{\tau} \cdot \vec{W}_\mu(x)) S^{-1} + \frac{i}{g_W} [\partial_\mu(S)] S^{-1} \quad (13)$$

yields the correct terms in the Lagrangian to ensure local gauge invariance. Applying this to the case where $S = e^{-i\vec{\tau} \cdot \vec{a}(x)}$ gives the form of the local gauge transformation of the W_μ fields for electro-weak theory

$$W_\mu^j \rightarrow W_\mu^{j'} = W_\mu^j + \frac{1}{g_W} \partial_\mu a_j + \epsilon_{jkl} a^k W_\mu^l. \quad (14)$$

Returning to the Dirac Lagrangian, this time for only left handed fields, and adding in the interaction term gives

$$\mathcal{L}_D = i\bar{\psi}_L \gamma^\mu \partial_\mu \psi_L - m\psi_L \bar{\psi}_L - (g_W \bar{\psi}_L \gamma^\mu \vec{\tau} \psi_L) \cdot \vec{W}_\mu = i\bar{\psi}_L \not{D}_\mu \psi_L - m\psi_L \bar{\psi}_L \quad (15)$$

where

$$D_\mu = \partial_\mu + ig_W \vec{\tau} \cdot \vec{W}_\mu \quad (16)$$

which incorporates the transformation rule for the W_μ field. The free field terms for each of the gauge fields must be added in order to complete the Lagrangian. These have the form

$$\mathcal{L}_F = -\frac{1}{4} W^{i\mu\nu} W_{\mu\nu}^i - \frac{1}{4} B^{\mu\nu} B_{\mu\nu}, \quad (17)$$

where

$$W_{\mu\nu}^i = \partial_\mu W_\nu^i - \partial_\nu W_\mu^i - g_W \epsilon^{ijk} W_\mu^j W_\nu^k, \quad (18)$$

where i is an index running from 1 to 3, g_W is the SU(2) gauge coupling and $B_{\mu\nu}$ has the same form as $F_{\mu\nu}$ from equation 8. The W_ν^i are the SU(2) gauge fields and $B_{\mu\nu}$ is the U(1) gauge field. The last term of equation 18 is the self interaction term of the weak bosons, which has arisen due to the non-Abelian nature of the SU(2) group. The tensor ϵ^{ijk} appears in equation 18 because its components are

the structure constants of SU(2) [9]. The full Lagrangian for the electro-weak theory is then

$$\begin{aligned}\mathcal{L}_{\text{EW}} = & \bar{\psi}_{\text{R}}\gamma^{\mu}\left(\partial_{\mu} - ig_{\text{Y}}\frac{Y_{\text{R}}}{2}B_{\mu}\right)\psi_{\text{R}} \\ & + \bar{\psi}_{\text{L}}\gamma^{\mu}\left(\partial_{\mu} - ig_{\text{Y}}\frac{Y_{\text{L}}}{2}B_{\mu} - ig_{\text{W}}\frac{\tau^i}{2}W_{\mu}^i\right)\psi_{\text{L}} \\ & - \frac{1}{4}W_{\mu\nu}^iW^{i\mu\nu} - \frac{1}{4}B_{\mu\nu}B^{\mu\nu}\end{aligned}\quad (19)$$

where g_{Y} has been introduced as the electro-magnetic coupling and the terms Y_{R} and Y_{L} are the weak hypercharges of right and left handed fermions respectively.

The crucial aspect of equation 19 to note is that it is invariant under a local gauge transformation, provided that the fields given in equation 17 are massless. The mass eigenstates of the W_{μ} and B_{μ} fields will be the W and Z bosons and the photon. As there are no mass terms for these fields the weak bosons must acquire their mass through another mechanism, which does not break the local gauge invariance. This is the Higgs mechanism.

2.3 The Higgs mechanism

The above calculations started by considering a Lagrangian and imposing an invariance under a local gauge transformation. For the electro-weak Lagrangian this resulted in 4 massless bosons. It is now proposed that these bosons are only massless in an unstable equilibrium state, and that there is a true ground state in which 3 of the 4 bosons will acquire a mass-like term in the Lagrangian.

2.3.1 Spontaneous symmetry breaking

The phenomenon of spontaneous symmetry breaking is demonstrated in this sub-section by modifying the Klein-Gordon equation given in equation 3, such that

$$\mathcal{L}_{\text{H}} = \frac{1}{2}(\partial_{\mu}\phi)(\partial^{\mu}\phi) + \frac{1}{2}\mu^2\phi^2 - \frac{1}{4}\lambda^2\phi^4 \quad (20)$$

where ϕ is a scalar field and μ and λ are real positive constants. As it stands equation 20 has no physical mass term because the sign of the second term is positive, and yields an imaginary mass. It is invariant under the transformation $\phi \rightarrow -\phi$. The first term can be identified as the kinetic energy term, which will be zero if the field is constant. The second and third terms can be considered as a potential. Writing the Lagrangian in the form $\mathcal{L} = \mathcal{T} - \mathcal{U}$, where \mathcal{T} is the kinetic energy density and \mathcal{U} is the potential energy density, the potential is:

$$\mathcal{U}(\phi) = -\frac{1}{2}\mu^2\phi^2 + \frac{1}{4}\lambda^2\phi^4, \quad (21)$$

which must be minimised in order to find the ground state. There are three extrema; the trivial $\phi = 0$, which is an unstable equilibrium; and $\phi = \pm\mu/\lambda$ which are the ground states. One can rewrite the potential in terms of a new variable η , which is 0 at either of the two stable equilibria. The new variable η is related to ϕ via

$$\eta \equiv \phi \pm \frac{\mu}{\lambda}. \quad (22)$$

The Lagrangian takes the form

$$\mathcal{L}_H = \frac{1}{2}(\partial_\mu\eta)(\partial^\mu\eta) + \mu^2\eta^2 \pm \mu\lambda\eta^3 + \frac{\lambda^2\eta^4}{4} - \frac{\mu^4}{4\lambda^2}. \quad (23)$$

The second term now can be identified as a mass term with the correct sign, the third and fourth terms are self coupling terms and the final term is a constant and therefore is irrelevant for a potential.

This is the process of spontaneous symmetry breaking. The Lagrangian given in equation 20 is invariant under the transformation $\phi \rightarrow -\phi$, but equation 23, which describes exactly the same physics, is not invariant under $\eta \rightarrow -\eta$, thus the symmetry is said to be broken. It happened because one of the two ground states had to be chosen, and the Lagrangian is not symmetric about the ground states, only about the unstable equilibrium. In this sense it is called a spontaneously broken symmetry, because the choice of ground states is arbitrary.

2.3.2 Spontaneous breaking of a global U(1) symmetry

To apply the spontaneous symmetry breaking mechanism to the U(1) group the Lagrangian must be formulated such that the initial symmetry has the form of the local gauge invariance used in equation 10, rewritten here for the ϕ field

$$\phi \rightarrow \phi' = U(x)\phi. \quad (24)$$

To do so one must first extend the symmetry to a continuous symmetry. Consider a complex scalar field, $\phi = \frac{1}{\sqrt{2}}(\phi_1 + i\phi_2)$, the Lagrangian for which is

$$\mathcal{L}_H = \frac{1}{2}(\partial_\mu\phi)^*(\partial^\mu\phi) + \frac{1}{2}\mu^2(\phi^*\phi) - \frac{1}{4}\lambda^2(\phi^*\phi)^2. \quad (25)$$

This is the equivalent of equation 20, except that it involves a complex field. It is invariant under a global gauge transformation of the form given in equation 24 except that U is not a function of x . The potential which has to be minimised in order to find the ground state is

$$\mathcal{U}(\phi) = -\frac{1}{2}\mu^2(\phi_1^2 + \phi_2^2) + \frac{1}{4}\lambda^2(\phi_1^2 + \phi_2^2)^2 \quad (26)$$

and is shown in fig. 1.

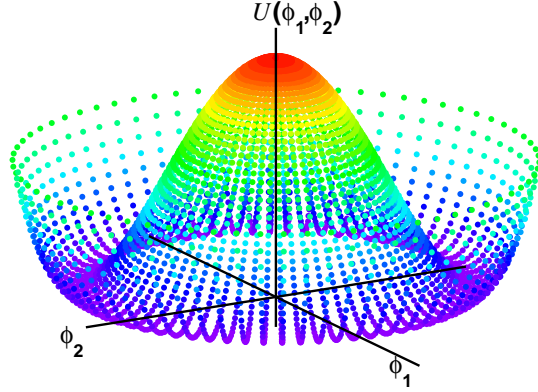


Figure 1: The form of the potential given in equation 26, which has a symmetry about the unstable equilibrium which is broken once a ground state is chosen.

There are a continuum of degenerate ground states which lie on a circle at $\phi_{1_{min}}^2 + \phi_{2_{min}}^2 = \mu^2/\lambda^2$. Any of the minima can be chosen in order to break the symmetry, the simplest is $\phi_{1_{min}} = \mu/\lambda$ and $\phi_{2_{min}} = 0$. The final step to take is to rewrite the Lagrangian in terms of the new minimum, using the coordinates $\eta \equiv \phi_1 - \mu/\lambda$ and $\zeta \equiv \phi_2$. The Lagrangian then becomes

$$\mathcal{L}_H = \left[\frac{1}{2}(\partial_\mu \eta)(\partial^\mu \eta) - \mu^2 \eta^2 \right] + \left[\frac{1}{2}(\partial_\mu \zeta)(\partial^\mu \zeta) \right] - \left[\mu\lambda(\eta^3 + \eta\zeta^2) + \frac{\lambda^2}{4}(\eta^4 + \zeta^4 + 2\eta^2\zeta^2) \right] + \frac{\mu^4}{4\lambda^2}. \quad (27)$$

The first term is the free Klein-Gordon equation for a scalar boson of mass $m_\eta^2 = \mu$. The second term is the same except this time the scalar boson has no mass, $m_\zeta^2 = 0$. This is a Goldstone boson, and one such boson always appears when spontaneously breaking a continuous global symmetry [9]. The third term describes five different couplings between these bosons, and the constant term can be ignored.

2.3.3 Spontaneous breaking of a local U(1) symmetry

The next step is to make this global symmetry a local one. The Lagrangian given in equation 25 can be made invariant under the local U(1) gauge transformation given in equation 24 by following the prescription outlined in sub-section 2.2.2, whereby a massless gauge field A_μ was introduced and the derivatives were replaced with covariant derivatives of the form $D_\mu = \partial_\mu + igA_\mu$. The locally gauge invariant Lagrangian is

$$\mathcal{L}_H = \frac{1}{2} \left[(\partial_\mu - igA_\mu)\phi^* \right] \left[(\partial^\mu + igA_\mu)\phi \right] + \frac{1}{2}\mu^2(\phi^*\phi) - \frac{1}{4}\lambda^2(\phi^*\phi)^2 - \frac{1}{4}F^{\mu\nu}F_{\mu\nu}. \quad (28)$$

The local symmetry of this Lagrangian can be broken in the same way as the global symmetry, by formulating the Lagrangian around the stable equilibrium. Using the coordinates $\eta \equiv \phi_1 - \mu/\lambda$ and $\zeta \equiv \phi_2$ the Lagrangian becomes

$$\begin{aligned}
 \mathcal{L}_H = & \left[\frac{1}{2}(\partial_\mu \eta)(\partial^\mu \eta) - \mu^2 \eta^2 \right] + \left[\frac{1}{2}(\partial_\mu \zeta)(\partial^\mu \zeta) \right] \\
 & + \left[-\frac{1}{4}F^{\mu\nu}F_{\mu\nu} + \frac{g}{2}\left(\frac{\mu}{\lambda}\right)^2 A_\mu A^\mu \right] \\
 & + \left[g\{\eta(\partial_\mu \zeta) - \zeta(\partial_\mu \eta)\}A^\mu + \frac{\mu}{\lambda}g^2\eta(A_\mu A^\mu) + \frac{1}{2}g^2(\zeta^2 + \eta^2)(A_\mu A^\mu) \right. \\
 & \left. - \lambda\mu(\eta^3 + \eta\zeta^2) - \frac{1}{4}\lambda^2(\eta^4 + 2\eta^2\zeta^2 + \zeta^4) \right] \\
 & + \frac{\mu}{\lambda}(\partial_\mu \zeta)A^\mu + \left(\frac{\mu}{2\lambda}\right)^2. \tag{29}
 \end{aligned}$$

The first two terms are again the Klein-Gordon equations for a massive and massless boson respectively. The second term is the free field term for the gauge field, which has now acquired a mass

$$m_A = 2\sqrt{\pi}\left(\frac{g}{\lambda}\right). \tag{30}$$

The third term represents the interaction terms of the η , ζ and A_μ fields. The final term has a constant, which is irrelevant for a Lagrangian, but also contains an unwanted interaction term between the Goldstone boson and the gauge field. This unwanted term can be removed without loss of generality by selecting a particular gauge. Rewriting the local gauge invariance in terms of the real and imaginary components

$$\phi \rightarrow \phi' = (\cos\theta + i\sin\theta)(\phi_1 + i\phi_2) = (\phi_1\cos\theta - \phi_2\sin\theta) + i(\phi_1\sin\theta + \phi_2\cos\theta) = \phi'_1 + i\phi'_2, \tag{31}$$

and selecting $\theta = \tan^{-1}(\phi_2/\phi_1)$ gives $\phi'_2 = 0$. Applying the transformation of equation 31 leaves the Lagrangian of equation 29 unchanged (due to the local gauge invariance). Using the fact that $\zeta = \phi_2 = 0$ in this particular gauge the Lagrangian becomes

$$\begin{aligned}
 \mathcal{L}_H = & \left[\frac{1}{2}(\partial_\mu \eta)(\partial^\mu \eta) - \mu^2 \eta^2 \right] + \left[-\frac{1}{4}F^{\mu\nu}F_{\mu\nu} + \frac{g}{2}\left(\frac{\mu}{\lambda}\right)^2 A_\mu A^\mu \right] \\
 & + \left[\frac{\mu}{\lambda}g^2\eta(A_\mu A^\mu) + \frac{1}{2}g^2\eta^2(A_\mu A^\mu) - \lambda\mu(\eta^3) - \frac{1}{4}\lambda^2\eta^4 \right] + \left(\frac{\mu}{2\lambda}\right)^2 \tag{32}
 \end{aligned}$$

The first term describes a free massive scalar boson η , the second term describes a free massive gauge field A_μ and the third term describes the interactions between them.

A mass has been given to the gauge bosons, and the consequence of this is a new massive scalar boson, which is identified as the SM Higgs boson. In this gauge the Goldstone bosons of equation 29 have not disappeared entirely, they are absorbed as an extra degree of freedom of the A_μ fields which is how they acquired mass.

2.3.4 Spontaneous breaking of SU(2) symmetry

¹ To alter the local U(1) symmetry breaking mechanism outlined in the previous 2 sub-sections to the breaking of a local SU(2) symmetry the complex scalar boson field ϕ is extended to an SU(2) doublet of the form

$$\phi = \begin{pmatrix} \phi_\alpha \\ \phi_\beta \end{pmatrix} = \sqrt{\frac{1}{2}} \begin{pmatrix} \phi_1 + i\phi_2 \\ \phi_3 + i\phi_4 \end{pmatrix} \quad (33)$$

so that the Lagrangian becomes

$$\mathcal{L}_H = \frac{1}{2}(\partial_\mu \phi)^\dagger (\partial^\mu \phi) + \frac{1}{2}\mu^2(\phi^\dagger \phi) - \frac{1}{4}\lambda^2(\phi^\dagger \phi)^2, \quad (34)$$

which is still invariant under global SU(2) transformations. To extend this global gauge invariance to a local one the derivatives in equation 34 are replaced by the covariant derivatives of equation 16 which introduces the three W_μ fields. The W_μ fields transform as shown in equation 14 and the free terms of equation 17 corresponding to the SU(2) gauge fields are added. The Lagrangian now becomes

$$\mathcal{L}_H = \frac{1}{2}[(\partial_\mu + ig_W \vec{\tau} \cdot \vec{W}_\mu)\phi]^\dagger [(\partial^\mu + ig_W \vec{\tau} \cdot \vec{W}_\mu)\phi] + \frac{1}{2}\mu^2(\phi^\dagger \phi) - \frac{1}{4}\lambda^2(\phi^\dagger \phi)^2 - \frac{1}{4}W_{\mu\nu}W^{\mu\nu}, \quad (35)$$

which is locally gauge invariant under SU(2) transformations. The potential is minimised when $\phi^\dagger \phi = -\mu^2/\lambda^2$, which is the equivalent of the circle of minima in fig. 1, except that ϕ now has four dimensions. A particular gauge is now chosen in which $\phi_1 = \phi_2 = \phi_4 = 0$ and $\phi_3^2 = -\mu^2/\lambda^2 \equiv v^2$. With this particular gauge equation 33, which gives the general form of ϕ in terms of the four fields $\phi_{1,2,3,4}$, becomes

$$\phi_0 \equiv \sqrt{\frac{1}{2}} \begin{pmatrix} 0 \\ v \end{pmatrix} = \sqrt{\frac{1}{2}} \begin{pmatrix} 0 \\ v + h(x) \end{pmatrix} \quad (36)$$

where the local gauge invariance has been used in the last step. Substituting equation 36 into the Lagrangian of equation 34 yields a Lagrangian describing 3 massive bosons of mass $M_W = g_W v$, a massive scalar, the Higgs boson and the interaction terms between them. The particular gauge chosen ensures that the Goldstone bosons are not present, but that the degrees of freedom associated with them are absorbed by the mass terms of the gauge fields.

¹This section follows the derivation from [10].

The final electro-weak Lagrangian including the Higgs terms is

$$\begin{aligned}
 \mathcal{L} = & -\frac{1}{4}(W_{\mu\nu} \cdot W^{\mu\nu} + B_{\mu\nu} B^{\mu\nu}) \\
 & + \left[\bar{\psi}_L \gamma^\mu (\partial_\mu + i\frac{g_W}{2} \vec{\tau} \cdot \vec{W}_\mu + ig_Y \frac{Y_L}{2} B_\mu) \psi_L \right] + \left[\bar{\psi}_R \gamma^\mu (\partial_\mu + ig_Y \frac{Y_R}{2} B_\mu) \psi_R \right] \\
 & + \left[(\partial_\mu + i\frac{g_W}{2} \vec{\tau} \cdot \vec{W}_\mu + ig_Y \frac{Y}{2} B_\mu) \phi \right]^\dagger \left[(\partial^\mu + i\frac{g_W}{2} \vec{\tau} \cdot \vec{W}_\mu + ig_Y \frac{Y}{2} B_\mu) \phi \right] + \frac{1}{2} \mu^2 (\phi^\dagger \phi) - \frac{1}{4} \lambda^2 (\phi^\dagger \phi)^2 \\
 & + \text{fermion and Higgs coupling terms.}
 \end{aligned} \tag{37}$$

2.3.5 Masses of the electro-weak bosons

The masses of the electro-weak bosons can be determined by combining the above results and considering a transformation invariant under $SU(2)_L \oplus U(1)$. This will yield 3 massive vector bosons, 2 of which are charged and 1 that is neutral, and a massless boson with no charge. These bosons can then be associated to the W^+ , W^- , Z and γ .

The relevant term to consider in the Lagrangian of equation 37 is

$$\mathcal{L}_M = \left[(i\frac{g_W}{2} \vec{\tau} \cdot \vec{W}_\mu + ig_Y \frac{Y}{2} B_\mu) \phi \right]^\dagger \left[(i\frac{g_W}{2} \vec{\tau} \cdot \vec{W}_\mu + ig_Y \frac{Y}{2} B_\mu) \phi \right]. \tag{38}$$

Substituting in equation 36 yields

$$\mathcal{L}_M = \frac{1}{8} \begin{pmatrix} g_W W_\mu^3 + g_Y B_\mu & g_W(W_\mu^1 - W_\mu^2) \\ g_W(W_\mu^1 + W_\mu^2) & -g_W W_\mu^3 + g_Y B_\mu \end{pmatrix} \begin{pmatrix} 0 \\ \nu \end{pmatrix} \times \text{H.C} \tag{39}$$

where H.C stands for the hermitian conjugate. Defining $W^\pm = \frac{1}{\sqrt{2}}(W^1 \pm iW^2)$ gives

$$\mathcal{L}_M = \left(\frac{1}{2} \nu g_W \right)^2 W_\mu^+ W^{\mu-} + \frac{1}{8} \nu^2 (g_Y B_\mu - g_W W_\mu^3)(g_Y B^\mu - g_W W^{\mu 3}). \tag{40}$$

The first term can be identified as a mass term with mass $M_W = \frac{1}{2} g_W \nu$. The remaining term can be written out in matrix form

$$\frac{1}{8} \nu^2 (W_\mu^3 \ B_\mu) \begin{pmatrix} g_W^2 & -g_Y g_W \\ -g_Y g_W & g_Y^2 \end{pmatrix} \begin{pmatrix} W^{3\mu} \\ B^\mu \end{pmatrix}. \tag{41}$$

The physical fields Z_μ and A_μ corresponding to the Z boson and the photon respectively must diagonalise the 2×2 matrix in equation 41. The masses of the fields can then be obtained by identifying the resulting diagonalised matrix equation with $\frac{1}{2}(M_Z^2 Z_\mu^2 + M_A^2 A_\mu^2)$, which is the appropriate mass term for 2 neutral vector bosons. The diagonalised fields are given by [10]

$$\begin{aligned}
 A_\mu &= \frac{g_Y W_\mu^3 + g_W B_\mu}{\sqrt{g_W^2 + g_Y^2}} \\
 Z_\mu &= \frac{g_W W_\mu^3 - g_Y B_\mu}{\sqrt{g_W^2 + g_Y^2}},
 \end{aligned} \tag{42}$$

which yields $M_Z = \frac{1}{2}v\sqrt{(g_W^2 + g_Y^2)}$ and $M_A = 0$. It is conventional to introduce the Glashow-Weinberg angle, defined by $\tan\theta_W \equiv g_Y/g_W$, such that the masses of the W and Z fields are related by

$$M_W = M_Z \cos(\theta_W). \quad (43)$$

2.4 Searches for the Higgs boson

The Standard Model Higgs boson was predicted in 1964 [11], following earlier work on electro-weak symmetry breaking [12, 13]. There were few theoretical constraints on the mass of the boson at that time. Early searches focused on nuclear transitions [14] and neutron-nucleus scattering [15] which excluded the mass ranges $1.03 < m_H < 18.3$ MeV and $m_H < 15$ MeV respectively [16].

The search for a high mass Higgs boson at particle colliders began at LEP, an electron-positron collider. The centre-of-mass energy of the LEP collider started at 90 GeV, and was subsequently increased to 160 GeV in order to study W pair production. Direct searches for the Higgs boson were performed by considering the $Z \rightarrow H + ff$ and $ee \rightarrow Z + H$ production mechanisms. An indication of the possible Higgs mass range was also obtained by probing rare electro-weak processes to high precision. Loop corrections involving the Higgs boson affect the rate of these processes, and exclusion limits were obtained by fitting all possible Higgs boson masses to the data.

It was not until the discovery of the top quark [17] in 1995 that the strongest predictions for the mass of the SM Higgs boson could be obtained from these fits, which indicated that the mass of the Higgs boson was just higher than the W mass of 81 GeV. As a result the centre-of-mass energy at LEP was gradually increased. By the year 2000 LEP was colliding electrons together at a centre-of-mass energy of 209 GeV and still no significant excess was observed. LEP operation ended in 2000, to allow work on the LHC to proceed. The final exclusion limits from LEP placed a lower bound on the mass of the SM Higgs boson at $m_H > 114.4$ GeV.

Additional exclusion limits were placed on the mass of the Higgs boson using data from the CDF and D0 experiments located at the Tevatron. The dominant production mechanism for the Higgs boson at the Tevatron was gluon-gluon fusion, for which the Feynman diagram is shown in fig. 3(a). Using Tevatron data a further experimental constraint on the mass of the Higgs boson was placed at $156 < m_H < 177$ GeV [18]. The Tevatron data together with that from LEP is used in fig. 2, which summarizes the state of the searches for the Higgs boson before the LHC. This figure shows the χ^2 distribution obtained from the electro-weak fits as a function of m_H . The blue band is an estimate of the error due to missing higher order terms. The yellow regions represent the excluded regions from both LEP and the Tevatron.

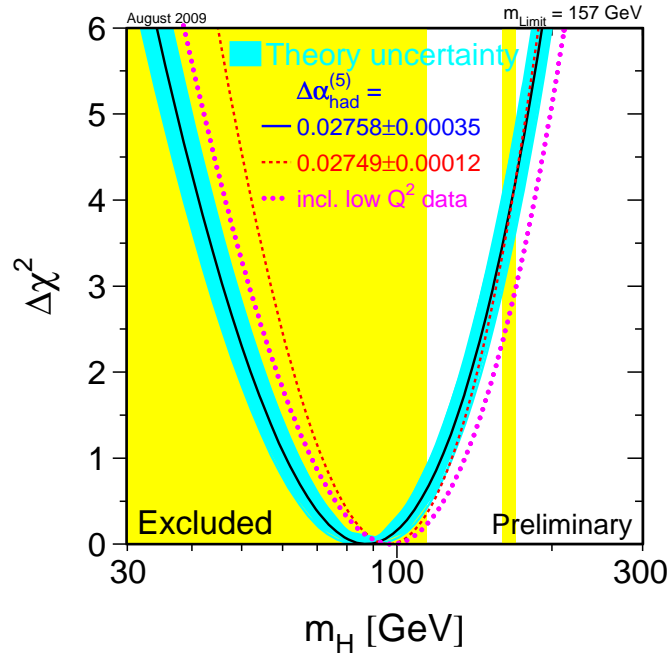


Figure 2: A summary of the pre-LHC exclusion limits of the SM Higgs boson using electro-weak fits [7]. The yellow band indicates an excluded region.

2.4.1 SM Higgs production at the LHC

There are many different Higgs boson production mechanisms at the LHC. The four most probable processes are shown in fig. 3, and the cross sections at $\sqrt{s} = 7$ TeV for these processes as a function of Higgs mass are shown in fig. 4.

At LHC energies the most probable production mechanism is the gluon-gluon fusion (ggF) process shown in fig. 3(a), where it is most likely that the quark in the triangular loop will be a top quark. This is the dominant production process for the high mass Higgs searches presented in chapters 5 and 6 respectively, where it accounts for approximately 90% of the expected signal. The next most abundant production mechanism is the Vector Boson Fusion (VBF) process shown in fig. 3(b) in which a Higgs boson is produced along with two jets. This process accounts for the remaining 10% of the expected signal of high mass Higgs production. The associative vector boson production mechanism shown in fig. 3(c), whereby the Higgs boson can be produced in association with a Z or W boson, is a much rarer process than ggF and VBF processes, and is particularly useful for decay channels such as the $H \rightarrow b\bar{b}$ channel, that have a large amount of QCD background. In this case one can use the leptonic decays of

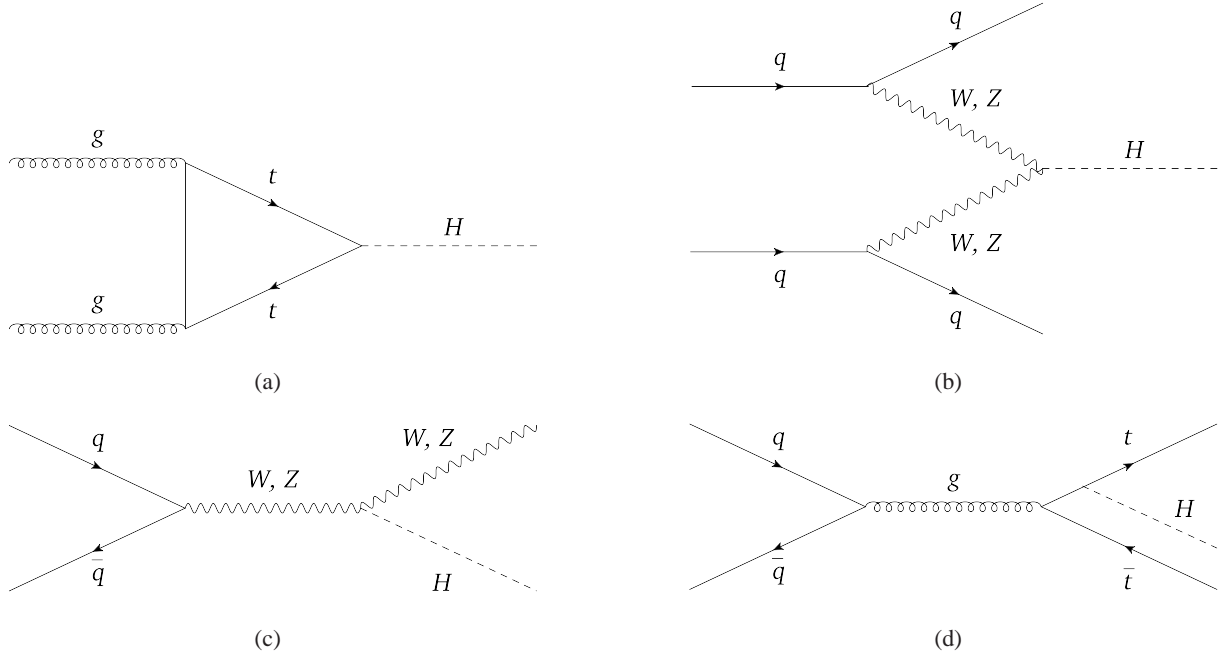


Figure 3: Feynman diagrams of the most likely Higgs production processes at the LHC (a) gluon gluon fusion, (b) vector boson fusion, (c) associated vector boson production and (d) associated $t\bar{t}$ production.

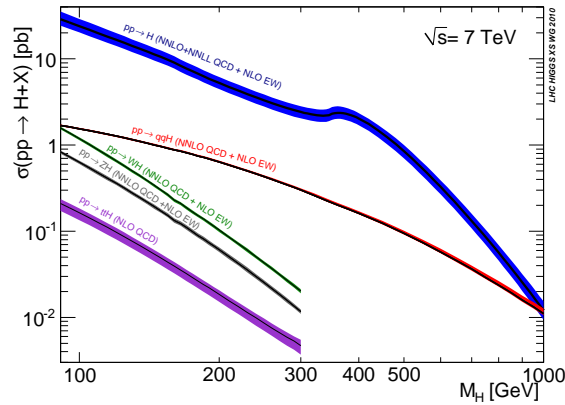


Figure 4: Cross sections at $\sqrt{s} = 7 \text{ TeV}$ of the most likely Higgs production mechanisms at the LHC as a function of Higgs mass [19].

the W or Z boson to help distinguish the signal events. This production mechanism is also used in the $ZH \rightarrow ll + inv$ search presented in chapter 7, where the Z boson is required to decay to 2 leptons. The associated $t\bar{t}$ production mechanism, shown in 3(d), is a very rare process, and will be used to extract the $Ht\bar{t}$ coupling when the LHC has collected more data. It is not considered in the searches presented in this thesis.

2.5 Beyond the Standard Model

Despite the success of the Standard Model there is still reason to believe that there is new physics to be discovered. Perhaps the most compelling evidence comes from cosmological studies, where a large excess in non-luminous matter has been indirectly observed by numerous experiments [20, 21], and is given the name Dark Matter (DM). None of the Standard Model particles are a good candidate for dark matter. A neutral stable particle is required, and the upper bounds on the mass of the neutrinos is found to be too small. Therefore a new particle is required. There are additional problems with the Standard Model which motivate dark matter and are described below.

2.5.1 The hierarchy problem

The mass of the candidate Higgs boson is around 125 GeV. Splitting up the mass of the Higgs boson into the quantum corrections gives $M_H^2 = M_{H0}^2 + \Delta M_H^2$ for the physical mass of the Higgs boson, where

$$\Delta M_H^2 = \frac{\lambda^2}{16\pi^2} \int \frac{d^4 p}{p^2} \sim \frac{\lambda^2}{16\pi^2} \Lambda^2. \quad (44)$$

The integral is performed over the momenta of the particles in the loop correction to the bare Higgs mass, and is valid up until Λ , which is the cut off at which the SM is no longer valid [21]. λ is simply a coupling constant with unit order of magnitude, therefore the quantum correction of the mass of the Higgs boson is of the same order as the scale of new physics. Currently the only known cut off for the validity of the SM is the Planck mass (M_p), the scale at which quantum effects to gravitational forces become important. This has a value of $M_p = \sqrt{\hbar c/GN} \sim 1.2 \times 10^{19}$ GeV. If this were indeed the only scale at which the SM was not valid then the bare mass of the Higgs and the quantum corrections would both be of order 10^{19} GeV, but these would have to cancel out to give the observed Higgs mass, which is 10^{17} orders of magnitude smaller. This cancellation is called a fine tuning problem. The fact that the mass of the Higgs is of order 100 GeV is reason to believe that there is a cut off scale around 1 TeV at which the SM is no longer valid. Such a cut off would provide a natural solution to the Hierarchy problem.

2.5.2 Neutrino masses

In the SM there are no right handed neutrino fields, and so the weak bosons only couple to left handed neutrinos and are predicted to be massless. However, the observations that neutrinos oscillate between flavours [22] indicates that they have mass. This is direct evidence that the SM is incomplete, and is further reason to believe that there is BSM physics. The measurement of the mass hierarchy of neutrinos,

which determines the difference in masses of the different flavours, is currently being studied by many neutrino experiments [23]. The absolute mass of neutrinos is unknown, as is the mechanism through which they acquire their mass. A measurement of the absolute mass is beyond the scope of current experiments [24].

2.6 Dark matter and the Higgs boson

In order for the DM candidate to solve the hierarchy problem it must couple to the Higgs boson. To account for the non-luminous matter in the universe and have the correct relic density it must also be weakly interacting and therefore stable. The detailed measurements of the Z lineshape at LEP investigated the invisible decay width of the Z boson, and found that it was consistent with 3 generations of neutrinos [25]. As such a DM candidate with mass less than $m_Z/2$ that couples to the Z boson is excluded. Additional limits on the annihilation cross-section of dark matter candidates were also performed at LEP [26]. To allow for a DM candidate that is consistent with the current measurements of the cross-sections of SM processes it is proposed that the new particle may only be produced in pairs [21], such that, for example, the decay $H \rightarrow \chi + \chi$ would be possible, where χ represents a DM candidate, but interactions of the form $SM + SM \rightarrow \chi \rightarrow SM + SM$ would not be allowed. Additionally this constraint naturally requires the DM candidate to be stable.

The search for invisible decays of the Higgs boson presented in chapter 7 is motivated by searching for DM candidates.

2.7 Supersymmetry

The hierarchy problem is also solved by supersymmetry (SUSY). This theory introduces a new particle for every particle in the SM, which has the same properties as the SM particle except that the spin differs by 1/2. SUSY models require at least 2 Higgs bosons, and most models require 5, which correspond to a light Higgs, a heavy Higgs, a positively and a negatively charged Higgs and a CP odd Higgs. If the candidate Higgs boson at 125 GeV is found to have the SM couplings then the search for the heavier Higgs will be a stringent test of SUSY. SUSY extensions to the SM provide a natural framework for DM to be incorporated into the SM, as some of the additional particles are natural DM candidates. The search for SUSY is one of the goals of the LHC. Currently no direct evidence for SUSY has been found. Some of the simpler models have been constrained using the data from the ATLAS, CMS and LHCb experiments. Nevertheless there is still unexplored phase space, and many SUSY models will require more data to be ruled out.

Chapter 3

The ATLAS Detector

In this chapter the large hadron collider is introduced, and a brief summary of the four main detectors is given. The main aims of the ATLAS experiment are outlined, the co-ordinate system adopted by ATLAS is explained and finally this is followed by a detailed account of the components that make up the ATLAS detector.

3.1 The Large Hadron Collider

The LHC is a hadron-hadron synchrotron collider located at the Franco-Swiss border near Geneva, which was built at the European Organisation for Nuclear Research known as CERN. It was designed to collide high energy hadronic beams together at large instantaneous luminosities in order to produce rare particle physics processes at a rate sufficiently high to study them. It consists of a large accelerator located in a tunnel 26.7 km in circumference, which lies between 45 – 170 m underground, into which two counter rotating hadronic beams are injected. For the majority of time the LHC is used as a proton-proton collider, but it is also occasionally used to collide heavy ions, such as lead ions [27]. The remainder of this section focuses on the proton-proton collisions.

Protons are first supplied from a linear accelerator (Linac 2) in which they are accelerated up to an energy of 50 MeV. They are accelerated further at three increasingly large synchrotron accelerators - proton synchrotron booster (1.4 GeV), proton synchrotron (25 GeV) and super proton synchrotron (450 GeV) - until finally they are injected into the LHC.

Integrated luminosity, denoted by L , is a measure of the total number of collisions expected and has units of cm^{-2} , although it is usually measured in multiples of the 'barn', b , where $1b = 10^{-24}\text{cm}^{-2}$. Instantaneous luminosity, denoted by \mathcal{L} , is simply the luminosity per second. The total number of collisions is calculated from the cross section (σ) which varies for different processes, and is related to the luminosity through equation 45.

$$N = \sigma \int \mathcal{L} dt = \sigma L \quad (45)$$

The LHC is designed to supply an instantaneous luminosity of $10^{34} \text{ cm}^{-2}\text{s}^{-1}$ which corresponds to approximately one billion proton proton collisions per second.

In September 2010 the beams were accelerated to yield a centre-of-mass energy of $\sqrt{s} = 7 \text{ TeV}$ and nominal data taking started. The beams remained at this energy throughout 2011 and the LHC delivered a

total integrated luminosity of $\sim 5 \text{ fb}^{-1}$ to the two general purpose detectors; ATLAS and CMS (Compact Muon Solenoid). In total four detectors are located around the ring as shown in fig. 5; ATLAS, CMS and two smaller, specialised detectors; ALICE (A Large Ion Collider) and LHCb (Large Hadron Collider Beauty). Having two general purpose detectors that utilise different technologies ensures that any new physics discoveries observed by a single experiment can be cross checked by an independent experiment. It also doubles (approximately) the integrated luminosity and thus increases the frequency of rare events.

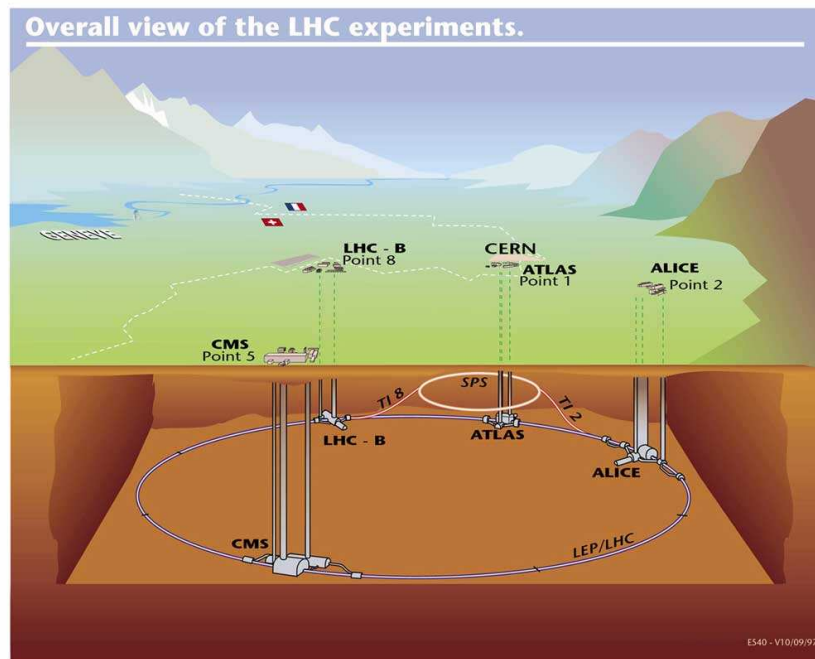


Figure 5: The location of the four main detectors located around the LHC ring [28].

3.2 The aims of the ATLAS experiment

In order to ensure the sensitivity to a variety of final state signatures the basic design requirements are the following, as outlined in the letter of intent [29] in 1992:

- High quality electro-magnetic calorimetry for electron and photon identification and measurements, complemented by hermetic jet and transverse missing energy calorimetry.
- Efficient tracking at high luminosity for lepton momentum measurements and to enhance electron and photon identification, and tau and heavy flavour tagging capabilities at lower luminosity.

- Precision muon momentum measurements with stand-alone capabilities at the highest luminosities.
- Large acceptance in the polar angle and complete azimuthal angle coverage.
- Triggering and measurements of particles at low momentum thresholds.

3.3 Co-ordinate system and units

A right handed co-ordinate system is used for the ATLAS detector, the origin of which is at the centre of the detector. The positive x axis points towards the centre of the ring, the positive y axis points vertically upwards and the positive z axis points along the beam pipe. The azimuthal angle (ϕ) and the polar angle (θ) are defined with respect to these axes. An alternative measure of the polar angle is the pseudo-rapidity (η) which is defined as

$$\eta = -\ln \tan(\theta/2). \quad (46)$$

The angular separation (ΔR) between two objects is defined to be

$$\Delta R = \sqrt{(\Delta\phi)^2 + (\Delta\eta)^2}. \quad (47)$$

Because of the high boost along the z axis particles often have their energy and momentum given in terms of the transverse ($x - y$ plane) components only, where these are defined as ($E_T = E \sin \theta$) and ($p_T = p \sin \theta$). When the mass of the particle is small compared to its momentum the mass component of the energy can be neglected and these two values are approximately equal.

3.4 Detector overview

The ATLAS detector is a general purpose detector, designed to explore potential new particle phenomena at the TeV energy scale. It is a 4π detector, with complete azimuthal angle coverage, and a large acceptance in pseudorapidity. It is forward-backward symmetric with respect to the interaction point. It consists of an inner detector [30], primarily used for tracking and particle recognition; calorimeters [31] [32], for measuring the energies of both electro-magnetic and hadronic particles, and to aid in particle identification; and muon chambers [33], for precise momentum and position measurements of muons. The performance goals and η range of these sub-detectors are given in table 2. There are four superconducting magnets; a thin, 2 T solenoid magnet surrounding the inner detector, and three large superconducting magnets one in each end cap and one surrounding the calorimeters supplying 1 T and

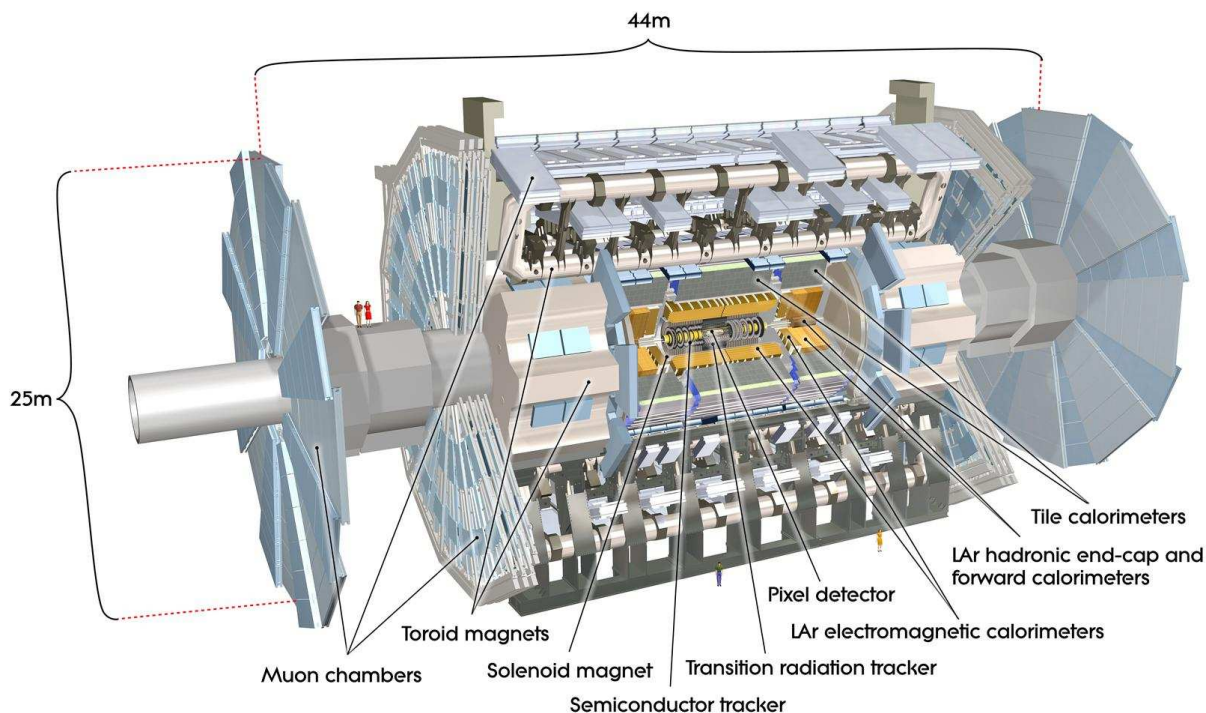


Figure 6: The cut away view of the ATLAS detector. Shown are the four super conducting magnets, the muon chambers, the hadronic and electro-magnetic calorimeters and the inner detector, which consists of the pixel detector, the transition radiation tracker and the semiconductor tracker [28].

0.5 T magnetic fields respectively. The layout and sub-systems of the ATLAS detector can be seen in fig. 6.

The ATLAS detector also has complex trigger systems and luminosity detectors. The trigger system uses measurements made in all of the sub-systems in the detector, and is split up into three different levels, L1, L2, and the event filter. A combination of these triggers is required to reduce the raw data rate (40 MHz [34]) down to approximately 200 Hz so that it can be written to disk. The η ranges for the trigger systems of the various sub detectors are given in table 2. The majority of collisions in the ATLAS detector are ‘soft collisions’ - collisions in which relatively little momentum is exchanged. Such events can be used to measure the luminosity. Dedicated detectors to record these events are located in the forward regions of the experiment.

Table 2: Performance goals of the ATLAS detector. The units for energy and momentum are in GeV [35].

Detector component	Required resolution	η range	
		measurement	Trigger
Tracking	$\sigma_{p_T}/p_T = 0.05\%$, $p_T \oplus 1\%$	± 2.5	-
EM calorimetry	$\sigma_E/E = 10\%$, $\sqrt{E} \oplus 0.7\%$	± 3.2	± 2.5
Hadronic calorimetry (barrel and end cap)	$\sigma_E/E = 50\%$, $\sqrt{E} \oplus 3.0\%$	± 3.2	± 3.2
Hadronic calorimetry (forward)	$\sigma_E/E = 100\%$, $\sqrt{E} \oplus 10.0\%$	$3.1 < \eta < 4.9$	$3.2 < \eta < 4.9$
Muon spectrometer	$\sigma_{p_T}/p_T = 10\%$ at $p_T = 1$ TeV	± 2.7	± 2.4

3.5 Inner Detector

The Inner Detector is located around the beam pipe at the collision point, and covers a range of $5 < r < 120$ cm and $|\eta| < 2.5$. It consists of three sub-detectors, two silicon based detectors; the Pixel Detector and the SiliCon Tracker (SCT), and a straw tube gaseous detector; the Transition Radiation Tracker (TRT), all of which are surrounded by the inner solenoid, a 2T magnet positioned on the inner side of the electro-magnetic calorimeter. These are shown in fig. 7.

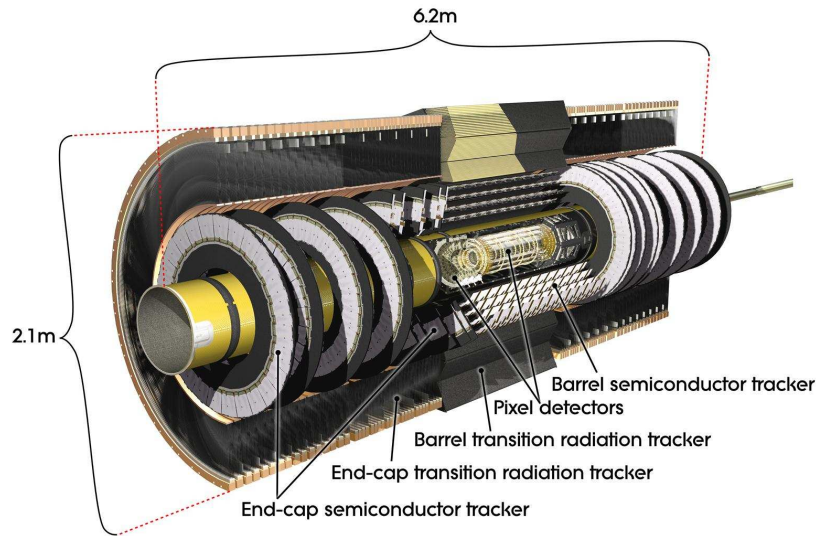


Figure 7: The cut away view of the inner detector with the sub systems labelled [28].

The three sub-detectors are used to determine the location of the primary vertex and any secondary vertices, to aid in particle identification and for charged particles to measure both the momentum and the sign of the charge from the curvature of the track. The inner detector hardware was chosen so as to

withstand the high radiation environment that it will be subjected to during data taking, and unless stated otherwise all components are built to survive at least ten years of operation at the LHC.

To ensure good track parameter resolution the location of the sensory elements must be known to within a few micrometers. This is mostly achieved by an alignment procedure using tracks. The SCT also has a built in interferometer based alignment monitoring system [36] that under pins these regular track based alignment procedures.

The amount of material within the ID is kept to a minimum as any materials traversed by an outgoing particle can cause Coulomb scattering, bremsstrahlung, photon conversions or secondaries from nuclear reactions, all of which can effect the accuracy of the track measurement. The amount of material in each sub-detector is shown as a function of of η in fig. 8.

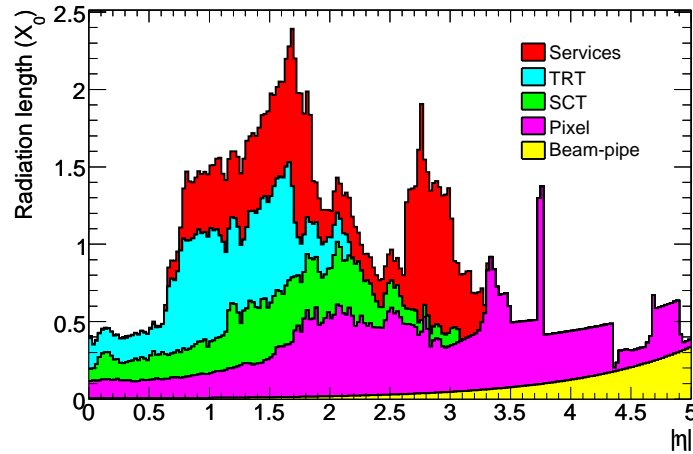


Figure 8: Cumulative amount of material in terms of radiation length for the Inner Detector as a function of $|\eta|$ [37].

Another source of error on the track measurements is the exact value of the magnetic field from the solenoid surrounding the ID. Prior to the installation of the ID, after only the barrel and endcap calorimeters were in place, a mobile array of Hall probes were used to map out the magnetic field in the volume to be occupied by the ID. To monitor any changes in this magnetic field during running four Nuclear Magnetic Resonance (NMR) probes are used, located near to $z = 0$ cm.

The inner detector does not contribute to the L1 trigger decision, and therefore all of digitized data from a single event is simply stored in a buffer and only passed to the off detector electronics if the L1 trigger accepts the event.

3.5.1 Pixel detector

Located closest to the beam pipe is the pixel detector. The pixel detector consists of 1744 identical pixel sensors, spread out across three barrel layers and two lots of three end cap disks. Each pixel sensor has 47232 pixels, each of size $50 \times 400 \mu\text{m}$, and is bump bonded to an element of the front end readout integrated circuit [34]. The three barrel layers are concentric cylinders around the beam axis located between $50.5 < R < 122.5 \text{ mm}$. The proximity of the barrel layers to the beam means that the innermost layer will have to be replaced after about three years of running due to radiation damage. The end cap disks are aligned perpendicular to the beam axis, and are located at both sides A and C of the detector. These are also $250 \mu\text{m}$ thick. The pixel layers are segmented in $R - \phi$ and z , and typically three pixel layers are crossed by each track. The intrinsic measurement accuracies for each of the layers and disks are $10 \mu\text{m}$ in the $R - \phi$ plane and $155 \mu\text{m}$ along the z axis, which is sufficient for high precision tracking measurements.

3.5.2 Silicon Tracker (SCT)

Additional tracking measurements are provided by the SCT, which is located further out from the beam than the pixel detector, and again consists of a barrel region and two end caps. Located at $255 < R < 549 \text{ mm}$ is the barrel region, which consists of four cylindrical layers. There are 2112 barrel SCT modules shared out across the four layers. Each module consists of four silicon sensors, two of each on the top and bottom, all with $80 \mu\text{m}$ pitch micro-strip sensors. The front and back sensors are aligned with a stereo angle of 40 mrad and are connected to binary signal readout chips. The shallow stereo angle reduces the number of ambiguities for a particle passing through a module, and also simplifies the geometrical layout of the module. The modules are orientated such that the bottom sensor is aligned with the beam line. The precision of each of the barrel SCT modules in the $R - \phi$ co-ordinate is $17 \mu\text{m}$ and $580 \mu\text{m}$ for the z co-ordinate.

In order to maximise the η coverage there are also nine disk layers in each of the two end caps arranged perpendicular to the beam axis. This ensures that there are at least four precision space-point measurements for each track within the fiducial detector coverage. The layout of the modules in the end caps is such that the accuracy of each of the end cap SCT modules in the $R - \phi$ co-ordinate is $17 \mu\text{m}$ and $580 \mu\text{m}$ for R .

In order to maintain an acceptably low level of noise during data taking and reduce increases in the required bias voltage the SCT is kept at a temperature around 0°C .

3.5.3 Transition Radiation Tracker (TRT)

The outer-most region of the inner detector is occupied by the TRT, located at $554 < R < 1082$ mm. It covers the region $|\eta| < 2.0$ and enables charged particles to be tracked right through to the calorimeters. The TRT contains many polyamide tubes of thickness 4 mm, each made of two $35 \mu\text{m}$ thick multi-layer films bonded back to back, immersed in an Argon based gas mixture. Each straw tube is inter-leaved with transition radiation material and has at its centre anode wires which are read out at either end of the straw. When passing through the numerous dielectric boundaries of each straw ultra relativistic particles produce transition radiation photons which ionise the gaseous mixture and enhance the signal.

The TRT consists of barrel and end cap regions. The barrel straws, of length 144 cm, run parallel to the beam line, and cover the region $|\eta| < 1.0$. Perpendicular to these in the end cap regions are radial straws of length 37 cm, these cover the region $1.0 < |\eta| < 2.0$. Each straw has an intrinsic accuracy $130 \mu\text{m}$ in the $R - \phi$ direction. Approximately 36 hits are expected for a charged particle passing through the TRT, and the precise measurement of the timing of these hits, together with the fact that these hits are spread out over a larger distance than that of the innermost detectors, means that the TRT contributes significantly to the accuracy of the momentum measurement of charged particles.

3.5.4 Inner detector performance

Fig. 9(a) shows the MC and data comparison for the vertex resolution of the ID in the x direction for data taken in 2011 [37]. Similar agreement is also observed for the y and z directions. Fig. 9(b) shows the invariant mass distribution of $Z \rightarrow \mu\mu$ decays from the 702 pb^{-1} of data collected during spring 2011. The mass is reconstructed using track parameters from the ID track of combined muons only. Two different sets of alignment constants for the data are compared with the ideal alignment performance based on MC predictions.

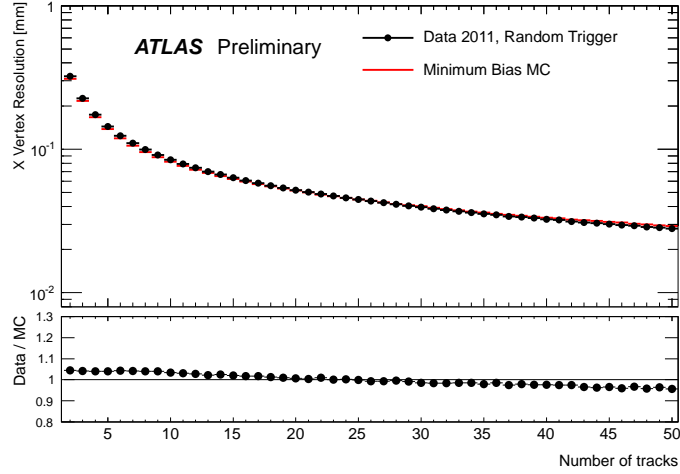
3.6 Calorimeters

The ATLAS calorimeters are positioned outside the 2 T solenoid magnet surrounding the inner detector. The purpose of a calorimeter is to measure the energy of incident particles. There are two types of calorimeter used in ATLAS.

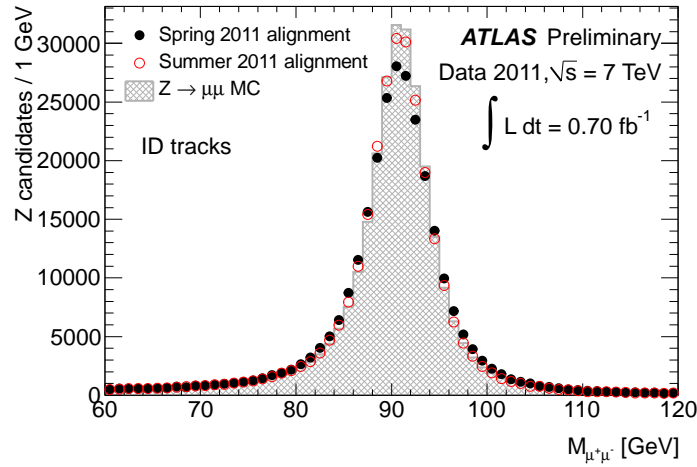
The electro-magnetic calorimeter (EMCAL) measures the energy of electro-magnetically interacting particles and the hadronic calorimeter (HCAL) does the same for strongly interacting particles. Both consist of a barrel calorimeter and two endcaps and give complete ϕ coverage. This is necessary for the accurate reconstruction of missing energy, which is of particular importance to the physics analyses

described in this thesis. Fig. 10 shows the layout of the ATLAS calorimeters.

The depth of the calorimeters is chosen to maximise the containment of electro-magnetic and hadronic showers and thus minimise the punch through of jets into the muon system. In total at $\eta = 0$, which corresponds to the thinnest part, the calorimeters are approximately 11 interaction lengths thick, which has been shown to reduce punch through to an acceptable level [35].



(a)



(b)

Figure 9: (a) Data and MC comparison of the vertex resolution as a function of the number of tracks for 2011 data. (b) The invariant mass of muons using only information from the tracks for 702 pb^{-1} of 2011 data. The black and red dots indicate two different sets of alignment constants.

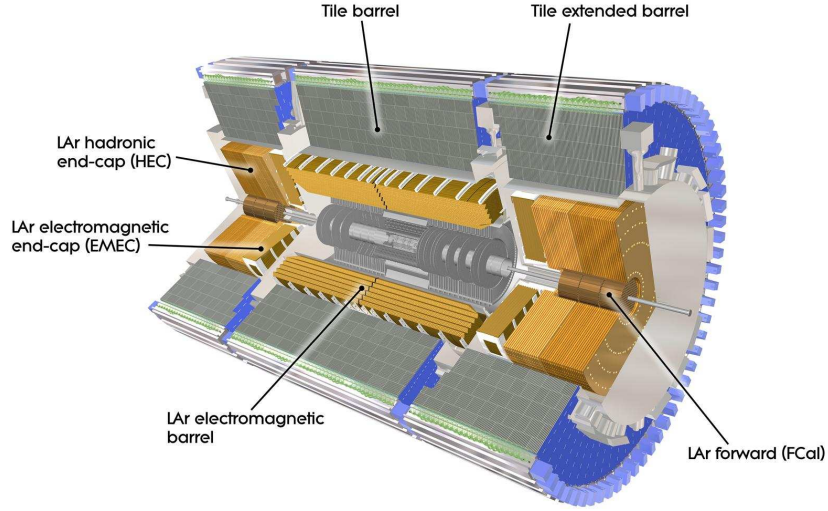


Figure 10: The cut away view of the calorimeters [28].

3.6.1 Electro-magnetic calorimeters

The EMCAL measures the energies of incident photons and electrons, and helps distinguish between different particle types by accurately measuring the shape of the resulting electro-magnetic shower. It also measures the electro-magnetic component of incident jets.

The LAr EMCAL uses lead as its absorber and the detection medium is liquid Argon. The LAr is kept at -88°C in a cryostat. The EMCAL consists of 3 parts, the barrel part ($|\eta| < 1.475$) and two end cap parts ($1.375 < |\eta| < 3.2$). The barrel part itself is made of two identical half barrel parts, separated by a small gap of 4 mm at $z = 0$ and the end caps are split into two wheels, the outer wheel ($1.375 < |\eta| < 2.5$) and the inner wheel ($2.5 < |\eta| < 3.2$). The absorber layers have an accordion shaped geometry, as shown in fig. 11, which allows for complete ϕ coverage without any azimuthal cracks. In the barrel the absorber layers are parallel to the beam line and are stacked along the ϕ direction where as in the end caps the accordion waves are aligned with the radial direction.

In the pseudorapidity range matched to the inner detector, $|\eta| < 2.5$, the calorimeter is split up into 3 layers to measure the variation in shower shape as a function of depth. The first layer has the finest ϕ granularity and is used for detailed ϕ measurements. The second layer is where most of the electro-magnetic shower will be absorbed, and the third layer is used to measure possible leakage into the hadronic calorimeter. An additional layer, referred to as the presampler, is positioned in the region $|\eta| < 1.8$ and is used to estimate energy loss of photons and electrons before they reach the first main

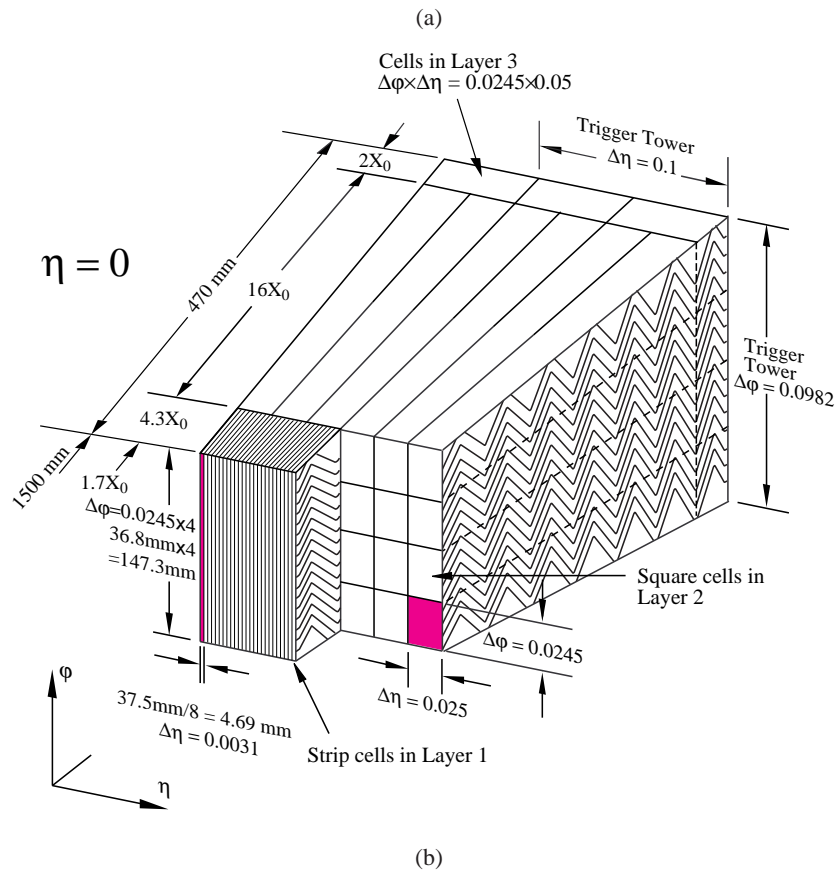
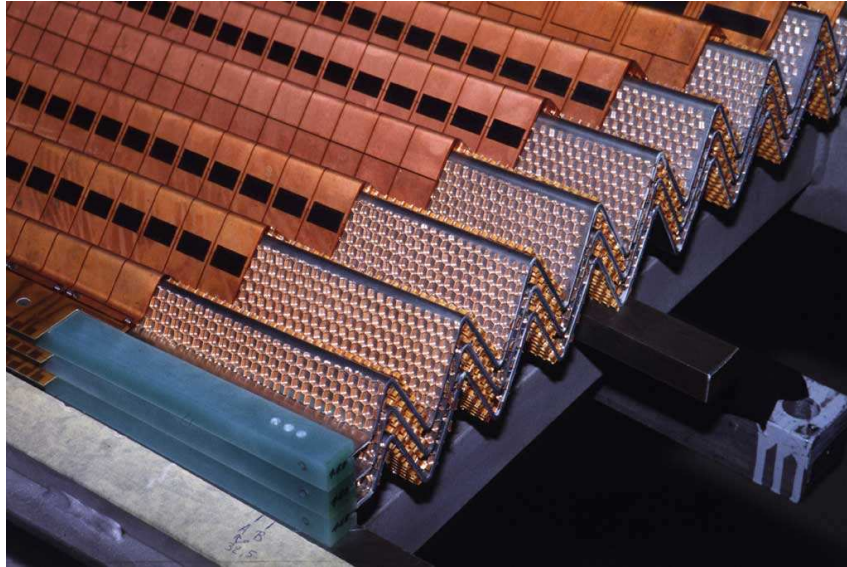


Figure 11: (a) Photo of the EMCAL during construction, showing the three layers and the accordion geometry [28] and (b) a schematic view of the part of the barrel section of the EMCAL.

layer. It has a very fine granularity in pseudorapidity which helps the p_T resolution as well as γ/π^0 separation [31].

3.6.2 Hadronic calorimeters

The hadronic calorimeters are used to measure the strongly interacting component of the incident jets, and absorb all particles that have passed through the EMCAL except muons.

Along with the forward calorimeters there are two hadronic calorimeters used in ATLAS. Both calorimeters employ a different technology depending on the performance requirements in the different regions of the ATLAS detector. The tile calorimeter (HCAL) uses scintillating tiles for the sampling medium and steel as the absorber. It is made of three barrel calorimeters, a central barrel of length 5.8 m, and two extended barrels, each 2.6 m in length and in total covers the pseudorapidity range $|\eta| < 1.7$. The scintillating light in the tiles is read out by fibres connected to photomultiplier tubes located outside the barrels.

The hadronic endcap calorimeters (HEC) are located in the pseudorapidity region $1.5 < |\eta| < 3.2$. Like the EMCAL they use LAr as the detection medium due to the high radiation conditions present at this location, but they use copper for the absorber.

Further calorimetry is located in the forward region of the detector, referred to as the forward calorimeter (FCal). The FCal is comprised of three longitudinal sections, the first of which is copper based and measures the EM component of very forward jets. The second and third sections are tungsten based and are used to measure forward hadronic activity. The FCal covers the pseudorapidity range $3.1 < \eta < 4.9$ and ensures that the ATLAS calorimeters have a large η coverage.

3.6.3 Calorimeters summary

Dedicated hardware is used to compute the calorimeter Level 1 trigger decision (see section 3.8). Fig. 11(b) shows the coarse granularity trigger towers (0.1×0.1 in $\Delta\eta \times \Delta\phi$) in the EMCAL, and similar sized towers are used in the HCAL. Analogue signals from these towers are read out and used to associate the event to a particular bunch crossing and calculate the E_T for each tower. The data are then transmitted to two separate sub-systems, one for identifying jet candidates and the other for identifying electron, photon and τ candidates [35]. Within a time of $2.1 \mu\text{s}$, this information is sent to the L1 central trigger processor allowing the decision to be completed within the target time of $2.5 \mu\text{s}$.

The η coverage and the thickness in terms of interaction length of all the calorimeters is displayed in fig. 12. The p_T , η and ϕ distributions for electrons and jets, which are mostly measured using the

calorimeter, for the 2011 dataset are shown in chapter 4.

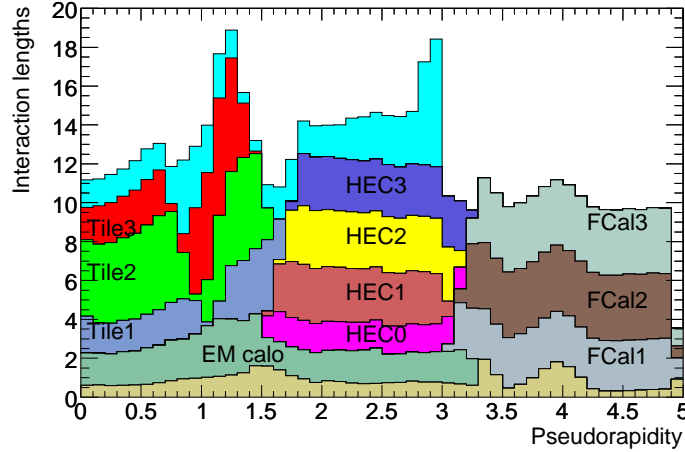


Figure 12: Cumulative amount of material in terms of interaction length for all of the calorimetry in ATLAS. The plot demonstrates the full η coverage of all of the calorimetry in ATLAS [35]. The unlabelled cyan band corresponds to the amount of material before the first active layer of the MS and the band below the EM Calo and FCAL 1 is the ID.

3.7 Muon spectrometer

The muon spectrometer (MS) is located outside of the calorimeters and covers the pseudorapidity range $|\eta| < 2.7$ [33]. It is used to detect and measure the momenta of muons, the only particles from the p-p interactions at the centre of ATLAS which make it through the calorimeters, except for neutrinos which do not interact with the detector at all. It consists of trigger chambers, which cover $|\eta| < 2.4$ and contribute to the L1 trigger decision, and precision tracking chambers which measure the trajectories of the muons from which the momenta can be inferred.

Three large superconducting air-core toroid magnets bend the trajectories of muons traversing the MS. In the barrel ($|\eta| < 1.4$) the 8 coils of the toroid magnet are housed individually in 25.3 m long cryostats which use liquid helium to keep the coils at 4.6 K. This toroid magnet provides a 0.5 T field. Two smaller, but more powerful toroid magnets are located in each of the end caps in the range $1.6 < |\eta| < 2.7$ and supply a 1.0 T field. For the pseudorapidity range $1.4 < |\eta| < 1.6$ magnetic deflection is provided by a combination of the two fields. This configuration, shown in fig. 13, provides a magnetic field which is mostly orthogonal to the muon trajectories.

To achieve the momentum resolution quoted in table 2 a detailed knowledge of the uniformity of the

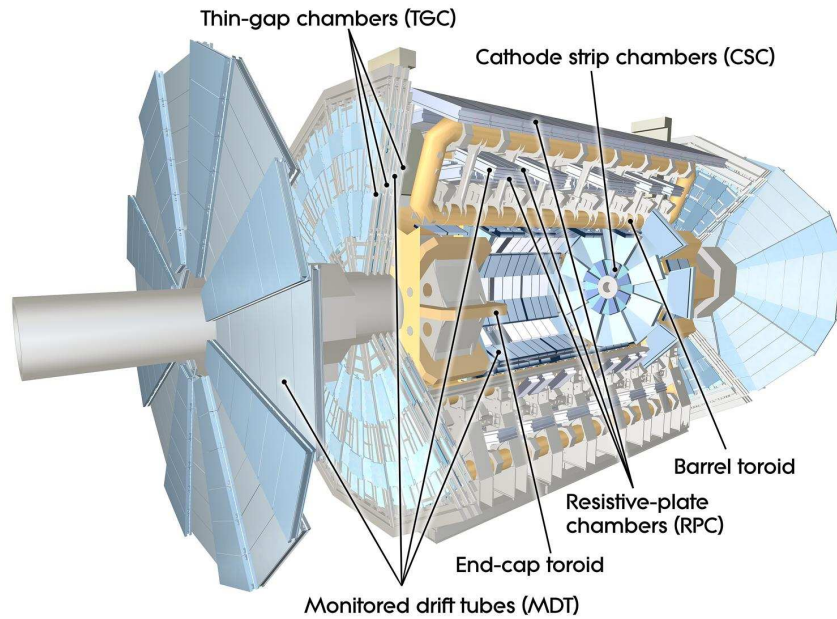


Figure 13: Cut away view of the ATLAS muon system [28].

magnetic field is required. The vast conductors that make up the toroids are shifted under the magnetic and gravitational load they are subjected to, making it difficult to predict the exact position of all the components, and hence to calculate the magnetic field they produce to the required accuracy. Therefore the field produced from each of these conductors is measured during running by 1730 Hall sensors mounted onto the precision tracking chambers. The Hall probe measurements are then compared with field calculations to determine the position and shape of the toroid conductors with respect to the MS. Two NMR sensors are also positioned in the barrel to detect any long term drift in the response of the 3-D Hall sensors.

In the barrel region there are 8 symmetrical precision tracking chambers located on and between the 8 coils of the barrel toroid magnet. Each of the 8 chambers has 3 concentric layers that are approximately positioned at $R = 5, 7.5$ and 10 m. For the endcaps a precision chamber is located both in front and behind each of the endcap toroid magnets. These wheel-shaped chambers are positioned perpendicular to the beam line at $|z| \approx 7.4, 10.8, 14.0$ and 21.5 m. For the majority of the MS the tracking chambers are Monitored Drift Tube (MDT) chambers. There are 1150 MDTs in the MS, each comprised of a pair of drift tube multi-layers, which themselves are made up of either 3 or 4 monolayers. For a charged particle traversing the MDTs approximately $20 z/r$ track position measurements are made, with resolutions of $80 \mu\text{m}$ per drift tube, or $35 \mu\text{m}$ per MDT. In the first layer of the endcaps, corresponding to a pseudora-

pidity range of $2.0 < |\eta| < 2.7$ where the rate of muons is expected to be highest, the precision tracking chambers are Cathode Strip Chambers (CSC). These have a higher granularity than the MDTs and higher rate capabilities to cope with the high rate of incident muons.

Dedicated high rate Resistive Plate Chambers (RPCs) positioned in the barrel are used to trigger on events with muons. There are 606 RPCs in the MS, and they provide 6 position measurements for each charged particle traversing them. The ϕ and z components of the muons are measured with a spatial resolution of 1 cm, and with a time resolution of 1 ns. In the endcaps the trigger chambers are Thin Gap Chambers (TGCs). Each TGC unit contains anode wires running parallel to the MDT wires that will provide a measurement of the r co-ordinate with a 2 – 3 mm spatial resolution and a 4 ns temporal resolution. Separate orthogonal anode wires measure the ϕ co-ordinate with a 2 – 3 mm and 4 ns spatial and temporal resolution respectively.

The p_T , η and ϕ distributions for muons in the 2011 dataset are shown in chapter 4 fig. 18.

3.8 Triggers

The 50 ns bunch spacing used for the majority of 2011 and all of 2012 corresponds to a raw data rate of 20 MHz, and at its design 25 ns bunch spacing the ATLAS detector is required to cope with a raw event rate a factor of 2 higher. Therefore fast online trigger decisions need to be made in order to determine which of the events to write out to disk.

The online event selection is done in three stages, and eventually brings the rate down to below 200 Hz. The criteria required to pass each of the three trigger levels can be altered using a trigger menu, allowing the triggers to be adjusted to the different running conditions of the detector. The first decision is made by the Level 1 (L1) trigger, which uses information from the custom built hardware in the calorimeters and muon chambers to identify interesting events and the regions of interest (ROIs) within these events, which are used later in the L2 trigger decision. There are separate L1 triggers for physics objects, such as muons, electrons and photons, jets and τ leptons. It is also possible to trigger on global properties of an event, such as large E_T^{miss} and the sum of the transverse energy. The L1 trigger is designed to bring the data rate down from 40 MHz to approximately 75 kHz [34]. The next step in the trigger chain is the Level 2 (L2) trigger which uses a more refined event selection to reduce the rate to below 3.5 kHz. The full detector is used in this decision, including the ID which enables the separation of events containing electrons and photons. Finally the most complex event selection criteria are applied at the event filter (EF) level which is applied on fully-built events. The reconstruction algorithms used at this stage are similar to those used in the full ATLAS reconstruction, but optimised for the online

environment. The EF trigger brings the rate down to the desired 200 Hz. The events are then separated into different streams and recorded for offline analysis.

Throughout data taking of 2011 and 2012 the triggers successfully coped with the high instantaneous luminosity whilst maintaining low p_T thresholds on all physics objects. Fig. 14 shows the EF rates of the lowest p_T unprescaled single electron triggers as a function of luminosity during the 2011 run. A similar plot for muons can be found in [38].

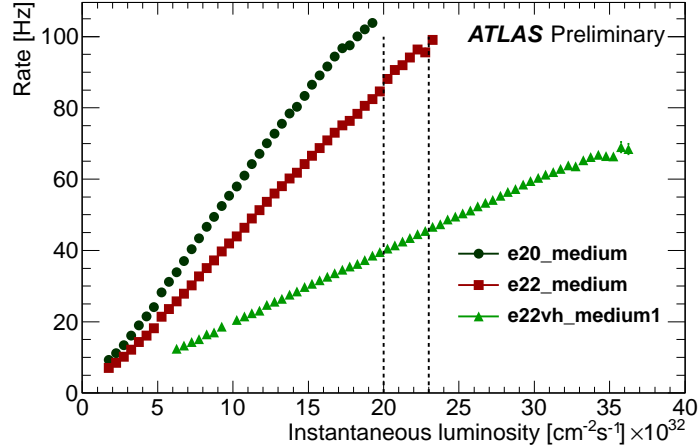


Figure 14: The unprescaled EF trigger rates for single electrons. The vertical lines indicate the instantaneous luminosity at which the triggers were no longer the main triggers used in physics analyses [39]. In the trigger names in the legend the number corresponds to the minimum p_T , and the letters *vh* indicate that isolation requirements are applied.

3.9 Luminosity

Hardware specifically designed to measure the LHC luminosity delivered to the ATLAS detector is located in the very forward regions of the detector. It was a design goal of ATLAS to measure the luminosity with an uncertainty of less than 5%. The actual uncertainties for the complete 2011 and 2012 datasets are 3.9% and 3.6% respectively. Two detectors are used to achieve this low uncertainty; LUCID (LUMinosity measurement using Cerenkov Integrating Detector) and ALFA (Absolute Luminosity For ATLAS). LUCID is located at $z = \pm 17$ m and is the main detector used for luminosity measurements. It is used to monitor the instantaneous luminosity and beam conditions. It consists of 20 aluminium tubes, 1.5 m in length and 15 mm in diameter, pointing back towards the interaction point each filled with C_4F_{10} gas. Forward particles from inelastic p-p scattering traverse these tubes and emit Cerenkov

light, which is then measured in photo multiplier tubes (PMTs). The signal amplitude from these PMTs can be used to determine the number of incident particles traversing the tubes. The signal is read out at a rate faster than the bunch crossing rate so that the luminosity for each bunch crossing can be determined.

ALFA is located at $z = \pm 240$ m and lies only 1 mm away from the beam. It measures the elastic scattering cross-section at small angles from which the total cross-section can be determined, and the luminosity extracted [35]. It consists of a stack of 10 double-sided scintillating-fibre modules which are read out using PMTs. The small angles at this z distance are smaller than the nominal beam divergences, and so ALFA is only used during special run conditions in order to calibrate LUCID.

3.10 Summary

In general the sub-detectors and detector systems described above have performed very well during data taking. A summary of the efficiencies during 2011 of each of the sub-detectors is given in table 3.

Sub-system	Sub-detector	Efficiency (%)
Inner Detector	Pixel	100
	SCT	99.3
	TRT	99.5
Calorimeters	LAr	97.2
	Tile	99.6
Muon Detectors	MDT	99.9
	RPC	99.8
	CSC	100
	TGC	99.8
Trigger	L1	99.8
	HLT	100
Magnets	Solenoid	99.7
	Toroid	99.3
Luminosity		99.8

Table 3: Summary of the channel efficiencies of the ATLAS sub-detectors during 2011.

Chapter 4

Reconstruction

This section describes the reconstruction of physics objects in the ATLAS detector and the data taken from 2010 up to the end of 2012. The physics objects described here are those most relevant to the analyses presented in chapters 5,6 and 7. The description focuses mainly on the reconstruction as used in the $H \rightarrow ZZ \rightarrow ll\nu\nu$ search described in chapter 6 which uses the 2011 dataset. Plots showing reconstructed objects are taken from that search. The $ZH \rightarrow ll + inv$ search uses the both the 2011 and 2012 dataset. It is highlighted when there are significant changes between the reconstruction in 2011 and 2012.

The description of the data is split up into three periods that correspond to each year of data taking.

- The $H \rightarrow ZZ \rightarrow ll ll$ search described in chapter 5 and [40] uses the 2010 dataset, as does a preliminary search in the $H \rightarrow ZZ \rightarrow ll\nu\nu$ [1].
- The $H \rightarrow ZZ \rightarrow ll\nu\nu$ analysis described in chapter 6 and [3] uses the 2011 dataset.
- The $ZH \rightarrow ll + inv$ search described in chapter 7 and [5] uses the 2011 dataset and part of the 2012 dataset.

4.1 Data

During an LHC fill after stable beams have been declared the sub-systems of the ATLAS detector must be declared ready to record data. Any time lost whilst waiting for these sub-detectors to become fully operational can be seen as a difference in delivered and recorded luminosity. Fig. 15 shows the delivered and recorded luminosities as a function of time for each year of running. Small efficiency losses relate to the turn on time of the high voltage of the pixel, SCT and muon detectors and also to time lost whenever a problem with a sub-detector prevents any data taking [41].

When a sub-detector is offline, noisy or under efficient during a run but the run continues the loss in luminosity is not shown in fig. 15, but the run and luminosity block numbers are flagged and a defect is recorded. The severity of defects is determined offline and a decision of whether or not to include the affected data is implemented via a Good Runs List (GRL).

A GRL is a list of run and luminosity block numbers for which all of a given set of sub-detectors were operational at an acceptably high efficiency. The requirement used to define a GRL may vary depending

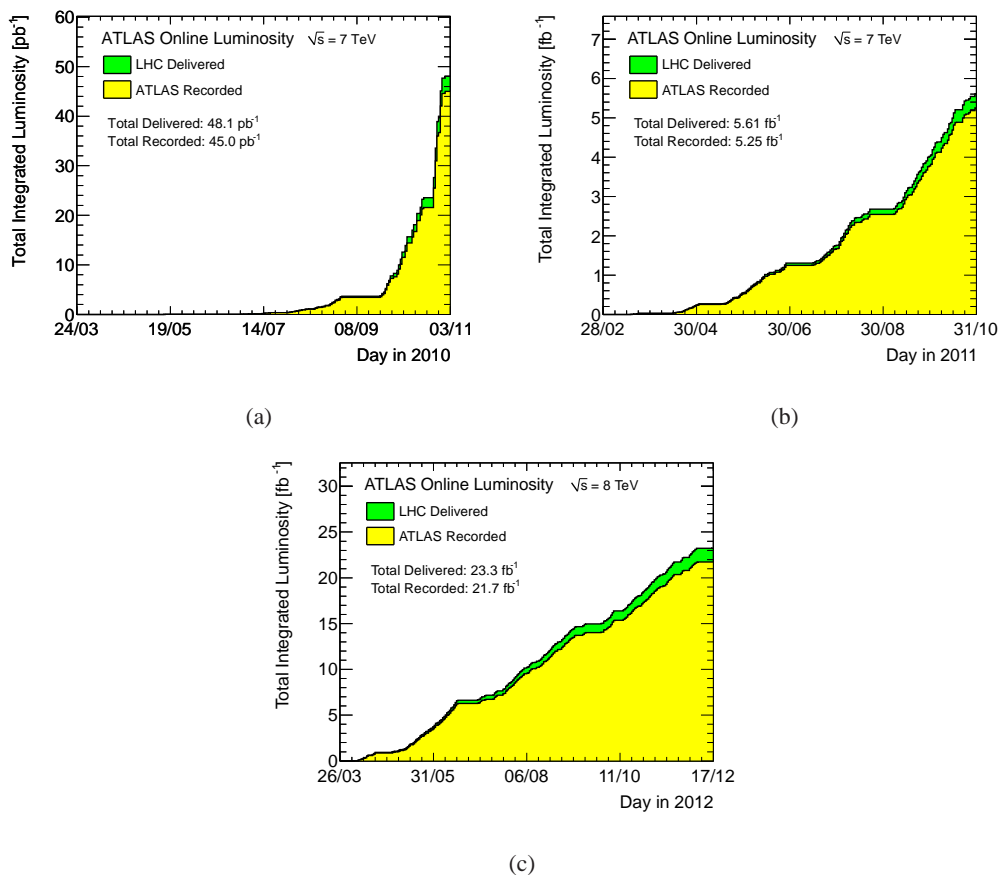


Figure 15: Cumulative luminosity versus day in (a) 2010, (b) 2011 and (c) 2012. The luminosity delivered (green), and recorded by ATLAS (yellow) during stable beams are shown. The total delivered and recorded integrated luminosities are written on each figure. [41]

on the intended use. For example if one were only interested in the electron performance one would require a GRL where the ID and calorimeters were fully operational, but it would not matter if there was a fault in the MS. Hence such an analysis could use a GRL that include runs during which MS defects occurred. From 2011 onwards GRLs were centrally produced so that different physics analyses with similar detector requirements could use the same datasets. The integrated luminosity of a dataset used in a given analysis is calculated from the GRL to account for any missing runs or luminosity blocks.

The details of each dataset are given in 4.1.1, 4.1.2 and 4.1.3.

4.1.1 The 2010 dataset

In July 2010 the LHC started colliding proton-proton beams together at a centre-of-mass energy of 7 TeV and continued until the heavy ion collisions started in November that year. During this time the

peak instantaneous luminosity was $2 \times 10^{32} \text{cm}^{-2}\text{s}^{-1}$ and the number of interactions per bunch crossing (denoted by $\langle \mu \rangle$) varied between 0 – 4. The time between bunch crossings was 75 ns. The total delivered (recorded) luminosity was 45445.7 (44060.7) nb^{-1} . The cumulative luminosity delivered and recorded per day in 2010 is shown in fig. 15 (a).

4.1.2 The 2011 dataset

During 2011 the beams continued to collide at $\sqrt{s} = 7 \text{ TeV}$. For the majority of the data the time between bunch crossings was 50 ns, although 12 pb^{-1} were taken with 75 ns. Compared to 2010 the number of protons within each bunch was increased and the peak instantaneous luminosity was $3.65 \times 10^{33} \text{cm}^{-2}\text{s}^{-1}$, over a factor of 10 higher; as a result $\langle \mu \rangle$ increased. The luminosity weighted $\langle \mu \rangle$ distribution for 2011 is shown in fig. 16. In this figure the complete 2011 dataset has been split up into two sub-datasets, corresponding to runs before and after a technical stop in September 2011, during which β^* , a parameter related to the transverse beam size, was reduced from 1.5 m to 1 m. It can be seen that the different β^* s have a large effect on the $\langle \mu \rangle$ values. The effect of a larger $\langle \mu \rangle$ on physics analyses is discussed in 4.1.4.

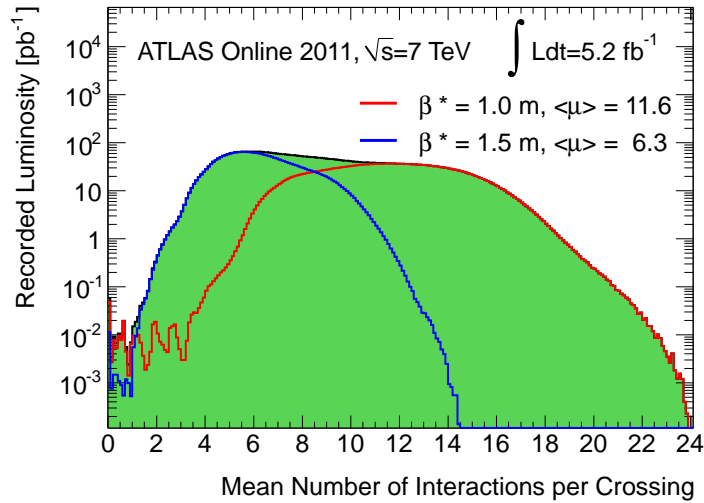


Figure 16: The mean number of interactions per crossing for the 2011 dataset. The blue line indicates data taken before the September technical stop ($\beta^* = 1.5$) and the red line after ($\beta^* = 1.0$). The average number of collisions per bunch crossing for each sub-dataset is given on the figure.

During the early part of data taking a number of cells in the LAr calorimeter were lost due to problems with the optical readout electronics. Additionally for a fraction of the data a problem with the front-end board electronics meant that certain regions of the electro-magnetic calorimeter were inactive. The

number of lost cells changes with time and is included in the simulation of the Monte Carlo samples. For analyses using the 2011 dataset an Object-Quality cleaning procedure was provided to remove electrons in fiducial regions around these lost cells. The procedure is applied to both the data and the MC.

The cumulative luminosity delivered and recorded throughout 2011 is shown in fig. 15(b). The total integrated luminosity recorded by ATLAS in 2011 is 5.25 fb^{-1} .

4.1.3 The 2012 dataset

During the winter shutdown between 2011 and 2012 the decision was taken to increase the LHC centre-of-mass energy to 8 TeV. This increased the cross section for rarer processes including Higgs production. The peak instantaneous luminosity was $7.73 \times 10^{33} \text{ cm}^{-2} \text{ s}^{-1}$. The 2012 dataset used for the $ZH \rightarrow ll + inv$ search presented in chapter 7 has an average $\langle \mu \rangle$ of 20. Fig. 17 shows the $\langle \mu \rangle$ distribution for the first 14 fb^{-1} of 2012, compared to that of 2011.

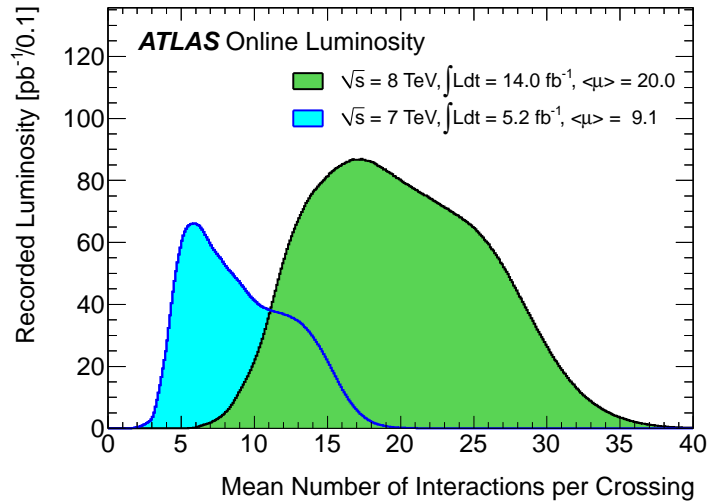


Figure 17: The luminosity-weighted distribution of the mean number of interactions per crossing for the 2011 and 2012 data.

The cumulative luminosity delivered and recorded throughout 2012 is shown in fig. 15 (c). The total integrated luminosity recorded by ATLAS is 21.7 fb^{-1} . The dataset used for the $ZH \rightarrow ll + inv$ analysis presented in chapter 7 is that taken up to September of 2012, and corresponds to 13 fb^{-1} .

4.1.4 Pileup

In general pile-up refers to additional interactions that occur alongside the hard interaction of interest. There are two types of pile-up, referred to as in-time and out-of-time pile-up. In-time pile-up refers to additional proton-proton interactions occurring in the same bunch crossing as the hard interaction of interest. Such interactions produce extra soft particles in the detector which can affect the performance. Higher numbers of pile-up events, higher $\langle \mu \rangle$, increase the impact on an analysis.

Out-of-time pile-up refers to detector performance effects due to interactions in preceding bunches. These effects scale with the beam intensity in bunches preceding the one during which a collected event occurred. This effect is accounted for in the 2011 and 2012 Monte Carlo samples which assume a 50 ns bunch spacing, which was the bunch spacing for the majority ($> 99.5\%$) of the data taken. As the out-of-time pile up effects depend on the intensity of several prior bunches, the position of a bunch within the bunch train is important.

4.2 Muons

Muons are identified by reconstructing tracks in the muon spectrometer using the STACO algorithm [34]. This algorithm starts from regions of activity (ROA) in the muon spectrometer identified by the TGC/RPC systems, local segments are then formed within each of these ROAs using straight line approximations. These segments are then combined taking into account the non-linear trajectory of muons due to the magnetic field. Finally a more accurate global track fit using all hit information from the muon system is performed. The obtained tracks are extrapolated to the beam line and an attempt is made to find a matching inner detector track [42]. If a match is found, a combined muon is formed incorporating the information from both detectors, otherwise a stand-alone muon is formed.

For the analyses presented in chapters 6 and 7 only combined muons are used (although stand alone muon information is used when determining missing energy). Combined muons give the best performance over a wide range of muon momenta due to the two independent measurements of the momentum. In general the ID dominates the measurement for muons with low p_T in both the barrel and the end caps. The MS dominates for high p_T muons.

The analysis presented in chapter 5 uses combined, stand alone muons and tagged muons. Tagged muons are muons that have an inner detector track but do not have a complete track in the MS. Further cuts are applied to the muons. The inner detector track associated to the muon is required to pass a series of additional cuts based on the number of hits and holes (absence of hits) in the various layers of the inner detector (see Table 4). Muons from cosmic rays are suppressed by requiring the impact parameter with

respect to the primary vertex satisfy $|d_0| < 1$ mm and $|z_0| < 10$ mm where d_0 and z_0 are the transverse and longitudinal impact parameters respectively. A track isolation requirement is applied to reject muons originating from heavy flavour quark decays. The sum of the p_T of all the tracks that lie within a cone of $\Delta R = 0.2$ of a muon is required to be less than 10% of the p_T of the muon itself. The track of the muon itself is not included in the sum.

Small inaccuracies in the simulation of the muon momentum scale ($< 1\%$), resolution ($< 3\%$ for MS, $< 1\%$ for ID) and selection efficiencies ($< 1\%$) are corrected for in Monte Carlo; muon momenta are smeared, and weights are applied to account for the difference in efficiency. The muon momentum resolution and p_T scale is determined from the width of $Z \rightarrow \mu\mu$ decays and by comparison of the two individual tracking measurements from the ID and MS. The smearing is applied as a function of p_T and is applied separately to the ID and MS tracks. A momentum scale correction is also applied. There are three contributing factors to the overall reconstruction efficiency of combined muons; the reconstruction efficiency in the ID, the reconstruction efficiency in the MS and the matching efficiency between these measurements. Both the ID efficiency and the MS together with the matching efficiency are measured using a tag and probe method. Muons from $Z \rightarrow \mu\mu$ decays are selected where one muon (the tag) is required to be a combined muon and the other (the probe) is a muon with either a MS or ID track only [43]. The efficiency is calculated as a function of p_T , η and ϕ . The uncertainty in the determination of the efficiency of muons is accounted for in the analyses by adjusting the weight applied to each muon.

The p_T , η and ϕ distributions of the muons forming the leptonic Z boson candidate are shown in fig. 18. It can be seen that the simulation provides a reasonable description of the data, although there is a modest discrepancy in the η distribution, which is more central in the data than in the Monte Carlo. This is a known feature of the η distribution of leptons from the Alpgen Z boson production simulation, and will be discussed further in sub-section 6.7. A summary of the muon selection is given in table 4.

4.3 Electrons

The reconstruction of electrons with $|\eta| < 2.5$ is performed using a variety of discriminating variables from both the calorimeters and the inner detector [34]. Calorimeter variables used are hadronic leakage, lateral shower shape (R_η), lateral shower width (weta2) and shower shape variables from the first layer of the ECAL. The hadronic leakage is the ratio of the transverse energies of clusters measured in the hadronic and electro-magnetic calorimeters, the exact definition of the variable depends on $|\eta|$. R_η is the ratio of the sum of uncalibrated energy cells within two different sized rectangles on the second sampling layer of the ECAL. Weta2 is related to the spread of the energy deposits over η . The high granularity of

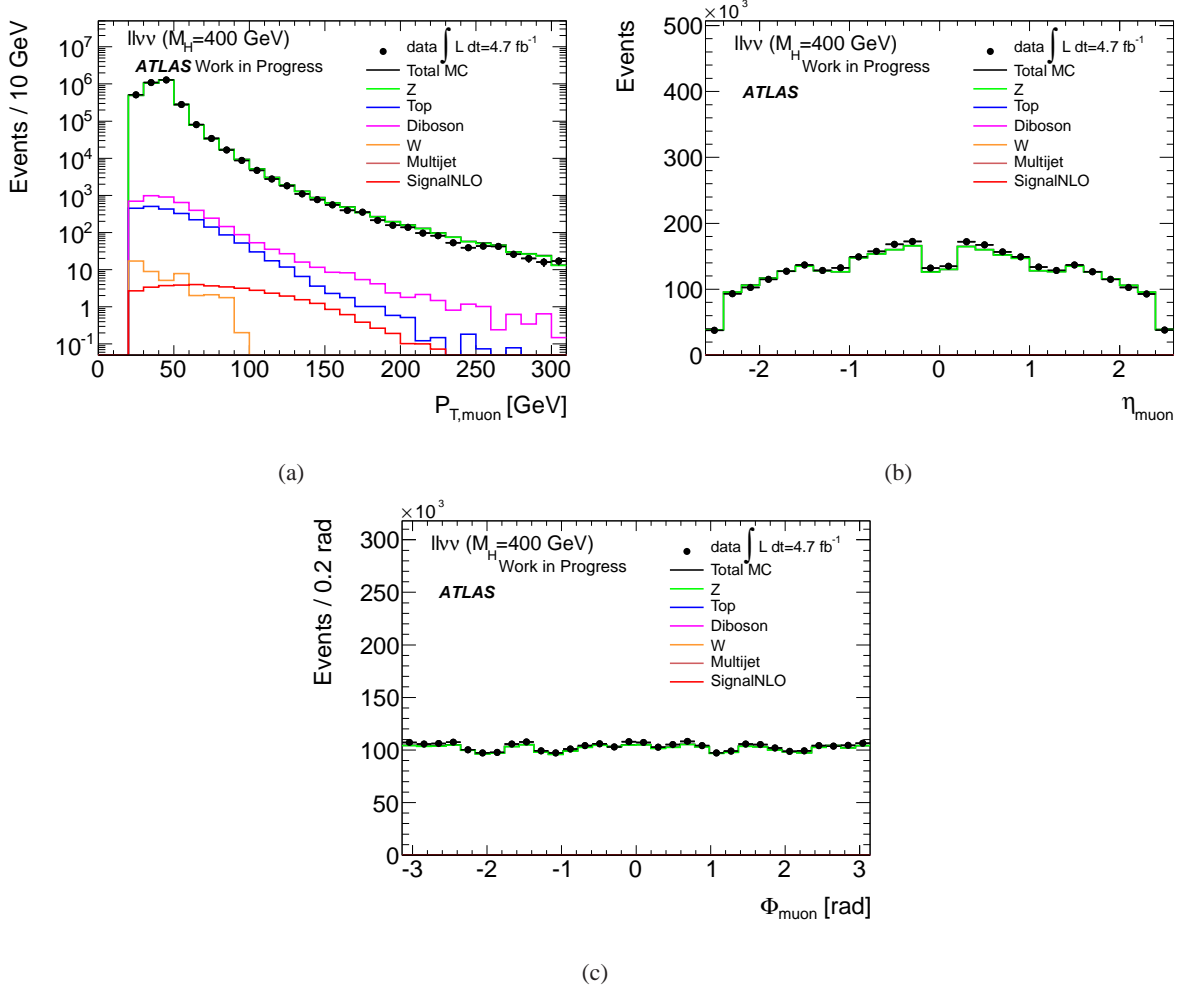


Figure 18: The p_T and η and ϕ distributions of the two muons forming the leptonic Z boson candidate after the Z mass selection.

the first layer of the ECAL is used to determine the substructure of the EM showers, which are used in particular to distinguish between electrons and charged pions and photons and neutral pions.

From the ID the discriminating variables are; track quality parameters, transition radiation information in the TRT and ID/calorimeter spatial and energy matching information. The cuts on the track quality parameters include; at least 9 precision hits in total from the pixel and SCT; at least 2 hits in the pixel layers, one of which must be in the b layer and a transverse impact parameter within 1mm of the primary vertex. The discriminating variable used in the TRT is the ratio of the number of high threshold hits to the total number of TRT hits. The final discriminating variables used are the alignment of the η and ϕ co-ordinates of the ID and calorimeter measurements and also the difference between momentum and energy as measured from the ID and calorimeter respectively (the electrons are highly relativistic

Identification	Combined STACO muons only
Kinematic cuts	$p_T^\mu > 20 \text{ GeV}$ $ \eta^\mu < 2.5$
Inner Detector	$N_{\text{hits}}^{\text{b-layer}} > 0$ (except where the muon passes an uninstrumented/dead area) $N_{\text{hits}}^{\text{pixel}} + N_{\text{dead}}^{\text{pixel}} > 1$ $N_{\text{hits}}^{\text{SCT}} + N_{\text{dead}}^{\text{SCT}} > 5$ $N_{\text{holes}}^{\text{pixel}} + N_{\text{holes}}^{\text{SCT}} < 3$ $ \eta < 1.9$: $N_{\text{tot}}^{\text{TRT}} > 5$ and $N_{\text{outliers}}^{\text{TRT}} < 0.9 \times N_{\text{tot}}^{\text{TRT}}$ $ \eta \geq 1.9$: If $N_{\text{tot}}^{\text{TRT}} > 5$, require $N_{\text{outliers}}^{\text{TRT}} < 0.9 \times N_{\text{tot}}^{\text{TRT}}$, where $N_{\text{tot}}^{\text{TRT}} = N_{\text{hits}}^{\text{TRT}} + N_{\text{outliers}}^{\text{TRT}}$.
Cosmic rejection	$ d_0 < 1 \text{ mm}$ $ z_0 < 10 \text{ mm}$
Jet Overlap Removal	$\Delta R_{\mu, \text{jet}} > 0.4$
Track isolation	$\sum_{\text{tracks}} p_T(\Delta R < 0.2)/p_T^\mu < 0.1$

Table 4: Summary of muon selection. N_{hits} (N_{holes}) represent the number of hits (missing hits) in a particular sub-detector of the inner tracker, while N_{dead} refers to the number of dead sensors crossed by the muon in a particular sub-detector.

and therefore the momenta and energy should be the same).

In general there are three particle identification menus (PIDs) used in ATLAS that define the values at which the above variables are cut. These are named loose, medium and tight. The definition of these menus changes depending on the year the analysis was performed, and from 2011 onwards three additional PID menus were used; loose++, medium++ and tight++. These are generally tighter than the initial PID menus and were changed to cope with the increase in calorimeter activity due to pile-up.

The loose++ menu uses only the hadronic leakage, lateral shower shape and lateral shower width. It has excellent acceptance but low background rejection. The medium++ menu applies all of the loose selection criteria and additionally uses the substructure information from the first layer of the ECAL and the tracking hits (except the b layer requirement). It increases the jet rejection by a factor of 4 with respect to the loose selection, but the identification efficiency is reduced by approximately 10%. A summary of the selection menus is given in table 5.

The electron energy scale, resolution and reconstruction efficiency are determined by a tag and probe method using electrons from $Z \rightarrow ee$, $W \rightarrow ev$ and $J/\Psi \rightarrow ee$ decays [44]. $Z \rightarrow ee$ decays are used for

Type	Description	name
Loose/loose++ selection variables		
Acceptance	$ \eta < 2.47$	
Hadronic Leakage	Ratio of the E_T of the first layer of the HCal with the E_T of the EM Cluster, used for $ \eta < 0.8$ and $ \eta > 1.37$	RHad1
	Ratio of the E_T of the HCal with the E_T of the EM Cluster, used for $ \eta < 0.8$ and $ \eta > 1.37$	RHad
Middle Layer of EM calorimeter	Ratio of energy in 3×7 cells with the energy in 7×7 cells centred at the electron cluster position	R_η
	Lateral shower width	ω_η
Medium/medium++ selection variables (includes loose/loose++)		
Strip Layer of EM calorimeter	Shower width	ω_{stot}
	Ratio of the energy difference between the 2 largest energy deposit and the sum of the two	E_{ratio}
Track quality	Number of hits in the pixel detector (≥ 1)	n_{pixel}
	Number of total hits in the pixel and SCT detectors (≥ 7)	n_{Si}
	Transverse impact parameter $ d_0 < 5$ mm	d_0
Track Cluster matching	$\Delta\eta$ between the cluster position in the strip layer and the extrapolated track ($ \Delta\eta $)	$\Delta\eta$

Table 5: Summary of the variables used to determine identity of electrons. Only loose and medium are given. [44]

high p_T electrons and $W \rightarrow e\nu$ and $J/\Psi \rightarrow ee$ are used to obtain efficiencies and smearing factors for electrons with lower momentum. A cross check is also performed by comparing the energy measured in the calorimeter to the momentum of the track, which is measured in the inner detector. The identification efficiencies are determined as a function of p_T , η and ϕ . These efficiencies are then applied by weighting the simulated events containing electrons. The p_T of simulated electrons are also smeared as a function of p_T , η and ϕ . The uncertainty of these measurements is propagated through to the analyses by shifting the event weights, scale and smearing factors up and down.

For the analyses presented in chapters 6 and 7 a track isolation requirement is applied to the electrons to reduce the number of jets faking electrons and to remove electrons that originate from jets. The sum of the p_T of all the tracks that lie within a cone of $\Delta R = 0.2$ of an electron is required to be less than 10%

of the p_T of the electron itself. The momentum of tracks that lie within $\Delta R = 0.01$ are not added to this sum to avoid including the p_T of the track associated to the electron.

The transverse momentum of an electron is determined using the energy from the cluster in the calorimeter and the η from the track. However if there are fewer than 3 track hits (both SCT and Pixel) the angle is also taken from the cluster in the calorimeter. The p_T , η and ϕ distributions of electrons consistent with having originated from a Z boson are shown in fig. 19.

In the 2012 dataset and the associated detector simulation, electron tracks are refitted using a Gaussian Sum Filter [45] to account for energy loss due to bremsstrahlung as the electron passes through the inner detector material.

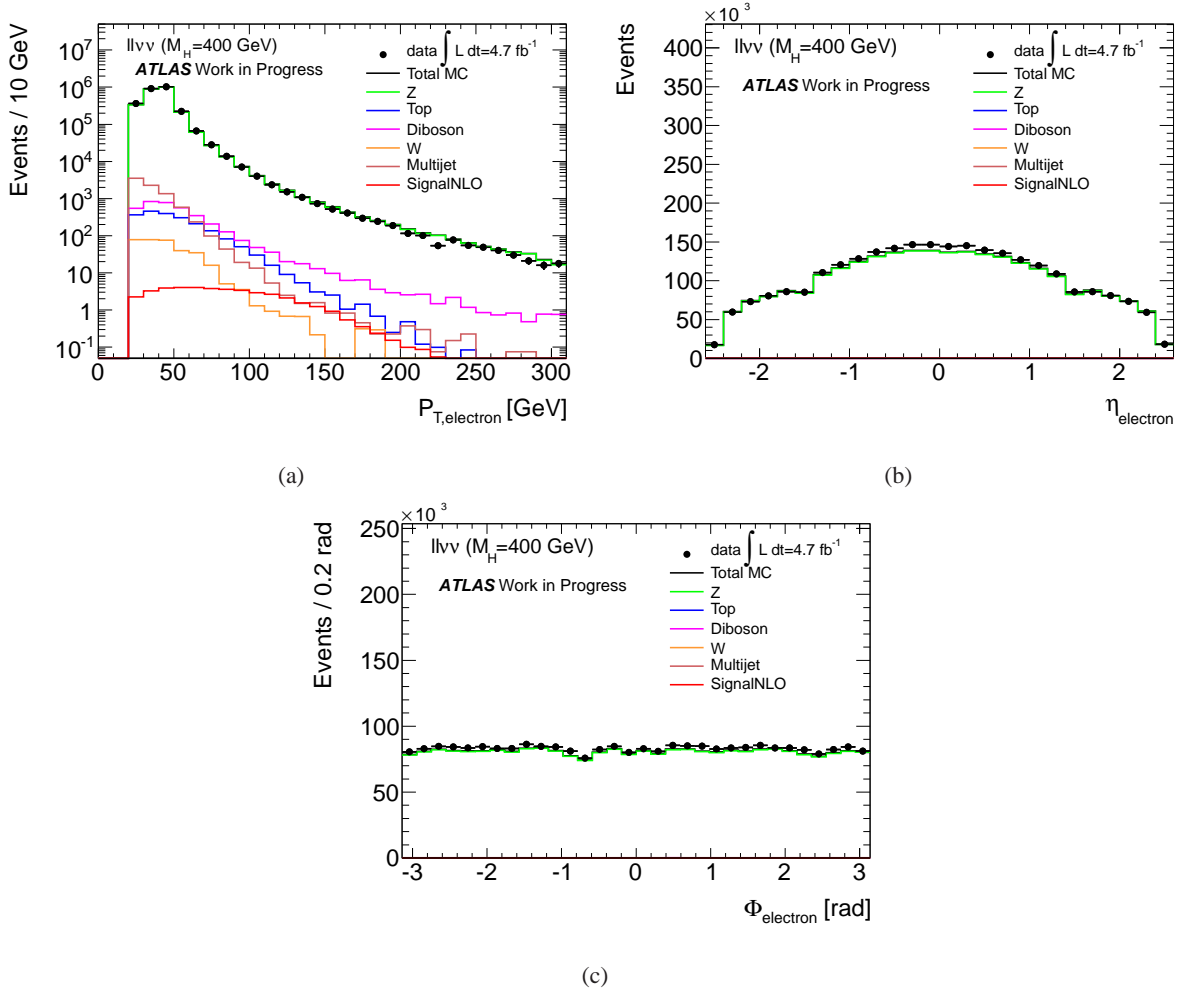


Figure 19: The p_T , η and ϕ distributions of the two electrons forming the leptonic Z candidate after the Z mass cut, described in chapter 6.

4.4 Jets

Jets are collimated bunches of stable hadrons which originate from gluons or quarks after they have fragmented and hadronised. Jets deposit their energy in both the EM and hadronic calorimeters. They are used in two ways for the analyses presented in chapters 6 and 7; for the accurate determination of the E_T^{miss} and to reduce the background using either a complete jet or a b-jet veto.

To measure the energy of a jet the energy deposits are first clustered together using a clustering algorithm and then these clusters are grouped together using a jet finding algorithm. In the analyses presented in chapters 6 and 7 the jets are reconstructed from topological clusters [46] using an anti- k_T algorithm [47] with a distance parameter $R = 0.4$. Topological clusters do not have a fixed size and are identified by combining neighbouring cells with significant energy deposits. The jet energy as measured from the calorimeters is corrected to account for dead material, particles not totally contained in the calorimeter, out of cone effects and clustering inefficiencies via a p_T and η dependent Jet Energy Scale (JES) determined from Monte Carlo Simulation [48]. The uncertainties applied on the energy of jets are obtained from data by considering the single particle response, whereby the objects that make up the jets are shifted by their corresponding uncertainties [49], and by results from a study in which a slice of the ATLAS detector was exposed to a beam of pions with p_T between 20 and 350 GeV [50]. The p_T , η and ϕ distributions for jets in events containing two leptons are shown in fig. 20.

A parameter known as the Jet Vertex Fraction (JVF) is used to remove jets that may have originated from other pp collisions occurring in the same bunch-crossing (in-time pile-up). The JVF is defined as the fraction of tracks that are associated to the jet that are consistent with having originated from the primary vertex. Tracks are taken to be associated to a jet if they lie within $\Delta R < 0.4$ of the jet axis.

4.4.1 b -Jets

ATLAS b -tagging algorithms are used to establish the likelihood of a jet to have contained a decay of a b -hadron, which is any hadron containing a b -quark. These algorithms take advantage of the fact that b -hadrons have a significant lifetime ($c\tau \approx 450 \mu\text{m}$). Jets containing such hadrons are primarily identified by reconstructing a secondary decay vertex from the tracks within the jet, or by combining the distance of closest approach to the primary vertex (impact parameter) of all tracks in the jet [51].

For the $H \rightarrow ZZ \rightarrow ll\nu\nu$ analysis the b -tagging algorithm used is MV1 [52]. It is based on a neural network that combines the output weights from various b -tagging algorithms as input. These algorithms identify b -jets using the tracks associated to the candidate jet to calculate both the impact parameter with respect to the primary vertex and the presence of displaced secondary vertices [52]. It gives each jet in

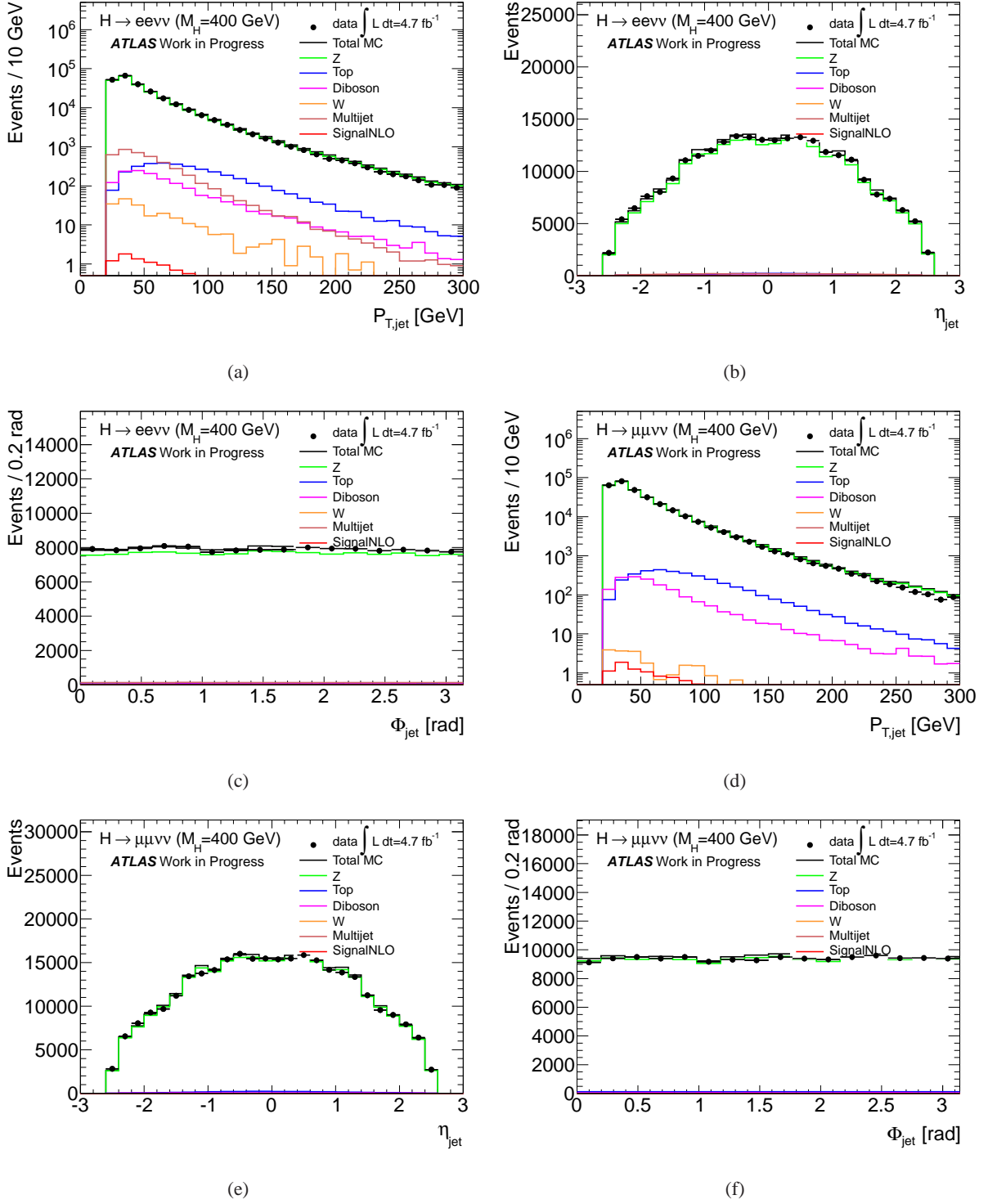


Figure 20: The p_T (a,d), η (b,e) and ϕ (c,f) distributions of the highest p_T jet in events with exactly two electrons or two muons (as indicated on the plots). Only jets with $p_T > 25$ GeV and $|\eta| < 2.5$ are included.

the event a b -weight that indicates the likelihood of it having originated from a b quark, which can then be cut on if it is above a certain threshold. The threshold chosen for the $H \rightarrow ZZ \rightarrow ll\nu\nu$ analysis corresponds to a b -tagging efficiency of 85% for true b -jets in $t\bar{t}$ events [53]. The c -tag efficiency, defined as the likelihood of identifying a jet containing a c -quark decay as a b -jet at this working point is 50%. The mistag efficiency, defined as the probability of mistakenly b -tagging a jet originating from a u, d, s -quark or a gluon, at this working point is approximately 1%, and is p_T dependent. The Monte Carlo b and c -tagging efficiencies and the light jet rejection are corrected to those observed in the data following the procedure described in [54], which uses the invariant mass of tracks associated to secondary decay vertices to distinguish between light and heavy jets, and cross checks this by studying the rate of events with a negative impact parameter, or that are measured to have a negative decay length, in $t\bar{t}$ events.

4.5 Overlap removal

For the analyses presented in chapters 5, 6 and 7 an overlap removal procedure is applied to ensure that no detector objects are counted twice. Firstly, if an electron is identified as having a track within $\Delta R < 0.2$ of the inner detector track of a candidate muon the electron is removed. It is highly likely that an electron will also be identified as a jet. Therefore jets are removed from the event if they lie within a cone of $\Delta R < 0.2$ of an electron.

As well as being used to avoid double counting of detector objects the overlap removal is also used to identify secondary leptons originating from heavy flavour jets which can then be removed. Muons are removed if they lie within a cone of $\Delta R < 0.4$ of a jet. Electrons are removed if they lie within $0.2 < \Delta R < 0.4$ of a jet. Note that this is applied after the initial overlap removal of jets which is why there is a lower bound.

4.6 Missing transverse energy

The missing transverse energy (E_T^{miss}) is reconstructed from energy deposits in the calorimeters and from muons reconstructed in the muon spectrometer. Tracks from the inner detector are also used to recover low energy particles with modest calorimeter deposits and to help identify muons in regions where there is incomplete MS coverage [55]. In order to apply the correct calibrations the calorimeter clusters are associated to physics objects in the following order; electrons, photons, hadronically decaying taus, jets and muons.

The definition of each object and the overlap removal are based on maximising the E_T^{miss} performance and are independent of those applied in the analysis. The configuration applied to reconstruct the E_T^{miss} is

known as MetRefFinal, and details of the precise definitions of all the objects can be found in [56].

After the calibrations have been applied a negative vectorial sum of the energy of cells associated to each object is calculated using

$$E_{x(y)}^{miss\ i} = \sum_{i=0}^N E_{x(y)}^{miss\ i} \quad (48)$$

where N is the total number of objects. The total missing transverse energy components are then calculated using

$$E_{x(y)}^{miss} \equiv E_{x(y)}^{miss,e} + E_{x(y)}^{miss,\gamma} + E_{x(y)}^{miss,\tau} + E_{x(y)}^{miss,jets} + E_{x(y)}^{miss,soft\ jets} + E_{x(y)}^{miss,calo\mu} + E_{x(y)}^{miss,CellOut} + E_{x(y)}^{miss,\mu} \quad (49)$$

where e is an electron, γ is a photon, $jets$ are high p_T jets, $soft\ jets$ are low p_T jets, $calo\mu$ is the energy deposited by muons in the calorimeter, $CellOut$ is the the energy from cells not associated with reconstructed objects, and μ is the component of the muon reconstructed in the MS. The objects are reconstructed in the pseudorapidity range $|\eta| < 4.9$, except for the μ term which uses tracks with $|\eta| < 2.7$.

The total E_T^{miss} and it's ϕ co-ordinate are then determined using equations 50.

$$\begin{aligned} E_T^{miss} &= \sqrt{(E_x^{miss})^2 + (E_y^{miss})^2} \\ \phi^{miss} &= \tan^{-1}(E_y^{miss} / E_x^{miss}) \end{aligned} \quad (50)$$

A value similar to E_T^{miss} is the missing transverse momentum of all ID tracks (P_T^{miss}) which is determined using only the information from the inner detector. It is calculated by performing a negative vectorial sum of the momenta of all tracks in the event that pass a set of cuts. The cuts ensure only good quality tracks are used and are applied on the transverse and longitudinal impact parameters, the momentum, the number of SCT and Pixel hits, η and ϕ . The overall value of the P_T^{miss} is not used in any of the analyses presented in this thesis, only the ϕ angle of the P_T^{miss} with respect to that of E_T^{miss} is used.

Chapter 5

Search for the SM Higgs boson in the $H \rightarrow ZZ \rightarrow llll$ channel

In this section a feasibility study of a search for a Standard Model Higgs Boson in the $H \rightarrow ZZ \rightarrow llll$ channel is described. The study was conducted in 2010. At this time only cosmic data had been recorded by the ATLAS detector as the LHC was offline, but it was shortly scheduled to start collisions at energies of $\sqrt{s} = 7$ TeV with a luminosity of 1 fb^{-1} expected to be recorded by the end of 2011.

A Standard Model Higgs search in this channel over a wide mass range was already well established [34]. The search presented here is a dedicated study focusing on the potential to look for a high mass Higgs using this channel. This study was based on the selection and background studies from the existing analysis. The analysis, combined with two further high mass Higgs boson search channels that are also briefly described in this chapter, was documented in an internal ATLAS note in 2010 [57].

Following this, a brief section describing a study on the recovery of electrons in the crack region of the electro-magnetic calorimeters using data taken at the end of 2010 is presented, and its impact on the Higgs searches containing a leptonically decaying Z boson is discussed.

5.1 The $H \rightarrow ZZ \rightarrow llll$ channel

The $H \rightarrow ZZ \rightarrow llll$ channel, where $l = e, \mu$, is one of the most important channels in the search for the SM Higgs boson. The four lepton final state ensures that there is good distinguishing power between the signal and background processes and the possibility for one of the Z bosons to be off-shell means that this channel is sensitive across a wide mass range; from $m_H = 110$ GeV up to masses of several hundred GeV.

The analysis presented in this section focuses on the high Higgs mass range, $m_H > 2m_Z$, where both Z bosons are likely to be on-shell. Although this mass region was disfavoured by electro-weak fits [7], it was important to perform a direct search. It was expected that with a limited amount of LHC data early limits could be set on the possibility of a high mass SM Higgs Boson.

The branching ratios for a Higgs boson decaying to various particles as a function of the Higgs mass are shown in fig. 21. From fig. 21 it can be seen that at low masses ($m_H < 180$ GeV) the contribution of $H \rightarrow ZZ$ to the total decay of the Higgs is modest. For the higher masses ($m_H > 2m_Z$) the dominant

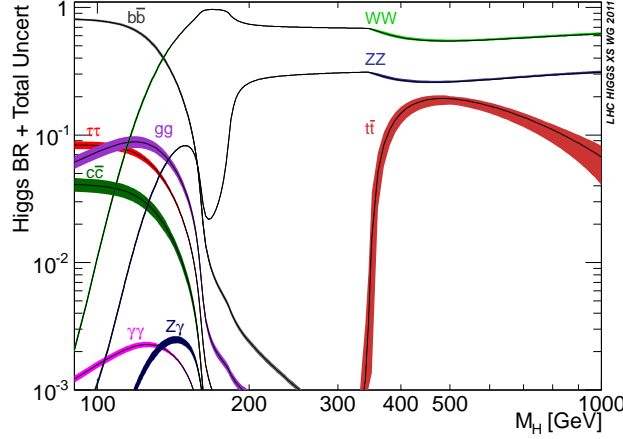


Figure 21: Branching fractions of the SM Higgs boson as a function of the Higgs mass [19].

decays are $H \rightarrow WW$ and $H \rightarrow ZZ$. The leptonic decay of the WW channel contains neutrinos, and so cannot be fully reconstructed. There is also a significant background to this final state from $t\bar{t}$ production. The $H \rightarrow ZZ \rightarrow llll$ channel on the other hand has a fully reconstructable final state, and the only significant background is expected to come from SM ZZ production.

The channel is limited however by the low branching ratio of a Z boson to decay to either two electrons, $(3.363 \pm 0.004)\%$, or two muons, $(3.366 \pm 0.007)\%$ [58]. Consequently, of all the $H \rightarrow ZZ$ events produced in the ATLAS detector only about 0.5% will decay to four leptons.

The search for the Higgs boson in this channel is performed by looking for a resonance in the distribution of the invariant mass of the four lepton system in three independent channels, $H \rightarrow ZZ \rightarrow eeee$, $H \rightarrow ZZ \rightarrow \mu\mu\mu\mu$ and $H \rightarrow ZZ \rightarrow \mu\mu ee$.

5.2 Signal samples

Simulated signal samples for $H \rightarrow ZZ \rightarrow llll$, where $l = e, \mu, \tau$ were generated using the PYTHIA 6.421 event generator. The simulation takes into account both the gluon-gluon and vector boson fusion production mechanisms for the Higgs boson, diagrams for which can be seen in fig. 3. The cross sections for $H \rightarrow ZZ$ are set to NNLO accuracy for the gluon-gluon fusion process and to NLO for the vector boson fusion production [59]. Samples were generated for all masses in the range $200 < m_H < 600$ GeV in increments of 20 GeV. The details of these samples are given in table 6.

m_H (GeV)	cross section (fb)	Events	Luminosity (fb ⁻¹)
200	15.235	49937	3278
220	13.830	49993	3615
240	12.091	49936	4155
260	10.510	49940	4752
280	9.326	49987	5360
300	8.444	49933	5913
320	7.855	49974	6362
340	7.696	49888	6531
360	7.639	49979	6494
380	6.918	49977	7224
400	5.964	49982	8381
420	5.059	49990	9882
440	4.264	49986	11724
460	3.586	49983	13937
480	3.015	49981	16576
500	2.535	49977	19711
520	2.133	49977	23386
540	1.797	49977	27818
560	1.512	49938	33036
580	1.280	49982	39041
600	1.085	49981	46047

Table 6: The $H \rightarrow ZZ \rightarrow llll$ ($l = e, \mu, \tau$) cross section as a function of m_H at $\sqrt{s} = 7$ TeV, the number of events generated and the corresponding integrated luminosity of the $H \rightarrow ZZ \rightarrow llll$ signal samples, generated using the PYTHIA MC generator. The cross sections are evaluated from theoretical calculations in [59].

5.3 Background samples

As this was a preliminary study aimed at establishing the sensitivity of the $H \rightarrow ZZ \rightarrow llll$ channel in the ATLAS experiment all backgrounds were taken from MC. It was anticipated that during data taking more sophisticated techniques for estimating these backgrounds would be developed. The dominant background for this channel is the irreducible SM $ZZ \rightarrow llll$ background, which has an identical final state to that of the signal. Other backgrounds considered for this analysis are those from $t\bar{t}$ and $Z + jets$.

Details of these backgrounds and the samples used to simulate them are described below.

5.3.1 ZZ background

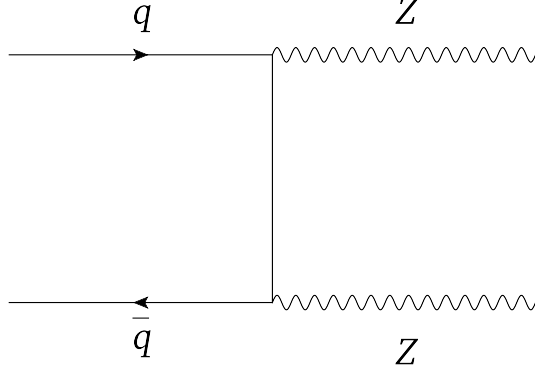


Figure 22: SM production of a Z boson pair.

The tree level Feynman diagram for the SM ZZ production is shown in fig. 22. The SM ZZ background has an identical final state to the signal, and thus can not easily be estimated directly from data. Therefore in this study the ZZ normalisation and shape were taken from MC.

Two samples were available to simulate this background, generated by MC@NLO [60] interfaced with JIMMY 4.31 [61] or generated with PYTHIA 6.421 [62]. The MC@NLO sample only contains on-shell Z bosons, but includes diagrams to NLO. The PYTHIA sample contains off-shell Z bosons but only includes LO diagrams. Although this analysis searches in the region $m_H > 200$ GeV, where the Z bosons are likely to be on-shell, a small fraction of events from off-shell Z bosons can still make it through the selection, particularly for the low mass region ($m_H < 300$ GeV). In order to measure the effect of off-shell Z bosons on this analysis a direct comparison was made between the two samples.

The LO PYTHIA sample is scaled to the overall NLO cross section by a k-factor, which is simply a ratio of the NLO and LO cross sections. The k-factor used for the PYTHIA sample is 1.25 [63].

Fig. 23 shows the invariant mass of the primary and secondary lepton pair (that are defined in section 5.4.3) for both SM ZZ MC samples. The width of the primary lepton pair is clearly wider in the PYTHIA sample which is due to the contribution from off-shell Z bosons. However, the difference between the two samples is much less pronounced in the final four lepton mass distribution, as can be seen in fig. 24. In this distribution good agreement is observed between the two samples. The effect of including off-shell Z bosons was estimated to have a less than 10% effect on the 4 lepton invariant mass distributions. Given that the latter distributions are used to calculate the expected limits the MC@NLO

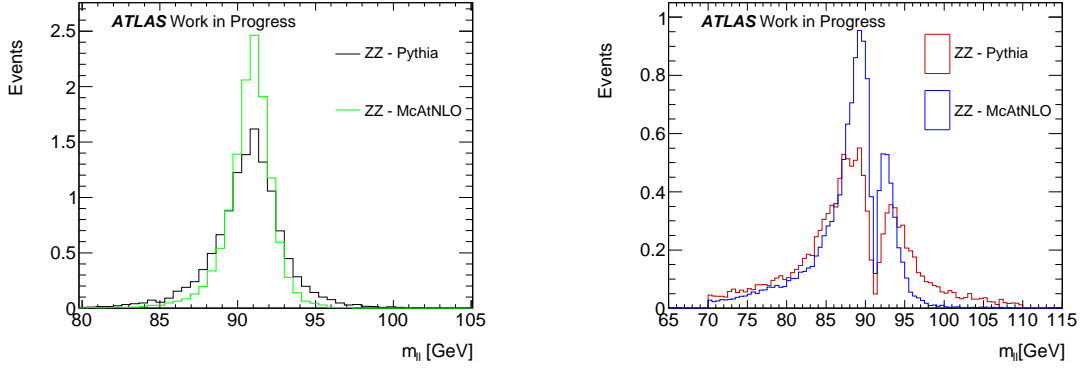


Figure 23: Comparison of the invariant mass distribution of the primary (left) and secondary (right) lepton pair in ZZ events simulated with MC@NLO or PYTHIA + k-factors, after the full selection.

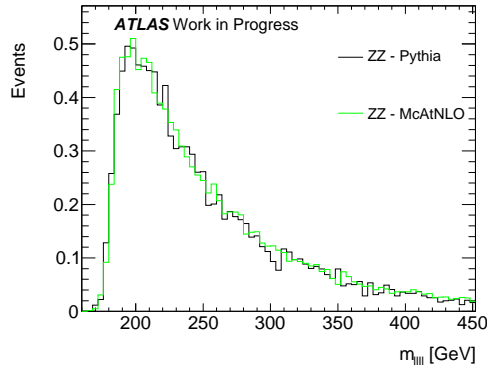


Figure 24: Comparison of the 4 lepton invariant mass distribution in ZZ events simulated with MC@NLO or PYTHIA + k-factors, after the full selection (high mass).

sample was used to estimate the SM ZZ background for the simple reason that it has higher statistics than the PYTHIA sample. A 10% systematic uncertainty was included for this effect and the PYTHIA sample was used to give an estimate of the shape uncertainty for the final distributions, as described in section 5.5.

The cross sections used for the MC@NLO sample is obtained from [64], but an additional factor of 16%, suggested in [63], is applied to account for missing NNLO gluon induced quark box diagrams [65]. This factor is applied to both the MC@NLO and PYTHIA sample. Details of the two samples are given in table 7.

process	generator	cross section (fb)	events	luminosity (fb ⁻¹)
$ZZ \rightarrow llll$	MC@NLO	26.181	69908	2670
$ZZ \rightarrow llll$	PYTHIA	75.03	59938	1332

Table 7: Cross sections at $\sqrt{s} = 7$ TeV, number of events generated and the corresponding integrated luminosity for the $ZZ \rightarrow llll$ sample generated using the MC@NLO and PYTHIA MC programs. The cross sections given are at NLO accuracy.

5.3.2 $Z + jets$ background

The $Z + jets$ background can form a background when the Z boson undergoes a leptonic decay and there are two additional reconstructed leptons; either coming from jets that are misidentified as electrons or from semi-leptonic decays of heavy flavour hadrons. For the high Higgs masses considered in this analysis the majority of leptons will have a comparatively large p_T . Such leptons are unlikely to be faked by jets. On top of this the isolation requirements imposed on the leptons ensure that very few leptons originate from jets. As a result, this background is very small, and was estimated entirely using MC.

The sample used to simulate this background was generated using ALPGEN [66], which is a NLO generator. The program generates separate samples for Z production with different numbers of final state partons p , where p runs from 0 – 3. A mixture of inclusive Z samples and specific $Zbb(Z \rightarrow ll)$ samples was used. The overlap between the samples is accounted for in a procedure described in [67]. Details of the individual samples are given in table 8.

5.3.3 $t\bar{t}$ background

Although it is unlikely that four isolated leptons are reconstructed in $t\bar{t}$ events the abundance of $t\bar{t}$ events in a hadron collider may allow a small fraction of such events to pass all cuts. This contribution is expected to be extremely small, particularly for searches at high Higgs masses. This background was estimated entirely using MC.

The sample used to simulate this background was generated using MC@NLO interfaced to JIMMY and includes diagrams to NLO. It is filtered at generator level so that the events contain at least one lepton (e, μ or τ) originating from a leptonic W decay. Details of this sample are given in table 9.

process	cross section (fb)	events	luminosity (fb ⁻¹)
$Z + 0p, Z \rightarrow ee$	659583	304216	0.461
$Z + 1p, Z \rightarrow ee$	13462	63440	0.479
$Z + 2p, Z \rightarrow ee$	41356	19497	0.471
$Z + 3p, Z \rightarrow ee$	10790	5499	0.510
$Z + 0p, Z \rightarrow \mu\mu$	659583	303947	0.461
$Z + 1p, Z \rightarrow \mu\mu$	13462	62996	0.476
$Z + 2p, Z \rightarrow \mu\mu$	41356	18993	0.459
$Z + 3p, Z \rightarrow \mu\mu$	10790	5497	0.509
$Zb\bar{b} + 0p, Z \rightarrow ee$	6519	149925	23.0
$Zb\bar{b} + 1p, Z \rightarrow ee$	2490	99973	40.1
$Zb\bar{b} + 2p, Z \rightarrow ee$	876	39989	45.6
$Zb\bar{b} + 3p, Z \rightarrow ee$	391	9949	25.4
$Zb\bar{b} + 0p, Z \rightarrow \mu\mu$	6519	149968	23.0
$Zb\bar{b} + 1p, Z \rightarrow \mu\mu$	2490	99975	40.1
$Zb\bar{b} + 2p, Z \rightarrow \mu\mu$	876	39988	45.6
$Zb\bar{b} + 3p, Z \rightarrow \mu\mu$	391	9997	25.6

Table 8: Cross sections at $\sqrt{s} = 7$ TeV, number of events generated and the corresponding integrated luminosity of the $Z + \text{jets}$ MC samples generated using the ALPGEN MC program. p refers to the number of partons that were generated at the matrix element level.

process	cross section (fb)	filter	filtered cross section	events	weighted events	luminosity (fb ⁻¹)
$t\bar{t}$	156879	0.5562	87256	999387	773167	8.86

Table 9: Cross sections at $\sqrt{s} = 7$ TeV, number of events generated and the corresponding integrated luminosity for the $t\bar{t}$ sample generated using the MC@NLO MC program. The cross section is NLO accuracy taken from [64], convoluted with branching fractions taken from the Particle Data Book [58].

5.4 Event selection

The following event selection was developed in the ATLAS Higgs group to select possible $H \rightarrow ZZ \rightarrow llll$ candidate events. It is split up into three parts; in the preselection the relevant kinematic and quality cuts on the leptons are applied; then the best two candidates are selected from all possible lepton pairs. Finally the best ZZ candidates are selected and a set of m_H dependent cuts are applied, as well as cuts

specific to the flavour of the leptons in the final state.

5.4.1 Preselection

Muons In the central region ($|\eta| < 2.5$) muons are required to be either combined or tagged (as defined in section 4.2), whereas for $2.5 < |\eta| < 2.7$ stand alone muons are also allowed.

Electrons Electrons must lie within the central region of the detector ($|\eta| < 2.47$) and are required to satisfy the medium quality requirements if they have $p_T < 20$ GeV, otherwise they only need to satisfy the loose quality requirements (as defined in section 4.3).

Leptons It is required that there are at least four reconstructed leptons in the event, two of which must have $p_T > 20$ GeV and a further two with $p_T > 7$ GeV.

5.4.2 Z candidate selection

- The leptons that make a Z candidate must be the same flavour and have opposite charge.
- The angular distance between the two leptons is required to satisfy $\Delta R > 0.1$.
- In order to reduce the contribution from the $Z + jets$ and $t\bar{t}$ backgrounds the leptons are required to be isolated by demanding that the sum of the transverse energy, E_T , of all calorimeter clusters that lie within a range $\Delta R < 0.3$ around the chosen lepton, $\Sigma E_T^{cone}(\Delta R < 0.3)$, normalised by the lepton p_T , be less than 0.5.
- A loose dilepton mass cut is then applied requiring that $70 < m_{ll} < 110$ GeV for at least one Z boson candidate per event.

5.4.3 ZZ candidate selection

From all possible lepton pairs constructed the leading lepton pair is defined to be the one with its invariant mass closest to the Z boson mass, taken to be 91.187 GeV [58]. The remaining lepton pair with the highest invariant mass is defined to be the secondary pair. Further cuts are then applied to the event depending on the invariant mass of the four lepton system:

- For $m_{llll} \geq 300$ GeV since both Z bosons will be on-shell a tight dilepton mass cut is applied, requiring that the invariant mass of both the primary and secondary lepton pair lies within a window

of ± 12 GeV around the Z mass. For $m_{llll} < 300$ GeV the requirement on the secondary pair is loosened to $m_{ll} > 60$ GeV to allow for contributions from off-shell Z bosons.

- A tighter isolation cut is applied where the leptons that make up the leading and secondary pairs are required to satisfy the condition $\Sigma E_T^{cone}(\Delta R < 0.3)/p_T < 0.33$ for electrons and $\Sigma E_T^{cone}(\Delta R < 0.3)/p_T < 0.44$ for muons.

The full selection is applied to both the signal and background samples.

5.5 Systematic uncertainties

The following is a list of the systematic uncertainties applied in this analysis.

Luminosity An uncertainty of 10% was applied to all samples. This uncertainty was assumed to be correlated across all samples.

Signal cross section The uncertainty on the signal cross section due to the choice of the renormalisation and factorisation scales and the chosen PDF parameterisation was taken from [59]. The uncertainty on the overall normalisation varies between 7.8% and 8.7% over all of the masses considered in this analysis, so a conservative uncertainty of 10% was applied to all signal samples.

Background cross section For the irreducible ZZ background a systematic error based on a 5% combined scale and PDF uncertainty on the NLO cross section was convoluted with a further 10% error corresponding to the maximum difference seen in the comparison between the k-factor scaled PYTHIA and MC@NLO MC as described in section 5.3.1. This lead to an overall scale uncertainty of 11% for the diboson background in this channel. In addition to this a shape uncertainty on the final distribution was applied. For this the PYTHIA ZZ sample was scaled so that it contained the same number of events as the nominal MC@NLO sample. This additional histogram was used internally within the limit setting code as described in section 5.7

For the relatively small $Z + jets$ background a conservative 10% uncertainty was applied on the normalisation, and similarly a 20% normalisation uncertainty was used for the $t\bar{t}$ background, which was estimated from MC.

Electrons There are systematic uncertainties associated with the energy scale, resolution and efficiency of each electron. In order to implement the energy scale and resolution uncertainties a separate set of

final distributions were produced for each, and then fed into the limit setting machinery as described in section 5.7.

To account for the uncertainty on the electron energy scale the energy of each electron was varied up and down by 1% [34]. For the resolution uncertainty it was assumed that for each electron the resolution was known to within 10%, this uncertainty was implemented by applying an additional smearing to the energy of each electron by an appropriate factor inversely proportional to \sqrt{E} . Finally a 1% uncertainty was assumed on the identification efficiency for each electron and this was implemented by simply scaling the final distributions up and down by 2% for the $ee\mu\mu$ channel and 4% for the $eeee$ channel.

Muons Similarly to the electrons there are uncertainties on the momentum scaling, the resolution and identification efficiency for the muons. Again the uncertainties in the momentum scaling and resolution were accounted for by shifting the central values and rerunning the selection, producing a separate set of final distributions.

An uncertainty on the muon momentum scale was applied by varying the corresponding momentum shift up and down by 0.3% [34]. It was assumed that the resolution of each muon was known to within 4%, therefore assuming an average resolution 5% for each muon, this uncertainty was implemented by applying a 1.4% additional smearing on the muon momenta. For the muon identification efficiency an uncertainty of 0.3% was assumed for each muon, which corresponds to an overall scaling to the final distributions of 0.6% for the $ee\mu\mu$ channel and 1.2% for the $\mu\mu\mu\mu$ channel.

5.6 Results

The distributions of the invariant mass of the $llll$ system after all cuts have been applied are shown in fig. 25 for $m_H = 200, 300, 400, 500, 600$ GeV. As can be seen from these distributions the $t\bar{t}$ and the $Z + jets$ backgrounds have been almost completely removed by the selection and the only background that contributes to the final state is the irreducible SM ZZ production. The shape of the signal across the entire mass range is approximately Gaussian. As the Higgs mass increases the peaks of the signal broaden and, due to the decrease in the cross section at higher masses, there is a reduction in the final number of events. The total number of events, after all cuts, for each of the Higgs mass samples as well as the backgrounds are given in table 10.

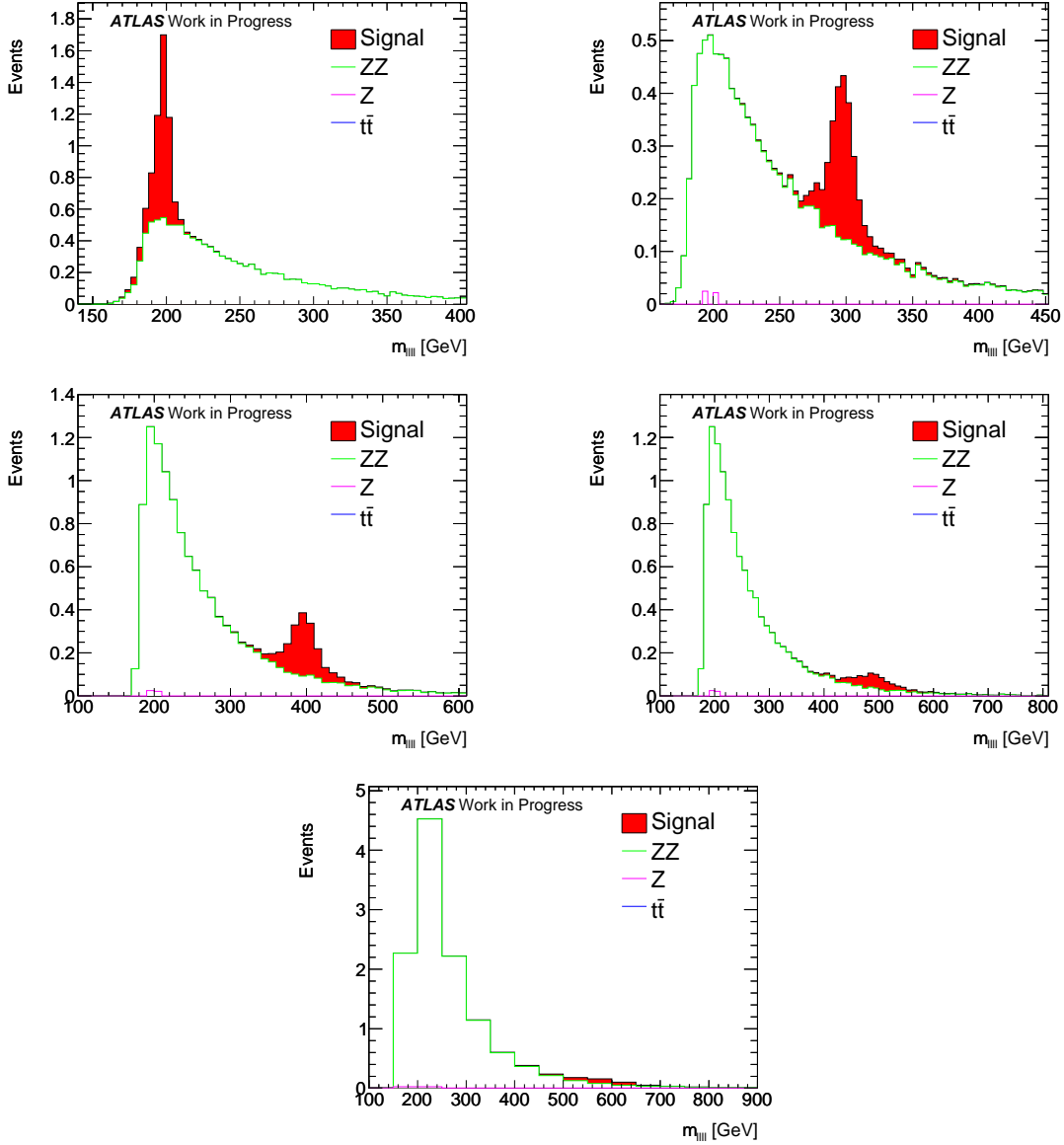


Figure 25: The invariant mass of the $llll$ system for 1 fb^{-1} at $\sqrt{s} = 7 \text{ TeV}$ for the Higgs masses $m_H = 200, 300, 400, 500$ and 600 GeV .

5.7 Expected exclusion limits

The sensitivity of the search for a SM Higgs boson in the $H \rightarrow ZZ \rightarrow llll$ channel is expressed in terms of CL_s [68]. This quantity is defined as $CL_s = CL_{s+b}/CL_b$, where CL_{s+b} is the probability that a composite distribution of signal and background will fluctuate to the observed number of data events or lower and CL_b is the probability that a background only distribution will fluctuate to the observed number of data events or higher. Low values of CL_s indicate that a background only hypothesis is more likely than a

Higgs mass (GeV)	Low mass cuts	High mass cuts
$m_H = 200$	3.36	–
$m_H = 220$	3.20	–
$m_H = 240$	2.85	–
$m_H = 260$	2.51	–
$m_H = 280$	2.30	–
$m_H = 300$	–	1.89
$m_H = 320$	–	1.77
$m_H = 340$	–	1.77
$m_H = 360$	–	1.83
$m_H = 380$	–	1.65
$m_H = 400$	–	1.44
$m_H = 420$	–	1.23
$m_H = 440$	–	1.03
$m_H = 460$	–	0.87
$m_H = 480$	–	0.73
$m_H = 500$	–	0.62
$m_H = 520$	–	0.52
$m_H = 540$	–	0.44
$m_H = 560$	–	0.37
$m_H = 580$	–	0.32
$m_H = 600$	–	0.27
Sample	Low mass cuts	High mass cuts
ZZ	12.45	12.45
Z	0.05	0.05
$t\bar{t}$	0.00	0.00

Table 10: The expected number of signal and background events for 1 fb^{-1} at $\sqrt{s} = 7 \text{ TeV}$ remaining in the $H \rightarrow ZZ \rightarrow llll$ search after the full selection. The two columns refer to the different cuts applied for low and high mass Higgs samples. The dash (–) indicates that these cuts were not applied for a particular Higgs mass.

background and signal hypothesis, and similarly a high value of CL_s would indicate a possible signal.

The limits are obtained using the `mclimit` [69] program used at the Tevatron in the search for the SM Higgs boson and the discovery of the top quark. The program is based on the CL_s method and allows multiple channels to be combined while taking into account both normalisation and shape uncertainties on signal and backgrounds.

In the absence of data one can estimate the expected exclusion sensitivity of a channel for a given luminosity by using pseudo-data distributions that are sampled from the background only prediction. Within the limit setting program this pseudo-data is treated in the same way as if it were genuine data.

A frequentist approach is used to calculate CL_b and CL_{s+b} , whereby many pseudo-experiments are generated. Each pseudo-experiment is comprised of a pseudo-data, a background only and a signal + background ($s + b$) distribution. The final output of each pseudo-experiment is the likelihood ratio, which is simply a ratio of the Poisson probabilities of the data given a signal plus background and given a background only hypothesis, as shown in equation 51.

$$X = \prod_{i=0}^{i=N_{bins}} \frac{e^{-(s_i+b_i)}(s_i + b_i)^{d_i}}{e^{-b_i}b_i^{d_i}}, \quad (51)$$

where X is the likelihood ratio, s_i , b_i and d_i are the content of the i^{th} bin of the signal, background and data distributions and N_{bins} is the number of bins in the final distribution.

The systematic variations are applied to both the $s + b$ and the background only distributions as is described in section 5.7.1. The pseudo-data distributions are sampled from the nominal background prediction, and only include the statistical fluctuations. Internally in the limit setting software a χ^2 comparison is performed between the pseudo-data distribution and the distributions of both the signal plus background and the background only hypotheses. The exact form of the χ^2 distribution used for the fits can be found in [70]. By generating many pseudo-experiments one can see how often, given the constraints of the analysis, one can exclude or accept either the background only or $s + b$ hypothesis.

5.7.1 The treatment of systematic uncertainties

Uncertainties in the prediction of the background only model and the signal plus background model allow the models to be more compatible with any observed data [71]. For example, if the systematic uncertainties are small, it is less likely that the pseudo-experiment background only distributions will yield a signal-like distribution, and therefore a stronger exclusion limit (higher value of $1 - CL_s$) is obtained. Conversely, larger systematic errors make it more likely for a background only experiment to produce signal like distributions, and so weaker exclusion limits will be obtained.

Systematic uncertainties effect both the normalisation and the shape of the final distribution. The manner in which each systematic is treated in this analysis is described in table 11. The alternative shape-shifted histograms represent $\pm 1\sigma$ variations corresponding to a given systematic uncertainty with respect to the nominal histograms.

Normalisation uncertainties In the case of a normalisation uncertainty the following formula is applied:

$$r_i^{varied} = r_i^{nominal} \prod_k (1 + s_k f_k), \quad (52)$$

where i is an index running over the bins, r_i is the content of the i^{th} bin, k is an index running over the systematic uncertainties, f_k is the fractional uncertainty of the k^{th} uncertainty and s_k is a Gaussian centred on 0 with unit width, and is often referred to as a nuisance parameter. Pseudo experiments are generated by applying random Gaussian variations to the nuisance parameters. A positive and negative shift in the normalisation uncertainties are both considered and in this analysis they are assumed to be symmetric. The shifts are restricted to never allow negative bin contents [71].

Shape uncertainties Uncertainties in the shape can also be accounted for by applying equation 52. In this case f_k would vary with the bin index i , and is taken from the fractional difference between the nominal and the varied distribution in each bin. Only one value of s_k is used. To allow for the multiple sources of shape uncertainty on the final distribution the nominal distribution is modified using the first systematic uncertainty, and then the result of this is used as the starting point for the next modification. This method is repeated until all the systematic uncertainties have been accounted for.

Correlation of uncertainties Systematic variations defined for different samples, or even channels, can be treated as correlated or uncorrelated.

5.7.2 Presentation of the limits

The expected sensitivity of the presented search is expressed in terms of the $1 - CL_s$ value, this gives a direct indication of the confidence level to which one can rule out a signal. For example, if $1 - CL_s > 0.95$ one can rule out the signal hypothesis at a 95% confidence level. Fig. 26 shows $1 - CL_s$ as a function of m_H for the $H \rightarrow ZZ \rightarrow eeee$, $H \rightarrow ZZ \rightarrow \mu\mu ee$ and $H \rightarrow ZZ \rightarrow \mu\mu\mu\mu$ channels separately, as well as the combination.

The effect of the systematic uncertainties on the final expected limits can be seen in fig. 27, which shows the impact of either doubling or removing the systematic uncertainties. As would be expected

systematic	signal	ZZ	Z + jets	$t\bar{t}$	implementation
electron scale up/down	yes	yes	yes	yes	alternate histogram
electron smearing	yes	yes	yes	yes	alternate histogram
muon scale up/down	yes	yes	yes	yes	alternate histogram
muon smearing	yes	yes	yes	yes	alternate histogram
electron efficiency up/down	yes	yes	no	yes	normalisation factor
muon efficiency up/down	yes	yes	no	yes	normalisation factor
MC estimated normalisation error	yes	yes	yes	yes	normalisation factor
luminosity	yes	yes	yes	yes	normalisation factor
ZZ shape	no	yes	no	no	alternate histogram

Table 11: Systematic variations applied and $t\bar{t}$ implemented correlations in the MCLIMIT program for the confidence level fits.

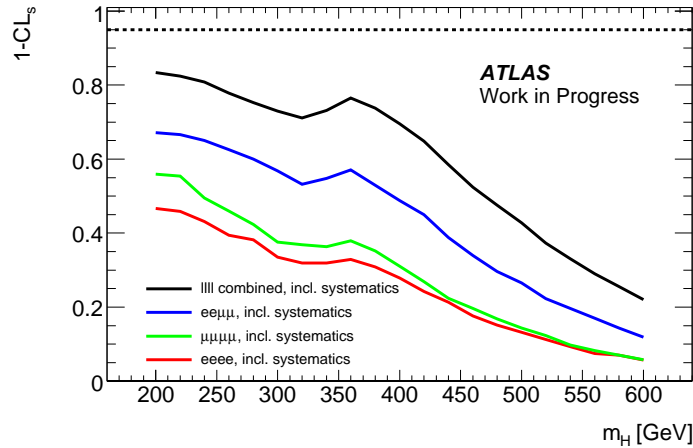


Figure 26: Expected $(1 - CL_s)$ values obtained for the search in the $H \rightarrow ZZ \rightarrow eeee$, $H \rightarrow ZZ \rightarrow \mu\mu ee$ and the $H \rightarrow ZZ \rightarrow \mu\mu\mu\mu$ channels as well as for the combined $H \rightarrow ZZ \rightarrow llll$ search. The limits correspond to 1 fb^{-1} of data at $\sqrt{s} = 7 \text{ TeV}$.

the strongest expected limits are obtained when no systematic variations are applied. The impact of applying the nominal systematics is to lower the expected exclusion limit across the entire mass range. At the higher masses, where there are fewer events expected, the statistical uncertainty is dominant. In this region the reduction in sensitivity due to the systematics is smaller. Overall however the small variations in the expected limits when removing or doubling the systematics suggests that this analysis

is robust against variations in the applied systematics.

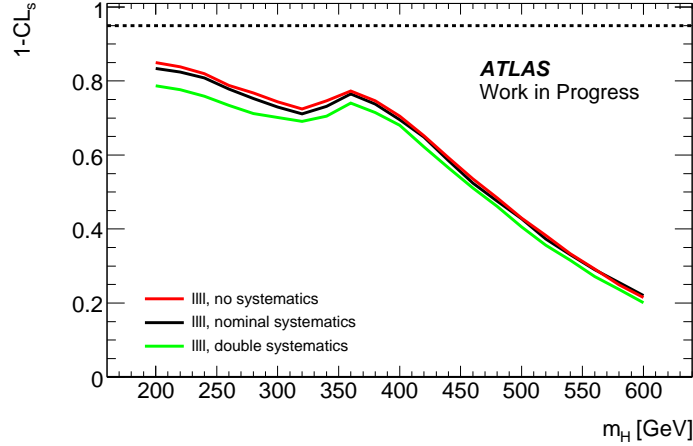


Figure 27: Expected $(1 - CL_s)$ values obtained for the $H \rightarrow ZZ \rightarrow llll$ channel, with no systematics, the nominal systematics or twice the nominal systematics applied. The expected limits correspond to 1 fb^{-1} of data at $\sqrt{s} = 7 \text{ TeV}$.

Given that the Higgs cross section at all possible masses is predicted by the SM one can plot the expected limits in a way that is intrinsically linked to the SM predictions, as shown in fig. 28. This figure shows the expected 95% CL upper limit on the SM production cross section multiplied by the branching ratio, expressed as multiples of the expected SM rate, as a function of the Higgs mass.

For a given Higgs mass m_H , a value of 1 on the y axis corresponds to a 95% confidence level exclusion of the Higgs with mass m_H with a cross section as predicted by the SM. This is indicated by the dashed horizontal line. A value of 2 on this axis means one could exclude a SM-like Higgs which has a cross section twice that predicted by the SM at a confidence level of 95%.

The green and yellow bands indicate the sensitivity of the expected limits to statistical variations, showing the limits for $\pm 1\sigma$ and $\pm 2\sigma$ fluctuations away from the expected background only distribution.

5.8 Conclusions

The analysis presented above demonstrates the sensitivity of the ATLAS detector to a high mass ($m_H > 200 \text{ GeV}$) Higgs decaying via the $H \rightarrow ZZ \rightarrow llll$ channel with 1 fb^{-1} of data at $\sqrt{s} = 7 \text{ TeV}$. It is based on MC predictions for both signal and background. The CL_s method is used to determine expected exclusion limits as a function of Higgs mass where both systematic and statistical uncertainties are taken into account. The effect of the systematics on the final expected limits was also investigated, and it was found that doubling the uncertainties leads to a maximum reduction in the expected $1 - CL_s$

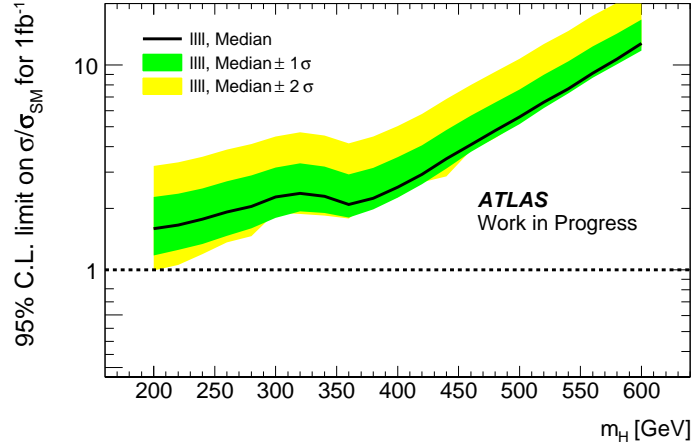


Figure 28: Expected limits for the $H \rightarrow ZZ \rightarrow llll$ channel, expressed as the number of times the SM Higgs cross section that would be excluded at 95% confidence level. The green and yellow bands indicate the expected sensitivity with $\pm 1\sigma$ and $\pm 2\sigma$ statistical fluctuations respectively. The expected limits correspond to 1 fb^{-1} of data at $\sqrt{s} = 7 \text{ TeV}$.

values of approximately 3%. The final results indicate that this channel is most sensitive at the mass $m_H = 200 \text{ GeV}$, and that at this mass a Higgs with a cross section 1.6 times higher than that predicted by the SM could be excluded with 1 fb^{-1} using this channel alone.

5.9 Studies on the 2010 data

Shortly after the analysis presented above concluded, the LHC started collisions at energies of $\sqrt{s} = 7 \text{ TeV}$, and by the end of 2010 44 pb^{-1} of data had been recorded. Although this dataset was too small to exclude a SM Higgs boson at any mass the first $\sigma \times BR(H \rightarrow ZZ)$ limits were set using this dataset.

The studies presented below helped contribute towards the event selection for the ATLAS $H \rightarrow ZZ \rightarrow llll$ search using the 2010 dataset [40], as well as the first results of the $H \rightarrow ZZ \rightarrow llqq$ and $H \rightarrow ZZ \rightarrow ll\nu\nu$ analyses [1].

5.10 Electrons in the crack region

To ensure that electrons can be measured in as wide an η range as possible there are both barrel and end cap calorimeters in the ATLAS detector, the layout of which is described in section 3.6. The region where the barrel and end cap calorimeters meet is called the ‘crack region’, and is located at $1.37 < |\eta| < 1.52$. The reconstruction of electrons in this region is more complex than elsewhere in the calorimeter. In the 2010 $H \rightarrow ZZ \rightarrow llll$ paper [40] a veto is applied on any electrons that lie within this range.

Approximately 4.6% of electrons lie within this η range. This can have a significant effect on the selection efficiency of the $H \rightarrow ZZ \rightarrow llll$ channel for final states that contain two or more electrons. For example in the $H \rightarrow ZZ \rightarrow eeee$ channel vetoing electrons in the crack region reduces the overall selection efficiency by 17%, and there is a smaller but still significant effect on the $H \rightarrow ZZ \rightarrow \mu\mu ee$ channel. Therefore any recovery of events with electrons in the crack region would significantly improve the sensitivity of this channel, as well as improving the sensitivity of other Higgs search channels which contain a leptonic Z decay, namely $H \rightarrow ZZ \rightarrow llbb$ and $H \rightarrow ZZ \rightarrow ll\nu\nu$.

A study was conducted using the 2010 dataset to investigate the prospects of recovering electrons from the crack region. This was done by looking at the dilepton invariant mass distributions in events with either one or two electrons in the crack region and comparing these with the same distributions for events with no electrons in the crack. A comparison of these distributions in data and MC was performed to ensure that there is a good description of the degradation of the invariant mass resolution for electrons in the crack, as well as of the selection efficiencies in this region.

The event selection applied for this study largely follows that outlined in section 5.4.2 with some improvements:

Trigger The triggers used correspond to the lowest p_T unprescaled single electron triggers, which due to variations in the running conditions changed throughout the 2010 data taking. For the early data a trigger was used which required an electron of $p_T \geq 14$ GeV as measured by the level 1 trigger. For later data an event filter trigger was used that required an electron of $p_T \geq 15$ GeV and satisfying the medium selection criteria. The efficiency of these triggers is simulated in MC and verified in data using a tag and probe method as described in section 4.3 and [44].

Primary vertex In order to reduce the effects of pileup it is required that the electrons must have a track within 10 mm of the primary vertex. The primary vertex is defined to be the vertex in the event closest to the extrapolated lepton vertex with at least three tracks associated to it.

Track isolation A track isolation criterion is applied which requires that the ratio of the sum of the momenta of all tracks within $\Delta R < 0.3$ of the electron relative to the momentum of the electron itself is less than 0.2.

Fig. 29 shows the invariant mass distributions for di-electron events with and without an electron in the crack region. The MC has been normalised so that there are the same number of events in the invariant mass distribution of electrons not from the crack with $70 < m_{ee} < 110$ GeV as in data for fig. 29 (a).

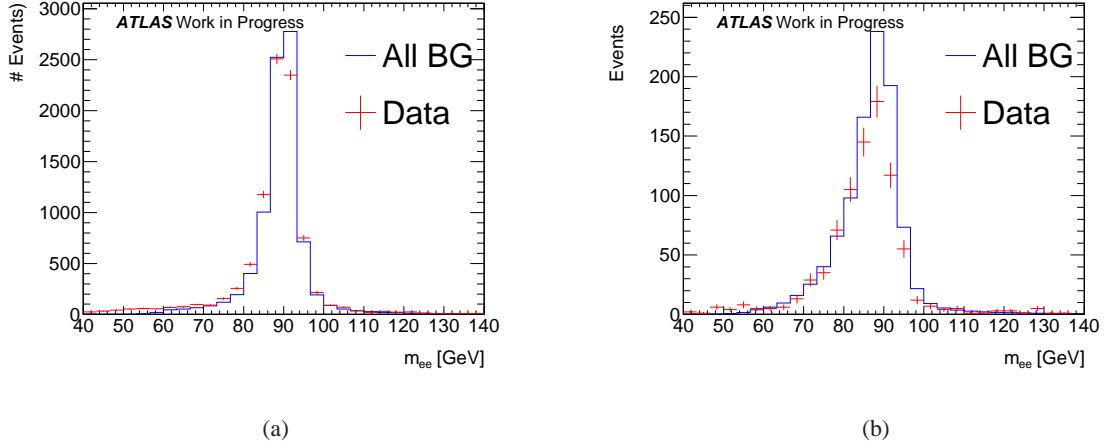


Figure 29: Invariant mass distributions for events with two opposite sign electrons, for the cases with (a) no electrons in the crack and (b) one electron in the crack. The dominant $Z + jets$ background MC is normalised so that there are the same number of data and MC events with $70 < m_{ee} < 110$ GeV in (a). This same normalisation is applied to (b).

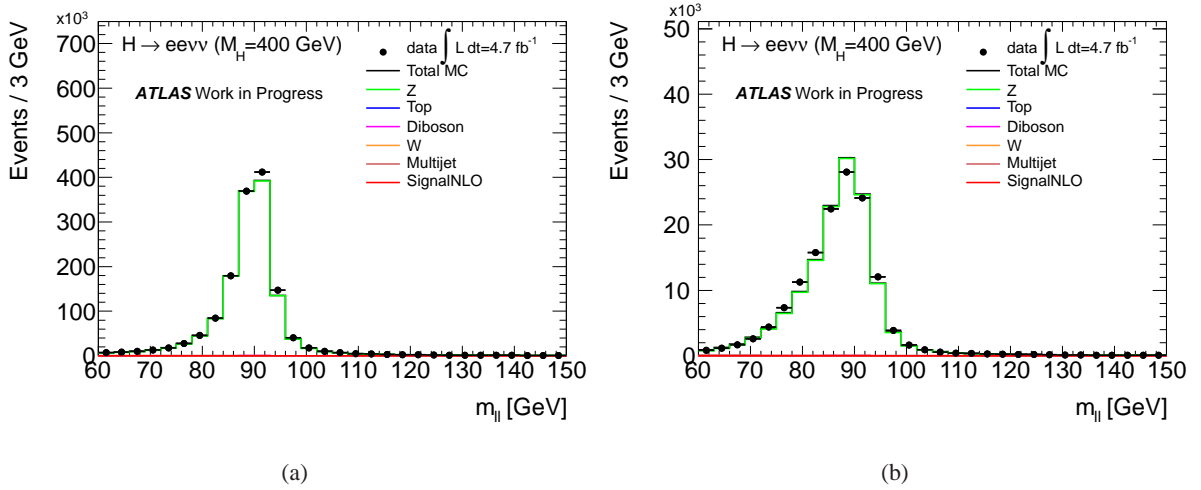


Figure 30: Invariant mass distributions for events with two opposite sign electrons, for the cases with (a) no electrons in the crack and (b) one electron in the crack. This plot is from the analysis described in chapter 6.

The same normalisation factor is then applied to the MC in fig. 29 (b). The agreement between MC and data in fig. 29(b) indicates that the energy response of electrons in the crack region is reasonably well described. A dedicated systematic for electrons in the crack region is applied to account for the loss in efficiency.

The width of the di-electron invariant mass gives a direct indication of the energy resolution of the

electrons in the different detector regions. For events where there are no electrons in the crack region the width of the m_{ee} distribution is measured to be 3.9 GeV, and for events with at least one electron in the crack region this width is broadened to 5.6 GeV. The resolution is well described by the MC in both cases.

For these reasons it was decided that in searches conducted on the 2011 dataset and beyond all three of the affected Higgs boson search channels, $H \rightarrow ZZ \rightarrow llll$, $H \rightarrow ZZ \rightarrow ll\nu\nu$ and $H \rightarrow ZZ \rightarrow llbb$ would not include a crack region veto for electrons.

As statistics were very limited in the 2010 dataset the same study was repeated using the 2011 dataset. Fig. 30 shows the m_{ee} distributions for events without (a) and with (b) an electron in the crack from the analysis described in chapter 6, which uses an increased dataset of 4.7 fb^{-1} . With the increased statistics a good agreement between data and MC is observed.

5.11 Results from 2010 dataset

In this sub-section the first Higgs boson searches conducted at ATLAS on real data for the high mass $H \rightarrow ZZ$ channels are presented. These searches were done over a dataset corresponding to an integrated luminosity between 35 pb^{-1} and 40 pb^{-1} . For the $H \rightarrow ZZ \rightarrow llll$ channel the event selection follows that outlined in section 5.4, with the modifications described in section 5.10 also applied. The $H \rightarrow ZZ \rightarrow ll\nu\nu$ and $H \rightarrow ZZ \rightarrow llqq$ channels share the same selection for a leptonic Z, and diverge in the latter selection. The detailed selection for these two channels can be found in [1], but a brief overview is given here.

$H \rightarrow ZZ \rightarrow ll\nu\nu$ and $H \rightarrow ZZ \rightarrow llqq$ common selection

- Events must pass single lepton triggers with p_T thresholds ranging between 10 – 15 GeV.
- All events must contain a primary vertex with at least 3 tracks associated to it.
- 2 same flavour leptons with $p_T > 20 \text{ GeV}$ are required, with no third electron or muon. Opposite charge requirement for muons only.
- The invariant mass of the lepton pair must lie within the range $76 < |m_{ll}| < 106 \text{ GeV}$.

$H \rightarrow ZZ \rightarrow ll\nu\nu$ selection

- $E_T^{miss} > 66 \text{ GeV}$. This cut is extended to 82 GeV for high Higgs masses ($m_H \geq 280 \text{ GeV}$).

- Reject events identified as likely to have contained a b-jet.
- Varying cuts on the opening angle of the leptons, depending on the Higgs mass.

$H \rightarrow ZZ \rightarrow llqq$ selection

- $E_T^{miss} < 50$ GeV.
- At least 2 jets whose invariant mass lies between $70 < m_{jj} < 105$ GeV.
- Additional Higgs mass dependent cuts on the opening angle of the two leptons and the two jets.

The final observed and expected limits for the $H \rightarrow ZZ$ channels based on the 2010 dataset are shown in fig 31.

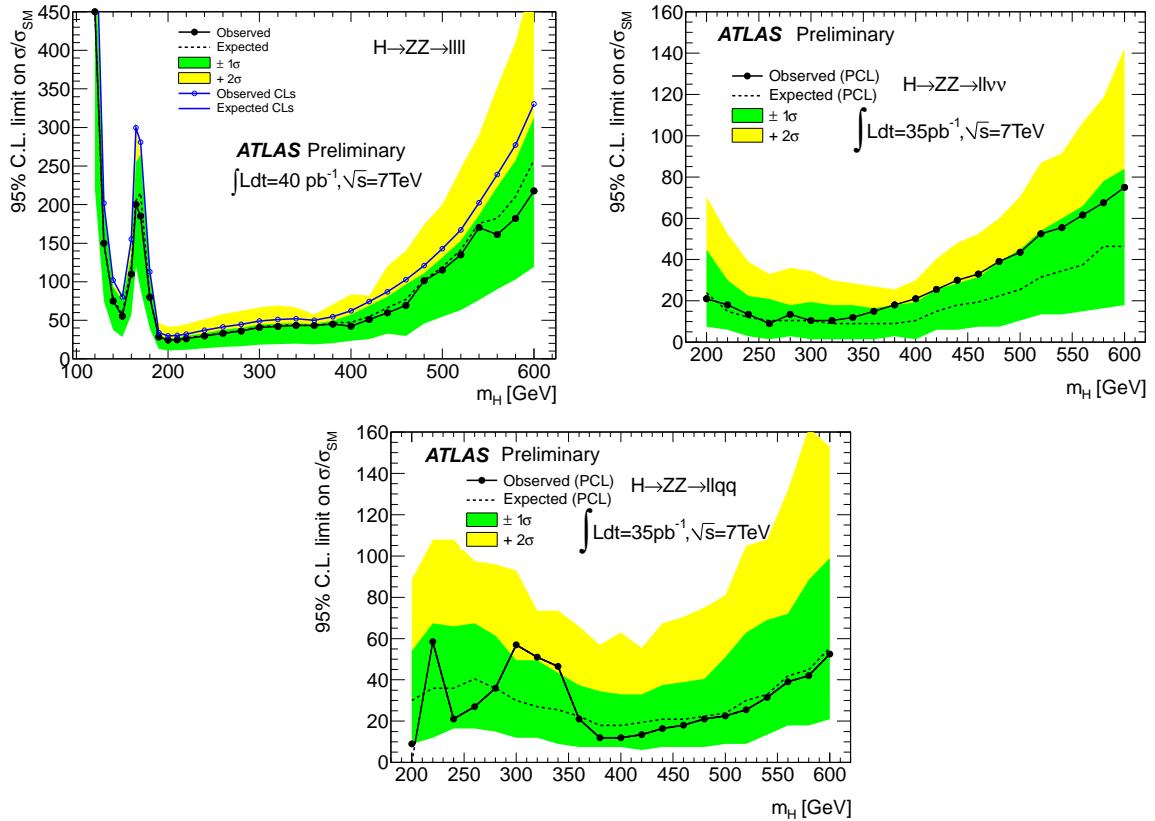


Figure 31: Exclusion limits for the 2010 dataset for the three Higgs search channels containing a leptonic Z; $H \rightarrow ZZ \rightarrow llll$ [40], $H \rightarrow ZZ \rightarrow llvv$ and $H \rightarrow ZZ \rightarrow llqq$ [1]. Both the observed (solid) and expected (dashed) line are shown.

For the $H \rightarrow ZZ \rightarrow llll$ channel the most significant results are obtained at $m_H = 200$ GeV where a Higgs boson can be excluded at 21 times the SM cross section. This is the mass region where this

channel has the best expected sensitivity (as indicated by a minimum in the expected exclusion limit).

The $H \rightarrow ZZ \rightarrow ll\nu\nu$ channel is most sensitive in the mass range $m_H = 320 - 380$ GeV, although the most significant result is at $m_H = 260$ GeV where there is an observed (expected) exclusion of a Higgs with 9 (9.5) times the SM cross section.

Finally for the $H \rightarrow ZZ \rightarrow llqq$ channel the best observed limit is at $m_H = 200$ GeV, where a Higgs boson with 8.5 times the SM cross section is excluded to a 95% confidence level, whilst the expected limit is 23.5. The most sensitive mass region is around $m_H = 400$ GeV. In conclusion it can be seen that the most sensitive channel at the higher Higgs masses for the early dataset is the $H \rightarrow ZZ \rightarrow ll\nu\nu$ channel.

Chapter 6

Search for the SM Higgs boson in the $H \rightarrow ZZ \rightarrow ll\nu\nu$ channel

In this section the search for the Standard Model Higgs in the $H \rightarrow ZZ \rightarrow ll\nu\nu$ channel is presented. This search was conducted throughout the 2011 data taking period, and after the publication of an initial paper [2] several updates were also published as conference notes [51, 72], which contained improvements to the event selection as well as an increased dataset. A final paper for the complete 2011 dataset was published in early 2012 [3], and it is this analysis which is presented in this chapter. This channel has contributed to the various ATLAS combined Higgs limits which were published throughout the year, the most notable of which announced the discovery of a new boson at around 125 GeV and can be found in [4].

6.1 The $H \rightarrow ZZ \rightarrow ll\nu\nu$ channel

In the high mass region, where $m_H > 200$ GeV, the Standard Model Higgs boson decays to two Z bosons with a high branching fraction. The $H \rightarrow ZZ \rightarrow llll$ channel, despite its excellent discrimination between background and signal, has limited sensitivity for an early search due to the small branching fraction for a Z to decay to either two electrons or two muons. Consequently the limits are dominated by statistical uncertainties. It is therefore beneficial to increase the statistics by extending the search using other channels, even if these additional channels have a poorer signal to background ratio.

A particularly useful additional channel is the $H \rightarrow ZZ \rightarrow ll\nu\nu$ which contains both a leptonically decaying Z boson and one that decays to two neutrinos. The branching ratio for a $Z \rightarrow \nu\nu$ decay is $(20 \pm 0.06)\%$ [58] which is six times higher than that of either $Z \rightarrow ee$ or $Z \rightarrow \mu\mu$ and therefore it is expected that there will be six times more $H \rightarrow ZZ \rightarrow ll\nu\nu$ events compared to $H \rightarrow ZZ \rightarrow llll$, ($l = e, \mu$). This is illustrated in fig. 32 which shows the cross section multiplied by the branching ratio for the $H \rightarrow ZZ \rightarrow ll\nu\nu$ and $H \rightarrow ZZ \rightarrow llll$ channels as a function of Higgs mass. The leptons considered in this plot include taus, and so the difference shown between the two channels is reduced to a factor of four.

The neutrinos from the Z boson decay are not directly detected by the ATLAS detector, but their presence is inferred from an imbalance in the vectorial sum of the transverse momenta in the event, E_T^{miss} ,

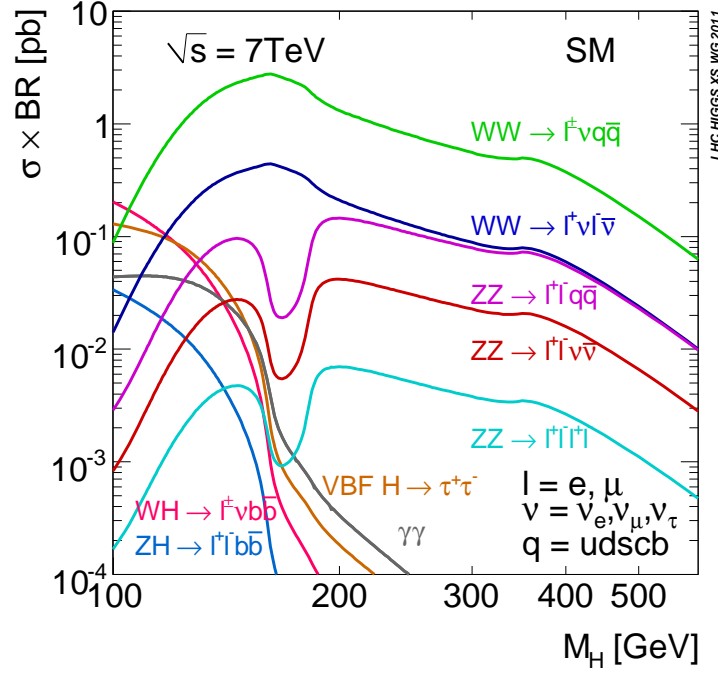


Figure 32: Branching fractions of the SM Higgs boson as a function of the Higgs mass [19]. The ZZ channels are shown separately.

which is defined in section 4.6. In order to observe a significant E_T^{miss} the Z boson decaying to neutrinos must be sufficiently boosted so that the two neutrinos are not back to back, as otherwise the missing energy from each neutrino would cancel out. Hence a Z boson with high momentum is required. When a Higgs boson decays to two on-shell Z bosons any left over mass-energy is transferred to the Z bosons as kinetic energy. Therefore high momentum Z bosons would be produced in particular from the decay of a high mass Higgs ($m_H \gg 2m_Z$), and high E_T^{miss} values can be used to distinguish these events. For lower Higgs masses ($m_H \approx 200$ GeV or less) no significant E_T^{miss} values are expected and inclusive $Z \rightarrow ll$ decays form an important background. As a result, this channel is most sensitive at the higher range of Higgs masses.

The selection of $H \rightarrow ZZ \rightarrow ll\nu\nu$ events is outlined in detail in section 6.5, but the general strategy is to first select the leptonic Z by requiring an electron or muon pair with an invariant mass consistent with the Z mass, then to apply cuts that are sensitive to the kinematic nature of a high mass Higgs decaying to a Z pair. These latter cuts are on the E_T^{miss} of the event and the azimuthal opening angle of the lepton pair. Additional cuts are applied to reject events with jets likely to have originated from b-quarks, as well as cuts that ensure the quality and authenticity of the E_T^{miss} reconstruction. The final search is performed by looking for a peak above background expectations in the transverse mass distribution determined from

the transverse momentum of the lepton pair and the E_T^{miss} vector in the event. The transverse mass is defined in the same way as [73, 74], and is given in equation 53.

$$m_T^2 \equiv \left[\sqrt{m_Z^2 + |\vec{P}_T^{ll}|^2} + \sqrt{m_Z^2 + |\vec{P}_T^{miss}|^2} \right]^2 - \left[\vec{P}_T^{ll} + \vec{P}_T^{miss} \right]^2. \quad (53)$$

This definition explicitly assumes that both the dilepton pair as well as the E_T^{miss} originate from a Z boson decay.

6.1.1 Expected sensitivity with 1fb^{-1}

A pre-data study was conducted comparing the sensitivity in the high mass range for the three ZZ channels. The results for the $H \rightarrow ZZ \rightarrow llll$ channel from this study have already been presented in chapter 5. The expected exclusion limits with 1fb^{-1} of data for all three $H \rightarrow ZZ$ channels are shown in fig. 33 where it can be seen that the $H \rightarrow ZZ \rightarrow ll\nu\nu$ channel is expected to be the most sensitive for an early exclusion in the high Higgs mass range. The individual expected limits for the $H \rightarrow ZZ \rightarrow ll\nu\nu$ channel expressed in multiples of the predicted SM rate as a function of the Higgs mass are shown in fig. 34. The most sensitive mass point for this channel is expected to be $m_H = 380\text{ GeV}$ where a Higgs boson would be almost excluded to 95% confidence level.

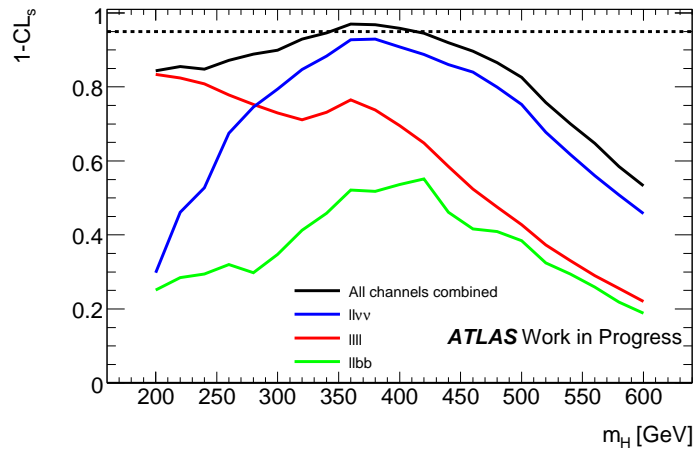


Figure 33: Expected exclusion limits for the $H \rightarrow ZZ \rightarrow llll$, $H \rightarrow ZZ \rightarrow ll\nu\nu$ and $H \rightarrow ZZ \rightarrow llbb$ channels as a function of Higgs mass. The limits correspond to 1fb^{-1} of data at $\sqrt{s} = 7\text{ TeV}$ [57].

6.2 Background samples

Several background processes that can mimic the final state of the signal are considered in this analysis.

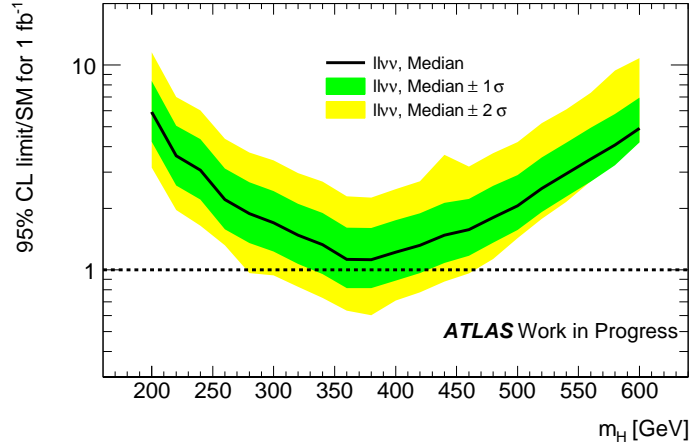


Figure 34: Expected exclusion limits for the $H \rightarrow ZZ \rightarrow ll\nu\nu$ channel, expressed as the fraction of the Standard Model Higgs cross section that would be excluded at 95% confidence level. The green and yellow bands indicate the expected sensitivity with $\pm 1\sigma$ and $\pm 2\sigma$ statistical fluctuations respectively. The limits correspond to 1 fb^{-1} of data at $\sqrt{s} = 7 \text{ TeV}$.

6.2.1 ZZ background

The main background for SM ZZ production is from the SM $ZZ \rightarrow ll\nu\nu$ decay mode, where $l = e, \mu$, which has an identical final state to that of the signal. Background processes from $ZZ \rightarrow llqq$, $ZZ \rightarrow \tau\tau qq$, $ZZ \rightarrow llll$, $ZZ \rightarrow ll\tau\tau$ and $ZZ \rightarrow \tau\tau\tau\tau$ decays are also considered, and these backgrounds are referred to throughout this chapter collectively as the ZZ background.

The ZZ samples are simulated using the MC@NLO [60] event generator interfaced with HERWIG and JIMMY 4.31 [61] for simulation of the underlying event. The calculation includes hard scattering diagrams to NLO accuracy, but only for on shell Z bosons. Alternate inclusive PYTHIA samples, calculated including hard scattering diagrams to LO accuracy, scaled using k-factors which do include the contribution from off-shell bosons, are used to determine the systematic uncertainty of the ZZ background, as described in section 6.7. For this channel the effect of not including the off-shell component is not as important as that presented in section 5.3.1 because the most sensitive region is at a higher Higgs mass where a larger fraction of the Z bosons will be on shell. Details of the ZZ samples are given in table 12.

6.2.2 WZ and WW background

Other diboson backgrounds with genuine E_T^{miss} are also considered; the $WZ \rightarrow lvll$, which can mimic the final state of the signal if the lepton from the $W \rightarrow lv$ decay is missed; and $WW \rightarrow lvlv$, which has

channel	σ (fb)
$ZZ \rightarrow llqq/\tau\tau qq$	841.5
$ZZ \rightarrow ll\nu\nu$	160.4
$ZZ \rightarrow llll$	27.0
$ZZ \rightarrow ll\tau\tau$	27.0
$ZZ \rightarrow \tau\tau\tau\tau$	6.8
$ZZ \rightarrow \tau\tau\nu\nu$	80.3

Table 12: The ZZ samples (where $l = e, \mu$) generated using the MC@NLO Monte Carlo programs. The cross sections are calculated to NLO [75] and convoluted with Z branching fractions from [58].

an identical final state to the signal, but a much different topology.

These backgrounds are simulated using the MC@NLO generator interfaced with HERWIG and JIMMY for the underlying event. All possible leptonic final states are considered, including τ decays. The cross sections are calculated to NLO accuracy, details of which can be found in table 13.

channel	σ (fb)
W^+W^-	46230
W^+Z	11500
W^-Z	6500

Table 13: The MC@NLO WW and WZ background Monte Carlo samples. The cross sections are calculated to NLO [75] and convoluted with branching fractions from [58].

6.2.3 Z + jets background

Leptonic Z decays with or without jets have no real E_T^{miss} , so this background only contributes in events with high fake E_T^{miss} , either from a poorly reconstructed jet or as a result of high pileup conditions. Although only a very small fraction of the total Z + jets events will contribute to the background in this search, the abundance of Z events makes it an important background to consider.

Background samples for $Z \rightarrow ee$, $Z \rightarrow \mu\mu$ and $Z \rightarrow \tau\tau$ are simulated using the ALPGEN Monte Carlo program [66] interfaced with HERWIG [76] for parton showers and hadronisation. The program generates hard matrix elements for Z and $Zb\bar{b}$ production with additional numbers of partons p in the final state, where p runs from 0 to 5. The cross sections, listed in table 14, include a k-factor of 1.25 to

make the inclusive Z cross section agree with NLO calculations [75]. Dedicated samples for $Z \rightarrow ee$, $Z \rightarrow \mu\mu$ or $Z \rightarrow \tau\tau$ with additional b-jets are also produced with the same generator. To remove a small double counting between the inclusive and b-jet samples the overlap removal procedure described in [67] is used. Details of all $Z + jets$ samples are given in table 14. All samples used correspond to luminosities of 8.0 fb^{-1} or greater.

For systematic checks further samples of $Z \rightarrow ee$, $Z \rightarrow \mu\mu$ and $Z \rightarrow \tau\tau$ are simulated using the PYTHIA 6.421 interfaced to PHOTOS [77], for initial state radiation, and TAUOLA [78], for the simulation of the τ decays. The simulation of Z production includes the Drell-Yan γ component and the $Z\gamma$ interference term, and a minimum mass of 60 GeV is required for the boson. The cross sections are scaled to the NLO values from [79].

process	generator	$\sigma(\text{fb})$
$Z + 0p, Z \rightarrow ee$	MC@NLO	836000
$Z + 1p, Z \rightarrow ee$	MC@NLO	168000
$Z + 2p, Z \rightarrow ee$	MC@NLO	50500
$Z + 3p, Z \rightarrow ee$	MC@NLO	14000
$Z + 4p, Z \rightarrow ee$	MC@NLO	3510
$Z + 5p, Z \rightarrow ee$	MC@NLO	988
$Zb\bar{b} + 0p, Z \rightarrow ee$	MC@NLO	8208
$Zb\bar{b} + 1p, Z \rightarrow ee$	MC@NLO	3100
$Zb\bar{b} + 2p, Z \rightarrow ee$	MC@NLO	1113
$Zb\bar{b} + 3p, Z \rightarrow ee$	MC@NLO	488
$Z \rightarrow ee$	PYTHIA	911.6
$Z \rightarrow \mu\mu$	PYTHIA	911.6
$Z \rightarrow \tau\tau$	PYTHIA	911.6

Table 14: The $Z + jets$ samples generated using the ALPGEN Monte Carlo program interfaced with HERWIG, where p refers to the number of additional partons generated in the matrix element and inclusive PYTHIA samples. The cross sections listed are for $\sqrt{s} = 7 \text{ TeV}$ and include a k -factor of 1.25. For the ALPGEN samples the cross sections for $Z \rightarrow \mu\mu$ and $Z \rightarrow \tau\tau$ are taken to be the same as those for $Z \rightarrow ee$.

6.2.4 $t\bar{t}$ and single top background

Top pair production forms a background to the final $ll\nu\nu$ selection when the two W bosons produced in a $t\bar{t}$ decay undergo leptonic decays, and the b -jets are not identified. It contains genuine E_T^{miss} and although only a small fraction of the total top events will survive all cuts it is a significant background due to the large number of top events expected.

Background samples of $t\bar{t}$ production as well as single top and Wt production are simulated using the MC@NLO event generator interfaced to HERWIG and JIMMY, except for the t-channel single top quark production, for which AcerMC [80] generator is used. The $t\bar{t}$ sample is filtered at generator level to require at least one lepton originating from a W boson with a $p_T > 1$ GeV. This ensures only events with at least one leptonic W decay are retained, where $l = e, \mu, \tau$. The case where both W bosons decay hadronically is not considered. Details of the $t\bar{t}$ sample are given in table 15.

channel	σ (fb)	filter	$\sigma_{filtered}$ (fb)
$t\bar{t}$	166800	0.5562	92774
single t (s-chan, $W \rightarrow e\nu$)	497		
single t (s-chan, $W \rightarrow \mu\nu$)	489		
single t (s-chan, $W \rightarrow \tau\nu$)	520		
single t (t-chan, $W \rightarrow e\nu$)	6941		
single t (t-chan, $W \rightarrow \mu\nu$)	6825		
single t (t-chan, $W \rightarrow \tau\nu$)	7264		
Wt	15740		

Table 15: The $t\bar{t}$ samples in the lepton-hadron (lh) or lepton-lepton (ll) decay mode and the single top and Wt samples, all generated using the MC@NLO Monte Carlo program interfaced with HERWIG and JIMMY. The $t\bar{t}$ filter requires at least one of the W bosons from the top decays to decay leptonically. The cross sections are taken from the best known theory estimation recommended by the ATLAS top working group [81]. The cross section is convoluted with branching fractions taken from the Particle Data Book [58].

6.2.5 Inclusive W background

Inclusive W production is expected to be a small background for this analysis as it only contributes when a jet is misidentified as a lepton, and the kinematics of the genuine and fake lepton are such that they are misidentified as having come from a Z decay.

Background samples for $W \rightarrow e\nu$, $W \rightarrow \mu\nu$ and $W \rightarrow \tau\nu$ are simulated using the ALPGEN Monte

Carlo program [66] interfaced with HERWIG [76] for parton showers and hadronisation. The program generates hard matrix elements for W , Wc , $Wc\bar{c}$ and $Wb\bar{b}$ and production with additional numbers of partons p in the final state, where p runs from 0 to 5. As was the case for the Z samples, the small double counting between the inclusive, b-jet and c-jet samples is removed using the procedure described in [67].

The cross sections, listed in table 16, include a k-factor of 1.2 to make the inclusive W cross section agree with NLO calculations [75].

This background mainly affects the electron channel because the rate of jets faking electrons is much higher than the rate of jets faking muons. To account for an over estimation in the electron mis-identification rate in the simulation, which affects this background in particular, a scale factor of 0.5 is applied. Details of the procedure used to determine this scale factor are given in section 6.6. This is applied for all plots containing the W background unless stated otherwise.

6.2.6 QCD background

The QCD background requires two fake leptons and fake E_T^{miss} . Although this background has a high production cross section it is found to be a very small background. QCD multijet production is evaluated from a data-driven estimate for the electron channel, as described in section 6.6. In the muon channel this background is expected to be very small, as the only significant contribution is from semi-leptonic c and b hadron decays. These events are simulated using the PYTHIA 6.421 [62] event generator via the dedicated PYTHIAB [82] interface. Samples of $b\bar{b}$ and $c\bar{c}$ production are generated where one of the b or c hadrons is required to decay to a muon with $P_T > 15$ GeV and $|\eta| < 2.5$. Details of these samples are given in table 17. The control regions and data driven methods for these backgrounds are presented in section 6.6.

6.3 Signal samples

The main focus of this analysis is to look for genuine $H \rightarrow ZZ \rightarrow ll\nu\nu$ events, but there can also be events from other Higgs decay channels that survive all cuts. Each of these channels has its own separate dedicated search, but by keeping the cuts between these searches orthogonal any selected events from these samples can be considered as part of the signal. One can then still combine all channels for a complete Higgs search without any worry of double counting.

Simulated signal samples of $H \rightarrow ZZ \rightarrow ll\nu\nu$, $H \rightarrow ZZ \rightarrow llqq$, $H \rightarrow ZZ \rightarrow ll\mu\mu$, and $H \rightarrow WW \rightarrow ll\nu\nu$ where $l = e, \mu, \tau$ and $q = d, u, s, c, b$ have been generated using the PowHeg [83] generator interfaced with Pythia [62] showering including matrix elements up to next-to-leading order. Both gluon-gluon

process	$\sigma(\text{fb})$
$W + 0p, W \rightarrow e\nu$	8300000
$W + 1p, W \rightarrow e\nu$	1560000
$W + 2p, W \rightarrow e\nu$	453000
$W + 3p, W \rightarrow e\nu$	122000
$W + 4p, W \rightarrow e\nu$	30900
$W + 5p, W \rightarrow e\nu$	8380
$Wb\bar{b} + 0p$	56800
$Wb\bar{b} + 1p$	42900
$Wb\bar{b} + 2p$	20800
$Wb\bar{b} + 3p$	7960
$Wc\bar{c} + 0p$	153000
$Wc\bar{c} + 1p$	125000
$Wc\bar{c} + 2p$	625000
$Wc\bar{c} + 3p$	20400
$Wc + 0p$	51800
$Wc + 1p$	192000
$Wc + 2p$	51000
$Wc + 3p$	119000
$Wc + 4p$	27600
$W \rightarrow e\nu$	9676075
$W \rightarrow \mu\nu$	9514057
$W \rightarrow \tau\nu$	10126125

Table 16: The W +jet samples generated using the ALPGEN Monte Carlo program interfaced with HERWIG, where p refers to the number of additional partons generated in the matrix element. The cross sections listed include a k -factor of 1.25. The cross sections for $W \rightarrow \mu\nu$ and $W \rightarrow \tau\nu$ are assumed the same as those for $W \rightarrow e\nu$.

fusion and vector boson fusion production mechanisms are taken into account by the matrix elements. PYTHIA has been interfaced to PHOTOS [77], for initial state radiation, and TAUOLA [78], for the simulation of the τ decays. In addition, a dedicated set of $gg \rightarrow H \rightarrow ZZ \rightarrow ll\nu\nu$ signal samples are used to estimate the shape uncertainty of the nominal sample by varying the theory parameters. For this study

channel	$\sigma(\text{fb})$
$bb \rightarrow \mu\mu$	7.39×10^7
$cc \rightarrow \mu\mu$	2.84×10^7

Table 17: The bb and cc samples generated using the PYTHIA Monte Carlo program via the PYTHIAB interface. The cross sections include diagrams to LO and are taken from PYTHIA. Due to the very large production cross section, the size of these samples correspond to only few percent of the corresponding amount of data analysed in the analysis.

only the dominant gg fusion process is considered. These samples are generated with PowHeg [83].

In all cases the cross sections for Higgs production via gg fusion are set to NNLO+NNLL+EW accuracy and those for vector boson fusion are evaluated at NLO+EW accuracy [59]. Details of the simulated signal samples are given in table 18. All signal samples correspond to luminosities that are high ($\sim 150 \text{ fb}^{-1}$ or more) compared to the available luminosity in the data.

6.4 The 2011 dataset

The data sample used in this analysis is the full dataset recorded by the ATLAS detector during 2011 when the LHC was running at a centre-of-mass energy of 7 TeV. The data are subsequently required to satisfy a number of conditions ensuring that all essential elements of the ATLAS detector were operational with good efficiency during data taking. This is implemented using a Good Run List (GRL) based on the ATLAS Data Quality flags. The GRL used for this analysis is a standard ATLAS GRL defined for $W/Z + jets$ cross section measurements and therefore only contains runs where all parts of the detector were functional, which is crucial to ensure reliable E_T^{miss} performance. The total integrated luminosity after these requirements is 4.7 fb^{-1} .

6.4.1 Pile-up in the data and MC samples

In order to maximise the total integrated luminosity taken in 2011 several of the beam parameters were optimised throughout the year. In particular a reduction in β^* resulted in a sharp jump in the average number of interactions per bunch crossing, $\langle \mu \rangle$. As a result, the data taken towards the latter part of the year are more heavily effected by in time pileup (for details see section 4.1.4). For the first 2.3 fb^{-1} of the 2011 data the peak in the μ distribution is at approximately $\langle \mu \rangle = 6$ whereas in the latter half of the 2011 data, which corresponds to a luminosity of 2.4 fb^{-1} , the peak is at $\langle \mu \rangle = 12$. Variations in $\langle \mu \rangle$

m_H (GeV)	$H \rightarrow ZZ \rightarrow ll\nu\nu$ σ (fb)	$H \rightarrow ZZ \rightarrow llqq$ σ (fb)	$H \rightarrow ZZ \rightarrow llll$ σ (fb)	$H \rightarrow WW \rightarrow l\nu l\nu$ σ (fb)
200	60.86	212.7	15.36	462.68
220	55.40	193.6	13.99	365.83
240	48.03	167.9	12.13	302.09
260	41.92	146.5	10.58	257.36
280	37.35	130.6	9.43	224.28
300	33.71	117.8	8.51	199.60
320	31.33	109.5	7.91	183.47
340	30.49	106.6	7.70	176.92
360	30.72	107.4	7.75	176.85
380	27.54	96.3	6.95	157.87
400	23.87	83.4	6.03	135.63
420	20.06	70.1	5.06	112.96
440	16.89	59.0	4.26	94.52
460	14.20	49.6	3.58	79.05
480	11.88	41.5	3.00	65.79
500	9.96	34.8	2.51	54.71
520	8.37	29.2	2.11	45.89
540	7.04	24.6	1.78	38.32
560	5.93	20.7	1.50	32.15
580	5.03	17.6	1.27	27.15
600	4.23	14.8	1.07	22.80

Table 18: The $H \rightarrow ZZ \rightarrow ll\nu\nu$, $H \rightarrow ZZ \rightarrow llqq$, $H \rightarrow ZZ \rightarrow llll$, and $H \rightarrow WW \rightarrow l\nu l\nu$ ($l = e, \mu, \tau$ and $q = u, d, s, c, b$) signal Monte Carlo samples shown for a range of Higgs masses. The cross sections are a combination of the gg and VBF fusion processes and are evaluated from theoretical calculations [59] for H production convoluted with Higgs branching fractions from [59] and Z branching fractions from [58].

are accounted for when simulating the MC by generating a varying number of additional interactions which correspond to the various periods of data taking for a sub set of each MC sample. These separate periods are then appropriately reweighted such that the luminosity of each subset is the same as the luminosity of the corresponding data period.

6.4.2 Triggers

The changing run conditions throughout the year also had an effect on the triggers. As the luminosity increased the p_T thresholds of the single lepton triggers needed to be increased to keep the trigger rates at a manageable level. For this analysis the lowest p_T un-prescaled single electron and single muon triggers available throughout the year are used together with di-electron triggers for the electron channel, which are included to make the selection more robust against possible uncertainties around the trigger thresholds. The p_T thresholds for the single electron triggers vary from 20 to 22 GeV. The di-electron trigger has a constant p_T threshold of 12 GeV. For muons the p_T threshold remained at 18 GeV.

For the trigger combinations used in this analysis the trigger efficiency for MC signal events containing two electrons with $p_T > 20$ GeV and $p_T > 22$ GeV is greater than 99.9%, and for MC signal events containing two muons with $p_T > 20$ GeV this efficiency ranges between 95% and 97%. Electron and muon trigger efficiencies in ATLAS are verified on data using a tag and probe method described in section 4.3 and [43,44]. Where appropriate correction factors are applied to the MC.

6.5 Event selection

The event selection for the $H \rightarrow ZZ \rightarrow ll\nu\nu$ analysis was optimised to give the highest exclusion sensitivity with 1 fb^{-1} of data. It is split up into a preselection which selects events containing Z bosons that is shared with the $H \rightarrow ZZ \rightarrow llqq$ analysis and then makes further cuts specific to the $H \rightarrow ZZ \rightarrow ll\nu\nu$ channel.

6.5.1 Preselection

Firstly all data events are required to pass the Good Runs list selection, as described in section 6.4, and also pass the trigger selection outlined in section 6.4.2. All triggered events are required to contain a vertex with at least three tracks associated to it. In order to ensure that the jets in the event are of good quality a jet cleaning procedure is followed. This takes into account the fraction of energy in the EMCAL and the HEC, the fraction of energy in each layer of the EMCAL and the fraction of energy in LAr cells in which the predicted and measured pulse shape vary too much. This cut removes events with jets likely to be caused or affected by hardware problems or cosmic ray showers, which can ultimately lead to poorly described high tails in the E_T^{miss} distribution. In addition to this events in both data and MC are also removed if a jet with $P_T > 40$ GeV enters the region in which the electro-magnetic calorimeter was not fully active due to failed front-end electronics. The jet P_T is first corrected to account for the missed energy.

The events are required to contain exactly two same flavour leptons with $p_T > 20$ GeV and with opposite charge. Events containing a third lepton with $p_T > 10$ GeV are rejected to reduce contamination from WZ events. The leptonic Z boson is then formed from these two leptons. To ensure that the leptons are consistent with having originated from a Z boson decay a further constraint requiring that the invariant mass of the lepton pair lies within ± 15 GeV of the Z boson mass is applied. This mass window cut strongly reduces the background from events that do not contain a genuine Z boson decay; mainly the $t\bar{t}$, WW and QCD backgrounds. The dilepton invariant mass for a combination of both the $ee\nu\nu$ and $\mu\mu\nu\nu$ channels is shown in fig. 35 after the complete preselection has been applied.

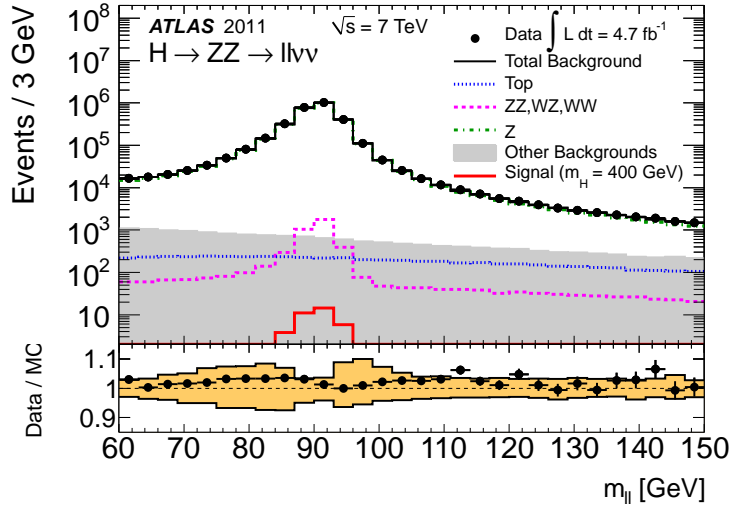


Figure 35: The dilepton invariant mass for the $H \rightarrow ZZ \rightarrow ll\nu\nu$ channel for both the muon and electron channels combined in events containing two leptons.

6.5.2 $H \rightarrow ZZ \rightarrow ll\nu\nu$ selection

$H \rightarrow ZZ \rightarrow ll\nu\nu$ events are characterised by high E_T^{miss} in the opposite direction to a high momentum leptonic Z decay and the main cuts in the analysis are chosen to reflect this topology. Additionally, to reduce the impact of the $t\bar{t}$ background events identified as having contained a b-jet are rejected. As it is crucial for this analysis that the performance of the E_T^{miss} measurement in the ATLAS detector is well understood, additional cuts to improve this performance are applied. These reject events where the direction of the E_T^{miss} is not back-to-back with the reconstructed Z or a jet. These cuts were optimised to give the best sensitivity for a low luminosity dataset (1 fb^{-1}) and are described in detail below. Two different sets of selection criteria are applied, one optimised for a low Higgs mass ($m_H < 280$ GeV), and one for a high Higgs mass ($m_H \geq 280$).

- For $m_H < 280$ GeV the missing transverse energy is required to exceed 66 GeV, while for $m_H \geq 280$ GeV the minimum required E_T^{miss} value is 82 GeV. The E_T^{miss} is calculated as described in section 4.6. The distribution of the E_T^{miss} after the dilepton mass window cut is shown in fig. 36(a) and fig. 37(a) for the $H \rightarrow ZZ \rightarrow ee\nu\nu$ and $H \rightarrow ZZ \rightarrow \mu\mu\nu\nu$ channels respectively.
- With increasing Higgs mass the Z bosons from the Higgs decay become more boosted, therefore a mass dependent upper limit is applied to the azimuthal angle between the two leptons. For $m_H < 280$ GeV this requirement is $\Delta\phi_{ll} < 2.64$, while for $m_H \geq 280$ GeV the requirement is $\Delta\phi_{ll} < 2.25$. At the lower Higgs masses the boost of the Z bosons is expected to be moderate and hence for $m_H < 280$ GeV an additional lower limit of $\Delta\phi_{ll} > 1$ is applied. The distribution of $\Delta\phi_{ll}$ after the dilepton mass window cut is shown in fig. 36(b) and fig. 37(b) for the $H \rightarrow ZZ \rightarrow ee\nu\nu$ and $H \rightarrow ZZ \rightarrow \mu\mu\nu\nu$ channels respectively.
- Events are rejected if they contain a jet which has been identified as more than 80% likely to be a b -jet, using the b -tagging method described in section 4.4.1. This significantly reduces the top background. The distribution of the maximum b -tagging weight in the event, after the dilepton mass window cut, is shown in fig. 36(c) and fig. 37(c) for the $H \rightarrow ZZ \rightarrow ee\nu\nu$ and $H \rightarrow ZZ \rightarrow \mu\mu\nu\nu$ channels respectively.
- In the high mass region, where the E_T^{miss} is expected to be back-to-back with the Z candidate, an additional cut is applied on the azimuthal angle between the Z candidate and the E_T^{miss} . For $m_H \geq 280$ GeV it is required that $\Delta\phi_{Z, \vec{p}_T^{miss}} > 1$. The $\Delta\phi_{Z, \vec{p}_T^{miss}}$ distribution after the dilepton mass window cut is shown in fig. 36(d) and fig. 37(d).
- Finally to avoid selecting events with a high E_T^{miss} originating from a badly measured jet, events are rejected if the phi opening angle between the E_T^{miss} vector and the nearest jet is $\Delta\phi_{\vec{p}_T^{miss}, Jet} \leq 1.5$ (for $m_H < 280$ GeV) and $\Delta\phi_{\vec{p}_T^{miss}, Jet} \leq 0.5$ (for $m_H \geq 280$ GeV). Only jets with $p_T > 25$ GeV and $|\eta| < 2.5$ are considered for this cut. The distribution of $\Delta\phi_{\vec{p}_T^{miss}, Jet}$ after the dilepton mass window cut is shown in fig. 36(e) and fig. 37(e).

After the above selection the search for $H \rightarrow ZZ \rightarrow ll\nu\nu$ is performed by looking for a peak above background expectation in the transverse mass distribution of the $ee\nu\nu$ and $\mu\mu\nu\nu$ systems.

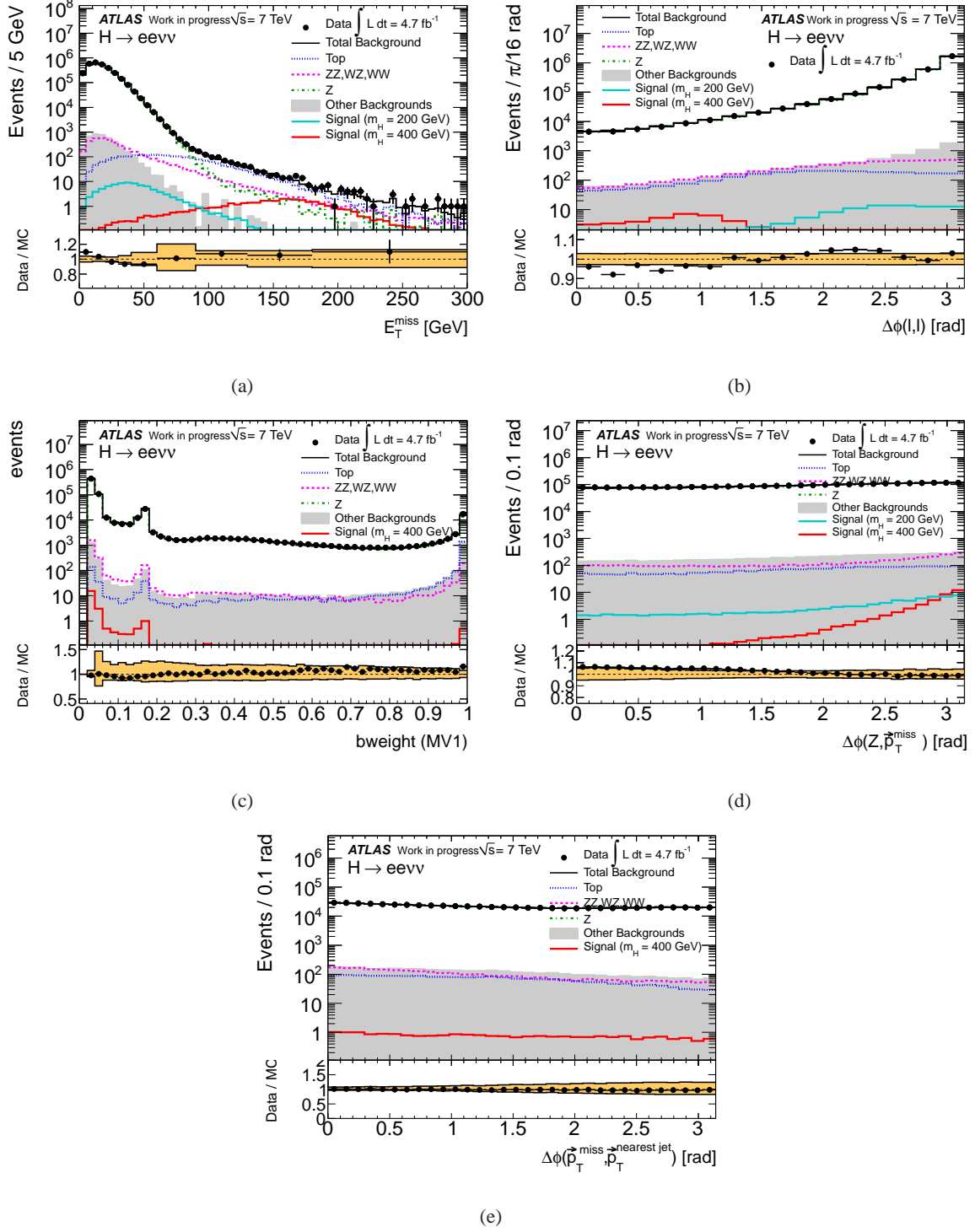


Figure 36: Kinematic distributions relevant to the $H \rightarrow ZZ \rightarrow eev\nu$ analysis for the Higgs boson signal and the main backgrounds: (a) E_T^{miss} , (b) the opening angle between the leptons, $\Delta\phi_{ll}$, (c) the maximum MV1 b-tagging weight, (d) the opening angle between the lepton pair and the \vec{p}_T^{miss} , $\Delta\phi_{ll, \vec{p}_T^{\text{miss}}}$ and (e) the opening angle between the \vec{p}_T^{miss} and the nearest jet, $\Delta\phi_{\vec{p}_T^{\text{miss}}, \text{Jet}}$, in the event. The signal sample shown corresponds to a Higgs with $m_H = 400$ GeV. The bottom plot shows the ratio between data and the combined MC background samples as well as a band formed by adding in quadrature all systematic uncertainties.

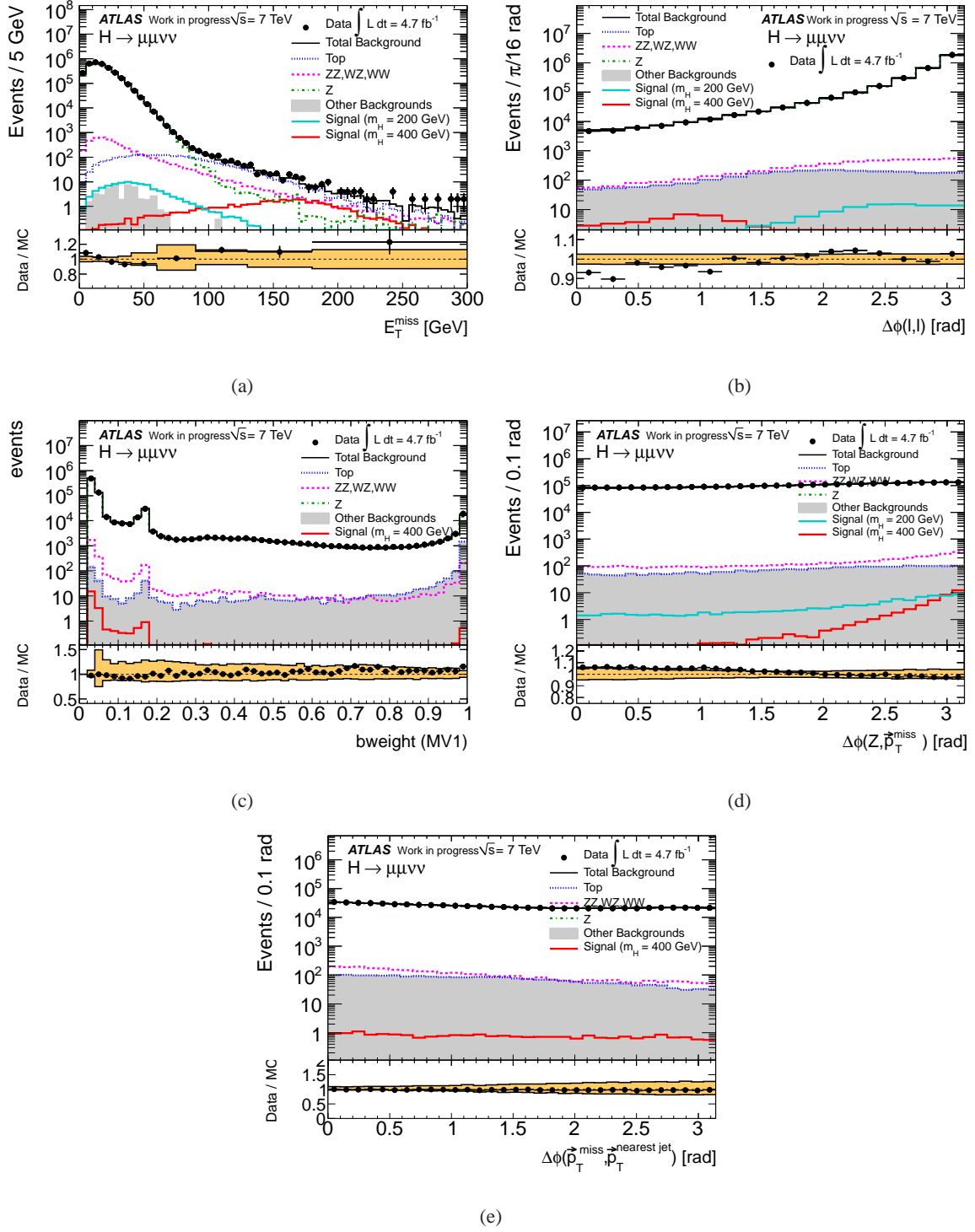


Figure 37: Kinematic distributions relevant to the $H \rightarrow ZZ \rightarrow \mu\nu\nu$ analysis for the Higgs boson signal and the main background: (a) E_T^{miss} , (b) the opening angle between the leptons, $\Delta\phi_{ll}$, (c) the maximum MV1 b -tagging weight, (d) the opening angle between the lepton pair and the \vec{p}_T^{miss} , $\Delta\phi_{ll, \vec{p}_T^{\text{miss}}}$ and (e) the opening angle between the \vec{p}_T^{miss} and the nearest jet, $\Delta\phi_{\vec{p}_T^{\text{miss}}, \vec{p}_T^{\text{nearest jet}}}$ in the event. The signal sample shown corresponds to a Higgs with $m_H = 400$ GeV. The bottom plot shows the ratio between data and the combined MC background samples as well as a band formed by adding in quadrature all systematic uncertainties.

6.6 Background control regions and data driven estimates

In order to ensure that the shape of backgrounds taken directly from MC are accurate and that the normalisation is correct a number of the cuts outlined in section 6.5 are inverted to obtain distributions that are dominated as much as possible by a single background. It is also important that the phase space of these control regions is not too far removed from that of the signal. Multiple control regions are used for the same backgrounds where appropriate. Control regions are presented for all of the backgrounds taken from MC except the irreducible $ZZ \rightarrow ll\nu\nu$ background, for which there is no such control region, and the $WW \rightarrow l\nu l\nu$ background. Also presented are the methods used to obtain entirely data-driven background samples.

6.6.1 ZZ background

As mentioned above the $ZZ \rightarrow ll\nu\nu$ background is irreducible. Any cuts specifically designed to isolate this background would also contain a potential signal and therefore no control region is used. The MC@NLO MC generator is used to simulate this sample, with an alternate PYTHIA sample used to determine a systematic on the shape difference of the final distribution. As was shown and discussed in section 5.3.1 when the samples are scaled to NLO the agreement between these samples is to within 10%. This number will be included in the normalisation systematic for the ZZ sample.

6.6.2 Top and W control regions

As these two backgrounds are the only significant backgrounds that do not contain a genuine Z decay the control regions for each of them are similar. Three different methods are outlined here based on inverting the Z boson mass window cut, selecting like sign lepton pairs and also using events with an electron-muon pair.

Events which have a lepton pair with an invariant mass that lies outside of the ± 15 GeV window of the Z boson mass are defined as having come from the m_{ll} sidebands. A lower and upper limit of $60 < m_{ll} < 150$ GeV is also applied.

Fig. 38(a) shows the E_T^{miss} distribution for events with two same flavour leptons in the m_{ll} sidebands that contain a b -tagged jet. At high E_T^{miss} top events dominate; for $E_T^{miss} > 66$ GeV there are 1439 observed events, compared to 1394 total predicted MC events, 1345 of which are top events. Fig. 38(b) shows the same distribution, only this time for events containing an electron and muon pair. In this case, again at $E_T^{miss} > 66$ GeV, top is the dominant background; 1422 events are observed compared to a total of 1401 from all backgrounds, 1375 of which are top events.

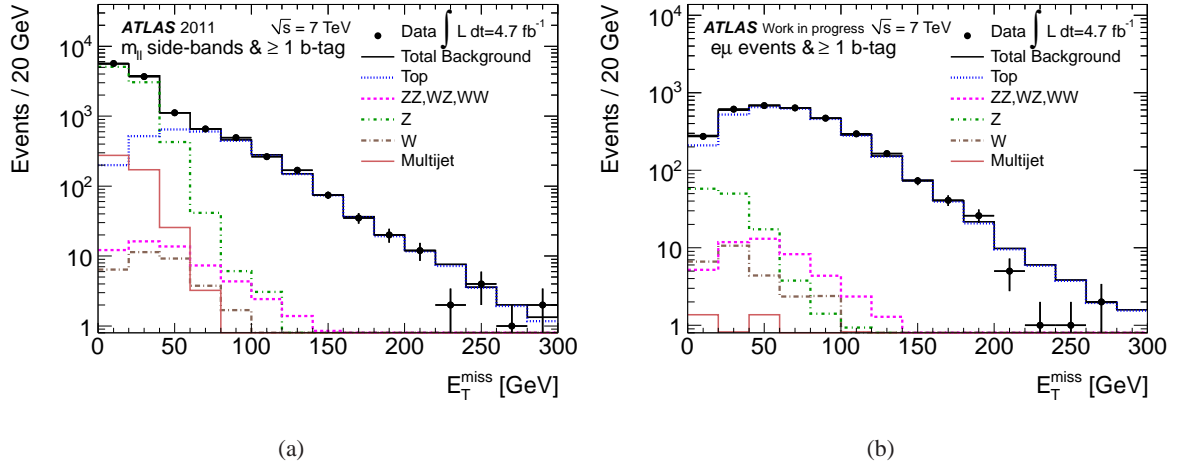


Figure 38: E_T^{miss} distribution for data and Monte Carlo estimated background samples for events in the sidebands of the m_{ll} distribution with b -jets in the ee and the $\mu\mu$ final states combined (a) and in the $e\mu$ (b) final state.

In order to measure the accuracy with which the MC simulates top and W events that do not contain a b -tagged jet one can look at events containing an oppositely charged electron-muon pair. Distributions of the invariant mass and the E_T^{miss} of these pairs can be seen in fig. 39, and in general good agreement between data and MC is observed. This is an important cross check to perform as it validates the simulation of the untagged top events. This sample is hence very similar to the sample selected by the nominal cuts in this search. One can obtain a purer top distribution by further requiring $E_T^{\text{miss}} > 66$ GeV. With this additional requirement a total of 2856 events are observed, compared to 2929 expected, 2595 of which are top events.

Another way to select a sample depleted of events with leptonic Z decays, is to require the leptons in the event to be of identical charge. This also significantly reduces the contribution from top events and provides a good way to partially isolate the $W + jets$ background. To further purify the $W + jets$ control region b -tagged events are rejected to reduce the contribution from top and it is required that the lepton pair is in the sidebands of the m_{ll} distribution, to reduce $Z + jets$ background.

Fig. 40 shows the E_T^{miss} distributions for like-sign ee and $e\mu$ pairs. For fig. 40 (a) the normalisation of the W background is taken directly from the simulation and it is clear that the simulated background overestimates the data. The contribution from the W background in this search is mainly from events with a misidentified electron, the rate of which is not described particularly well in the MC. Based on this observation the W background in this analysis is scaled down by 50% and a conservative 100% systematic is applied on the normalisation (see section 6.7). This background is not expected to contribute

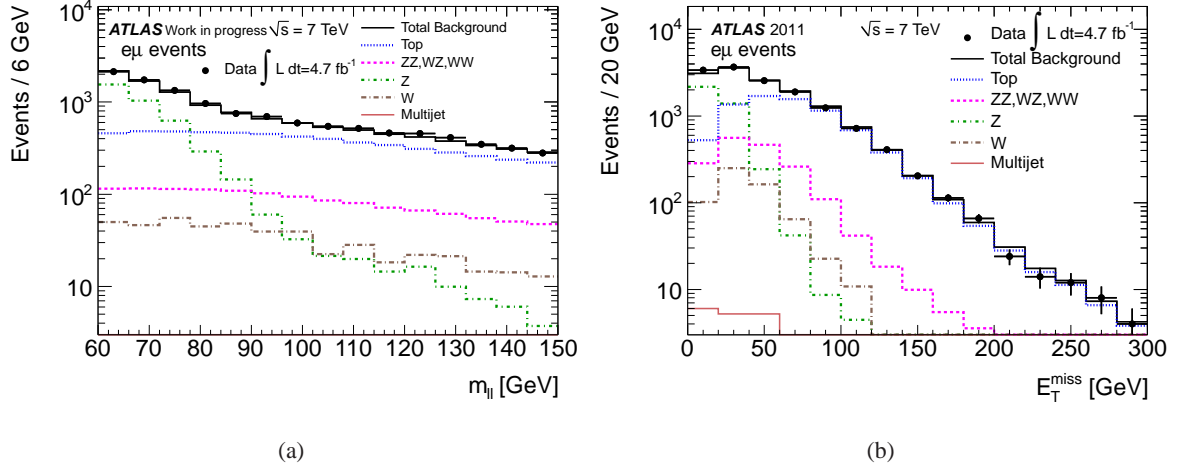


Figure 39: m_{ll} (a) and E_T^{miss} (b) for data and Monte Carlo events that contain an oppositely charged electron and muon. Note that in these plots the multiJet background is included from MC and not the data driven method described below.

significantly to the final distribution, so the large systematic has little effect on the overall limits.

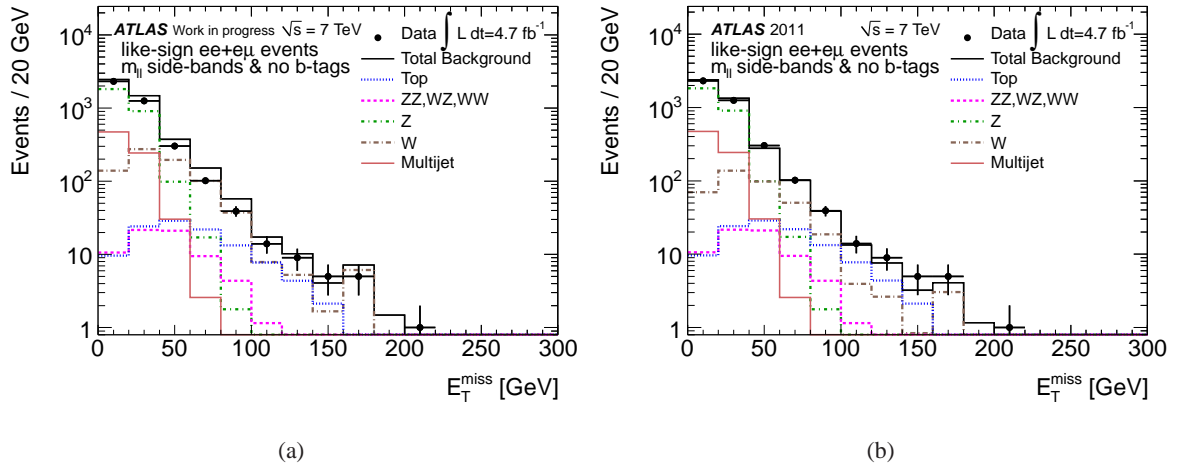


Figure 40: The E_T^{miss} distribution for data and Monte Carlo estimated background samples for events with a like-sign ee or $e\mu$ pair, no b -jets and a dilepton mass in the sidebands of the Z -mass region. In figure (a) the W background is unscaled, whilst in (b) the W background is scaled by the same factor 0.5 that is applied in all other figures.

The figure on the right shows the same distribution, but now with this 50% scaling applied to the W background. After this rescaling, for events with $E_T^{miss} > 66$ GeV, 124 events are observed in the data compared to 127 ± 8 expected events of which 61 ± 7 are W events.

6.6.3 WZ control regions

The $WZ \rightarrow lvll$ background contains a leptonic Z decay and genuine E_T^{miss} from the leptonic $W \rightarrow lv$ decay. It contributes to the signal region when the lepton from the W decay is missed. Therefore the p_T threshold for the veto leptons is lowered to 10 GeV to maximise the identification efficiency of this extra lepton and suppress the contribution from the WZ background. As a control region one can obtain a WZ dominated sample by selecting those events where an extra lepton has been identified. Fig. 41 shows the E_T^{miss} distribution for data and MC for events with an oppositely charged electron or muon pair and an additional lepton. In the high E_T^{miss} region the distributions are dominated by WZ background. For $E_T^{miss} > 66$ GeV, 100 events are observed compared to 77 expected events of which 70 are WZ events. The difference corresponds to 2 times the statistical uncertainty.

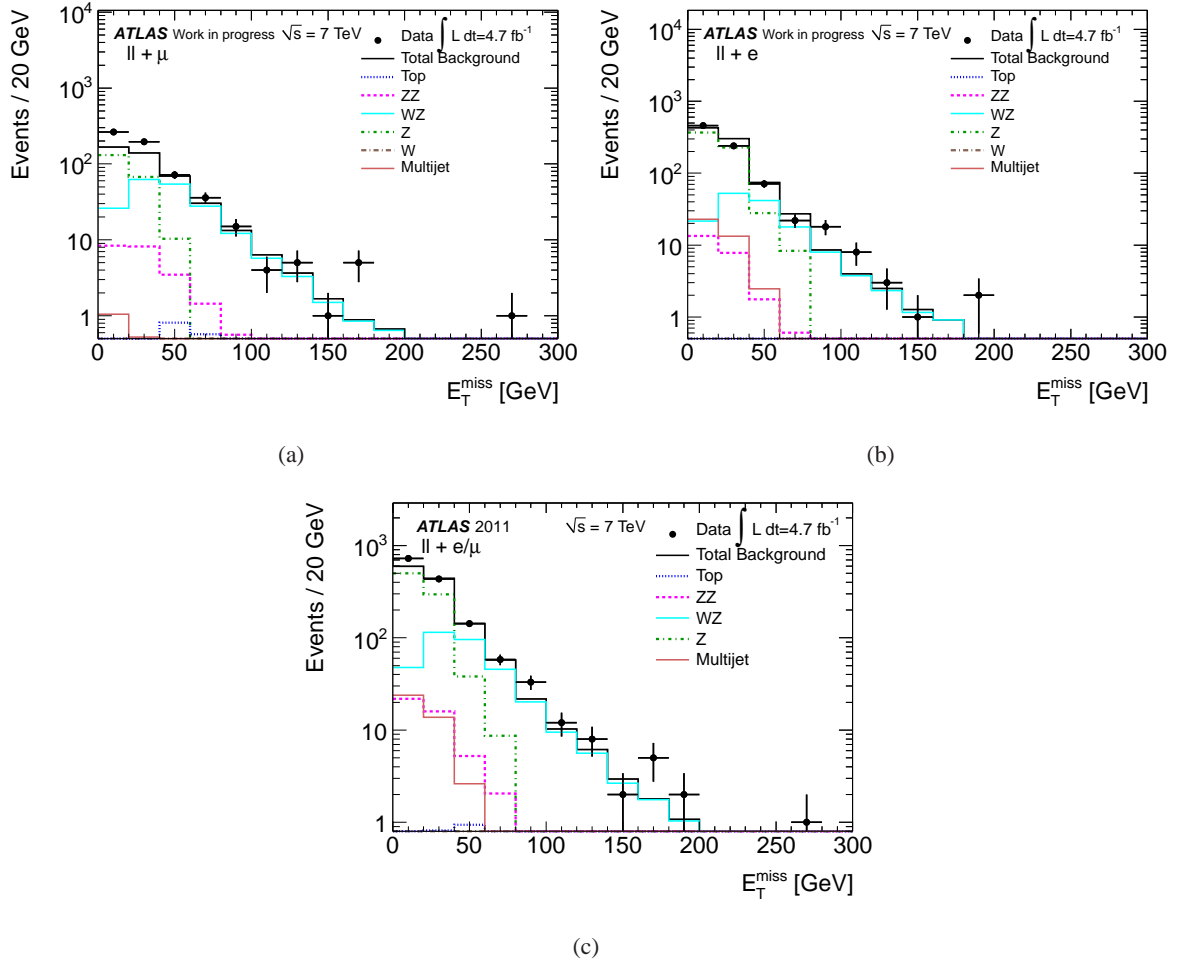


Figure 41: E_T^{miss} distribution for data and Monte Carlo events containing an oppositely charged electron or muon pair and an additional (a) muon, (b) electron or (c) either.

6.6.4 $Z + jets$ control regions

In the early data taking periods this background has a modest contribution at high E_T^{miss} in both the low and high mass search regions. In the later periods, in the presence of more pile-up interactions, the inclusive Z background is a leading background in the low mass search, while in the high mass region it has a similar contribution to the top background. This is because the additional interactions are significantly broadening the E_T^{miss} distribution, which can be seen in by comparing fig. 42(a) and fig. 42(b).

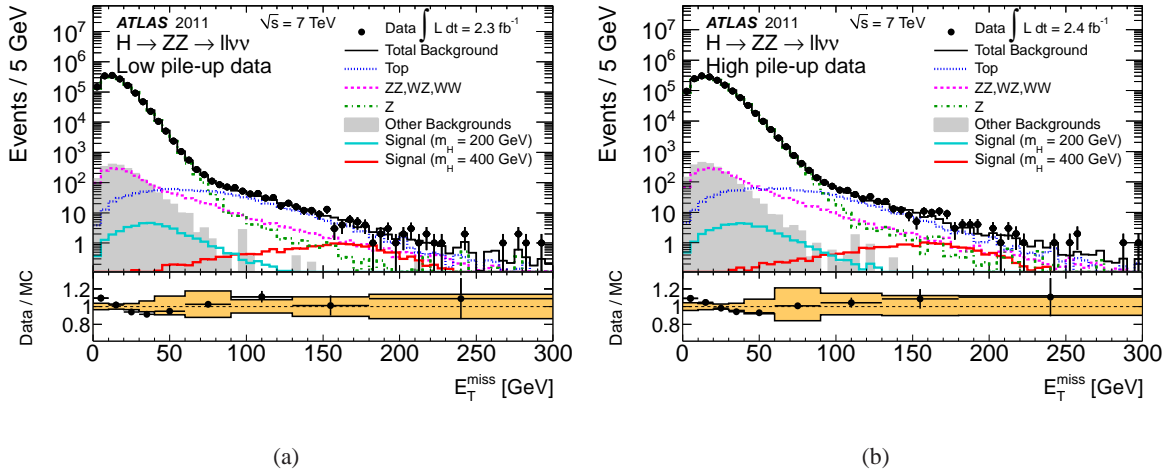


Figure 42: E_T^{miss} distributions for events with two leptons for the low pile-up (a) and high pile-up (b) periods. Contributions of muon and electron pairs are combined. The increased pile up in period L-M significantly broadens the contribution from backgrounds with fake E_T^{miss} particularly the inclusive Z sample.

As discussed in section 6.5, events with no genuine E_T^{miss} are strongly reduced by requiring large values of $\Delta\phi_{\vec{p}_T^{miss}, Jet}$. This discriminator can be inverted to obtain a control region for the inclusive Z background for events after the E_T^{miss} cut. As can be seen in fig. 43 events with fake E_T^{miss} pointing in the same direction as a high p_T jet are well described by the MC simulations within the statistical uncertainties. This figure further illustrates the increase of Z events in the high pileup periods compared to the low pileup periods.

In the low m_H search region, for $\Delta\phi_{\vec{p}_T^{miss}, Jet} < 1.5$, 114 (429) events are observed compared to 131 (431) expected events in the low (high) pile-up region. In the high m_H search region, for $\Delta\phi_{\vec{p}_T^{miss}, Jet} < 0.5$, 33 (73) events are observed compared to 34 (68) expected events in the low (high) pile-up region. In all cases the disagreement is smaller than the overall systematic applied on the Z background.

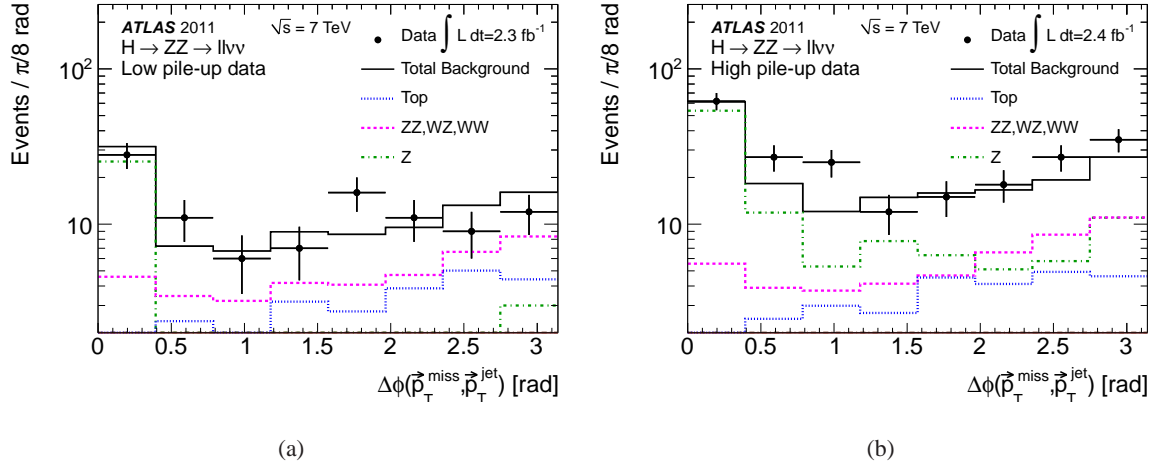


Figure 43: $\Delta\phi_{\vec{p}_T^{\text{miss}}, \vec{p}_T^{\text{jet}}}$ distributions for the high mass selection, for the low pile-up period (a) and the high pile-up period (b). Contributions of muon and electron pairs are combined.

6.6.5 Data-driven estimate of multijet production

QCD multijet production may contribute to the background if two fake leptons are reconstructed with an invariant mass consistent with a Z boson. Photon conversions also contribute in the case of electrons while pions decaying in-flight can add to the muon channel. In addition, true leptons from the semi-leptonic decay of heavy flavour hadrons may contribute in both the electron and muon channels.

Multijet background in the electron channel The multijet background in the electron channel is estimated from data using a template method. The shape of the background is determined from a sample dominated by multijets and then subsequently this sample is normalised to the nominal selection using the sidebands of the m_{ll} distribution. A data sample dominated by multijet events is obtained by replacing the standard requirement of two medium++ electrons in the analysis by two loose electrons which are explicitly required to not pass the medium++ selection (“LLnoM”). Since this sample contains loose electrons, rather than medium++, the events can no longer be collected using the standard (medium) single electron triggers described in section 6.4.2, as this might bias the selection. Instead, a trigger is used which is based on a signature of two loose photons, but also selects electron pairs, and is chosen since it is the lowest threshold unprecaled trigger available to trigger on loose electron pairs. The remaining analysis cuts are applied as usual and the resulting data histograms are used as templates to describe the shape of the multijet background in the various distributions.

Fig. 44 (top) shows the m_{ee} distributions of electron pairs in the data compared to the combined MC

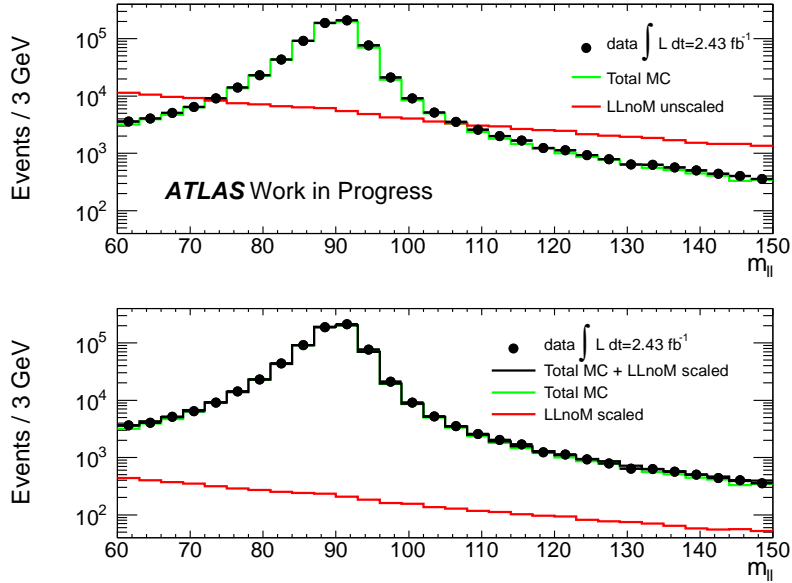


Figure 44: The m_{ll} distributions of the two electrons forming the leptonic Z candidate. The top plot shows the distribution in data, the distribution of all background Monte Carlo samples combined and, in red, the distribution in the “LLnoM” samples. In the bottom plot the data is compared against the sum of the combined Monte Carlo samples and the “LLnoM” sample scaled with the normalisation factor from the fit described in the text. The scaled “LLnoM” sample on its own is shown in red.

backgrounds, which, although not easily visible, fail to describe the tails away from the Z -resonance. Crucially the m_{ee} distribution of the “LLnoM” sample shows no evidence of a Z -resonance, indicating that it is dominated by fake electron pairs. Although the templates describe the shape of the multijet background, they must be normalised to take into account the difference in efficiency between the two electron selections. To estimate the normalisation of the fake electron pair background the m_{ee} distributions of the combined MC backgrounds and of the “LLnoM” sample are fitted to the data, allowing only the normalisations of the two to vary. The normalisation of the combined MC sample is unchanged within $\sim 1\%$. Fig. 44 (lower) shows the m_{ll} distribution in the data along with the MC backgrounds, the scaled “LLnoM” sample and the sum of the two. A good description over the entire range is obtained when the “LLnoM” estimate of the fake pairs is added to the combined Monte Carlo samples.

As the template sample used to estimate the QCD background in the electron channel is expected to have a different like-sign and opposite sign mixture than the electron pairs selected in the analysis, the template fit described above is repeated and a separate scaling factor is applied for like-sign events used in the $W + jets$ control region.

Multijet background in the muon channel The multijet background to the muon channel can be estimated in two ways. The background due to leptons originating from semi-leptonic heavy flavour decays is estimated directly from the semi-leptonic bb/cc samples described in section 6.2. Although the statistics for these background samples is about a factor 10 less than that in the data, no Monte Carlo events survive after the lepton pair selection.

In addition a selection of like-sign muon pairs is used to estimate the background of fake muons. 217 events with a like sign muon pair are identified (compared to 1.75×10^6 opposite sign pairs). The like sign pairs predominantly have low p_T muons and low E_T^{miss} . In the remainder of this search multijet background in the $H \rightarrow ZZ \rightarrow \mu\mu\nu\nu$ channel are considered to be negligible.

6.7 Systematic uncertainties

This section describes the systematic uncertainties taken into consideration for this search.

Luminosity The luminosity uncertainty used for the 2011 data is 3.7% for the low pile-up periods and 4.1% for the high pile-up periods. These numbers are based on recommendations from [84, 85]. This uncertainty is only applied to MC samples for which the normalisation error is not taken directly from a comparison between data and MC, which are the signal and diboson samples. When it is applied this systematic is assumed to be correlated across samples.

Signal cross section Higgs boson production cross section calculations have been summarised by the LHC Higgs cross section working group in [86]. There is an uncertainty in the production cross section arising from the choice of QCD scale, the Parton Distribution Functions (PDF) and α_s . For the QCD scale this uncertainty is ${}^{+12}_{-8}\%$ and $\pm 1\%$ for the gluon-gluon fusion and vector boson fusion processes respectively [86], and for the PDFs and α_s it is $\pm 8\%$ and $\pm 4\%$ for gluon-initiated and quark-initiated processes respectively. The cross sections are calculated with a zero-width approximation for the Higgs boson. For the Higgs decays the width is implemented at the event-generator level through a relativistic Breit-Wigner line shape. It has been suggested [87, 88] that for the highest Higgs boson masses considered in this search ($m_H > 400$ GeV) effects related to off-shell Higgs boson production and interference with other SM processes may become sizeable. For the gluon-fusion production mechanism at $m_H > 400$ GeV a lineshape correction is applied whereby the lineshape is reweighted to match a lineshape calculated in the complex pole estimation [88–90]. For the Vector Boson Fusion (VBF) production mechanism a full lineshape calculation and a correct account of the interference with SM ZZ production was not available. A conservative estimate of the possible size of such effects is included as a signal

systematic uncertainty on the normalisation of the signal for both production mechanisms, following a parametrisation as a function of m_H : $150\% \times m_H^3$ TeV, for $m_H \geq 300$ GeV [86].

Signal Acceptance To account for possible effects of theoretical uncertainties on the signal acceptance a systematic error is evaluated by comparing the selection efficiencies in the nominal $H \rightarrow ZZ \rightarrow ll\nu\nu$ MC signal samples (PowHegPythia, $m_H = 200, 400, 600$ GeV) with those obtained using samples where variations have been introduced at the generator level:

- **PowHegPythia:** For the nominal sample modelling Powheg interfaced with Pythia parton shower and ATLAS tune AUET2B-CTEQ6L1 [91] has been used.
- **ISR/FSR:** The parton shower effects were estimated by varying the parameters sensitive to the initial and final state radiation in the signal samples. The variation ranges were comparable to the ranges used in the Pythia tunes Perugia Hard and Perugia Soft [92]. Samples were produced with variations in the initial and final state radiation that either increased or decreased the parton shower activity with respect to the nominal sample.
- **Perugia2011:** The Powheg events were also processed with Pythia using the central Perugia2011 tune [92]. As is the case for the nominal sample ATLAS tune, the central Perugia2011 tune relies on the LHC data. The two tunes however differ in many aspects, as they are obtained from the independent tuning efforts.
- **SRenFacUp/Down:** In order to estimate the renormalisation and the factorisation scale systematics, two dedicated samples were generated where the Powheg renormalisation and factorisation scales have been set simultaneously to double or half their default values. The events for these samples were then processed with the same Pythia setup as for the nominal sample.

Table 19 summarises the effect of these theoretical uncertainties. They are calculated by taking the variation in absolute efficiency from the nominal sample, considering each step of the selection. To be conservative the largest error out of the up and down shifts is applied symmetrically. For the high Mass region ($m_H > 280$ GeV), the biggest variations between the 400 and 600 samples were taken. The total error is computed by adding the 3 individual errors in quadrature.

Background cross sections For the Z background a systematic variation is applied on the normalisation to account for discrepancies between the number of events predicted by MC and observed in the control regions and in the early parts of the selection process, when the Z background is dominant. MC

Region	ISR/FSR	Perugia2011	SRenFac	Total
Low-Mass	5.89%	5.50%	2.46%	8.43%
High-Mass	2.38%	1.38%	2.01%	3.41%

Table 19: Summary of the signal acceptance systematics.

predictions have on average about 2.4% fewer events than the data in the $H \rightarrow ZZ \rightarrow eev\nu$ channel and 1.2% fewer events than the data in the $H \rightarrow ZZ \rightarrow \mu\mu\nu\nu$ channel so a 2.5% systematic variation is applied. Since the normalisation has been verified by direct comparison between data and Monte Carlo no additional normalisation error due to the luminosity uncertainty is applied to this sample. All other systematics are applied to this sample since they are likely to affect both the shape and normalisation after the remaining selection cuts.

The largely irreducible SM ZZ background is taken directly from the Monte Carlo. A systematic error based on a 5% combined scale and PDF uncertainty for the NLO cross section is convoluted with a further 10% error, corresponding to the maximum difference seen in a comparison between the k-factor scaled PYTHIA and MC@NLO results (section 5.3.1), and applied. This leads to an overall 11% error on the normalisation.

The relatively small WZ and WW backgrounds are also taken directly from the Monte Carlo with an assumed normalisation error of 11%, identical to that taken for the ZZ background. This normalisation error covers the small discrepancies observed in the high E_T^{miss} tails of the WZ control region shown in fig. 41.

Comparisons between data and background expectations in the side-bands of the dilepton mass and in the $e\mu$ control region show discrepancies up to 5% in regions dominated by top background. This is well within the recommended 9% theory uncertainty which is applied on this background. Experimental uncertainties are still applied on this channel since the background is from top events failing the b -tagging veto, for which no direct control region comparison was made.

Comparisons between data and background expectations in the like-sign ee and $e\mu$ pair control regions indicate an overestimation of the W background in the MC. For this reason the W background is scaled down by 50%, and a 100% systematic is applied on the remaining W background. As the control region definition is very similar to the definition of the signal region, in particular involving a similar E_T^{miss} cut, no further systematics are applied in this case.

Electrons Systematic variations on efficiency, scale and smearing corrections for the electrons are applied to account for the uncertainties in the tag and probe method used to determine them [44]. These uncertainties arise from the uncertainties in the amount of additional material in the detector, the energy scale determination method, the object quality requirements, the background fit range and the pile up present in the sample used for the tag and probe study. The electron energy scale is varied up and down by 1% in the barrel region, and by 3% in the crack and end caps. Three alternate histograms are produced (one for smearing and one each for the energy scale shift up and down) which are generated with these shifts applied and used in the limit setting software described in section 6.9. Furthermore a 2.3% uncertainty is assumed on the combined identification and reconstruction efficiency of electrons. This is implemented as a 4.6% change, up and down, in the weighting for events with 2 electrons in the final state.

Muons Systematic variations on scale and smearing corrections are applied following the recommendations in [43, 93]. The uncertainty in the muon scale is p_T dependent, and for the range of muon momenta used in this analysis is of order 0.2%. The uncertainty in the smearing is also p_T dependent and separate uncertainties are used for the ID and MS tracks. A 1% uncertainty is assumed on the identification and reconstruction efficiency for muons determined from data and MC comparisons of J/Ψ and Z decays [43, 93]. This is implemented as a $\pm 1\%$ shift in the weighting of events with 2 muons in the final state.

Jets The energy scale and resolution uncertainties are applied as recommended in [48, 49] and [94] respectively. This includes scale and resolution uncertainties, a dedicated uncertainty in the case of nearby jets, an extra uncertainty due to pile-up and an extra uncertainty for b -jets.

b -tagging efficiency The uncertainty on the efficiency and mistag efficiency of the b -tagging algorithm used in this analysis follows the recommendations from [95].

Trigger No errors are applied for the lepton trigger efficiencies in the $H \rightarrow ZZ \rightarrow ee\nu\nu$ channel, since relative to the applied offline event selection the single electron trigger efficiencies in ATLAS are high. Therefore in events that have 2 electrons the event trigger efficiency is expected to be near 100% and the uncertainty is assumed to be negligible.

An uncertainty in the muon trigger weight is obtained from [43] which varies with p_T , η and ϕ . The muon trigger weight applied to each event containing either a muon or multiple muons is shifted up and

down by this uncertainty so that separate histograms can be obtained and used when setting limits, as described in section 6.9.

E_T^{miss} The systematic variation in E_T^{miss} is determined by propagating through all object scale and resolution uncertainties to the E_T^{miss} calculation. Since the E_T^{miss} is highly sensitive to pile-up an additional uncertainty on the average number of interactions per bunch crossing ($\langle \mu \rangle$) is applied. The μ values are rescaled in the MC by $\pm 3\%$, and the E_T^{miss} distribution with only these variations applied is shown in fig. 45.

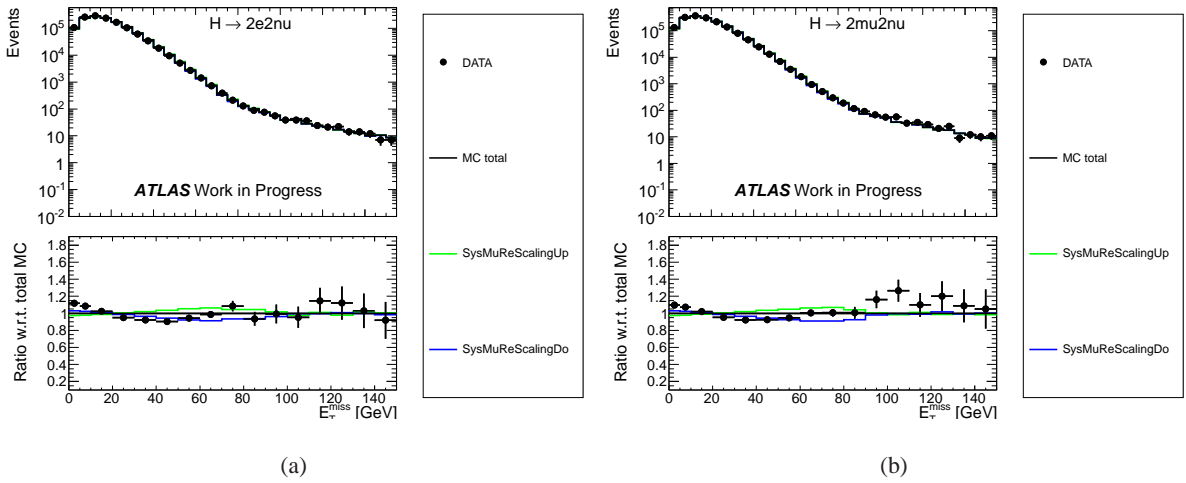


Figure 45: E_T^{miss} distribution for both channels with a $\pm 3\%$ μ re-scaling factor is also shown.

ZZ shape A shape systematic for the ZZ background is taken from the PYTHIA prediction for this background. Fig. 46 shows this comparison. To avoid adding an extra normalisation systematic, the final distribution, from the Pythia prediction is scaled to have the same number of events as that of the MC@NLO sample.

Z shape A shape systematic for the Z background is also taken from the PYTHIA prediction for this background. Again, to avoid adding an extra normalisation systematic, the final distribution, from the PYTHIA prediction is scaled to have the same number of events as that of the ALPGEN sample.

All of the above systematics are included in the plots showing systematic bands, which are made by adding each systematic in quadrature. In general all of the distributions important for this analysis agree within these systematic bands.

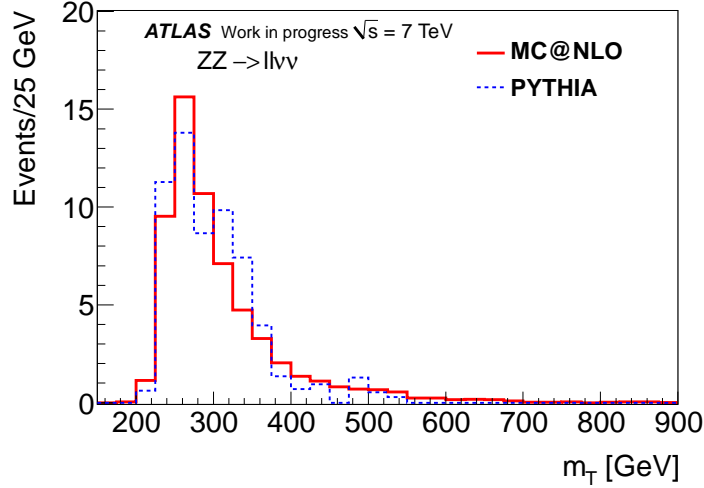


Figure 46: Comparison of the transverse mass distribution between the nominal MC@NLO ZZ background simulation and the alternative Pythia distribution, which is used as a systematic shape alternative. The electron and the muon channels are combined.

6.8 Results

This section presents the final transverse mass distributions after all cuts have been applied. As described in section 6.3 in this search some signal cross talk from other Higgs decay modes ($H \rightarrow ZZ \rightarrow ll\mu\mu$, $H \rightarrow ZZ \rightarrow llqq$ and $H \rightarrow WW \rightarrow l\nu l\nu$) is expected. These processes add to the expected sensitivity and are therefore considered as part of the signal. Table 20 shows the relative contributions from the different Higgs decay modes in the final selected MC signal samples in the $H \rightarrow ZZ \rightarrow ll\nu\nu$ channel. In particular the $H \rightarrow WW \rightarrow l\nu l\nu$ admixture is large at the lowest Higgs masses. To avoid double counting with the ATLAS $H \rightarrow WW \rightarrow l\nu l\nu$ analysis an explicit veto is applied in the latter search to events in which the selected lepton pair consists of same flavour leptons and has a mass consistent with having originating from a Z-decay, based on the same mass window cut as that applied in this analysis. Similarly the $H \rightarrow ZZ \rightarrow ll\nu\nu$ and the $H \rightarrow ZZ \rightarrow llqq$ channels have no overlap because of the different E_T^{miss} regions selected. The $H \rightarrow ZZ \rightarrow ll\nu\nu$ selection also excludes events with more than two leptons, so no overlap is expected between this channel and the $H \rightarrow ZZ \rightarrow ll\mu\mu$ channel. In all results plots shown in this section, as well as in the limits shown in section 6.9, events from other Higgs decay modes are included and considered as part of the signal.

The distributions of the transverse mass of the $ll + E_T^{miss}$ system are shown in fig. 49 for $m_H = 200, 300, 400, 500$ and 600 GeV. At 200 GeV the distribution is clearly dominated by the background processes. A better separation between the signal and backgrounds is obtained at the higher

$m_H(\text{GeV})$	$H \rightarrow ZZ \rightarrow ll\nu\nu$	$H \rightarrow ZZ \rightarrow llll$	$H \rightarrow ZZ \rightarrow llqq$	$H \rightarrow WW \rightarrow l\nu l\nu$
200	25.5%	0.4%	0.0%	74.1%
300	87.0%	0.8%	0.0%	12.2%
400	94.5%	1.0%	0.0%	4.5%
500	96.9%	0.9%	0.0%	2.2%
600	97.4%	0.8%	0.0%	1.8%

Table 20: The number of events from different Higgs decay modes relative to the total number of signal events, after the full $H \rightarrow ZZ \rightarrow ll\nu\nu$ selection. In all signal samples τ leptons are included.

masses. It can also be seen that the transverse mass distribution for the signal peaks near the Higgs mass. The distribution of data events observed is also shown on the plots. The total number of events, after all cuts, for each of the Higgs mass samples as well as the backgrounds are given in tables 21 . From this table it can be seen that for the high mass searches the diboson backgrounds dominate, particularly in the low pile up data, and that for the most sensitive mass range, $m_H = 300$ to 400 GeV, the signal to background ratio is higher in the low pile up data.

Source	low m_H search		high m_H search	
	Low pile-up data	High pile-up data	Low pile-up data	High pile-up data
Z	$40.1 \pm 5.0 \pm 7.9$	$264.7 \pm 12.7 \pm 67.3$	$0.8 \pm 0.3 \pm 0.8$	$11.6 \pm 2.1 \pm 2.9$
W	$4.6 \pm 2.2 \pm 4.6$	$5.8 \pm 1.8 \pm 5.8$	$1.5 \pm 0.8 \pm 1.5$	$2.2 \pm 1.3 \pm 2.2$
top	$23.2 \pm 1.3 \pm 5.4$	$27.9 \pm 1.3 \pm 5.3$	$16.0 \pm 1.1 \pm 4.0$	$17.2 \pm 1.0 \pm 3.9$
multijet	$1.1 \pm 0.2 \pm 0.5$	$1.1 \pm 0.2 \pm 0.6$	$0.1 \pm 0.1 \pm 0.0$	$0.1 \pm 0.1 \pm 0.0$
ZZ	$33.4 \pm 0.7 \pm 3.9$	$36.7 \pm 0.7 \pm 4.3$	$28.4 \pm 0.6 \pm 3.4$	$31.9 \pm 0.7 \pm 3.8$
WZ	$23.3 \pm 1.0 \pm 2.8$	$25.2 \pm 1.0 \pm 3.0$	$17.1 \pm 0.8 \pm 2.1$	$18.9 \pm 0.8 \pm 2.3$
WW	$25.5 \pm 0.8 \pm 3.0$	$32.4 \pm 0.9 \pm 3.8$	$9.4 \pm 0.5 \pm 1.1$	$13.3 \pm 0.5 \pm 1.6$
Total	$151.2 \pm 5.8 \pm 11.2$	$394.0 \pm 13.0 \pm 66.9$	$73.3 \pm 1.8 \pm 6.1$	$95.2 \pm 2.9 \pm 6.9$
Data	158	442	77	109
m_H [GeV]	Signal expectation			
200	$10.3 \pm 0.2 \pm 1.8$	$11.1 \pm 0.2 \pm 1.9$		
300			$16.4 \pm 0.3 \pm 2.9$	$17.5 \pm 0.3 \pm 3.1$
400			$14.4 \pm 0.2 \pm 2.5$	$15.4 \pm 0.2 \pm 2.7$
500			$6.2 \pm 0.1 \pm 1.1$	$6.5 \pm 0.1 \pm 1.1$
600			$2.7 \pm 0.0 \pm 0.5$	$2.9 \pm 0.0 \pm 0.5$

Table 21: The expected number of background and signal events in the low and high m_H search regions in the $H \rightarrow ZZ \rightarrow ll\nu\nu$ channel, along with the observed numbers of candidates in data, for an integrated luminosity of 2.05 fb^{-1} . The quoted uncertainties are statistical and systematic respectively.

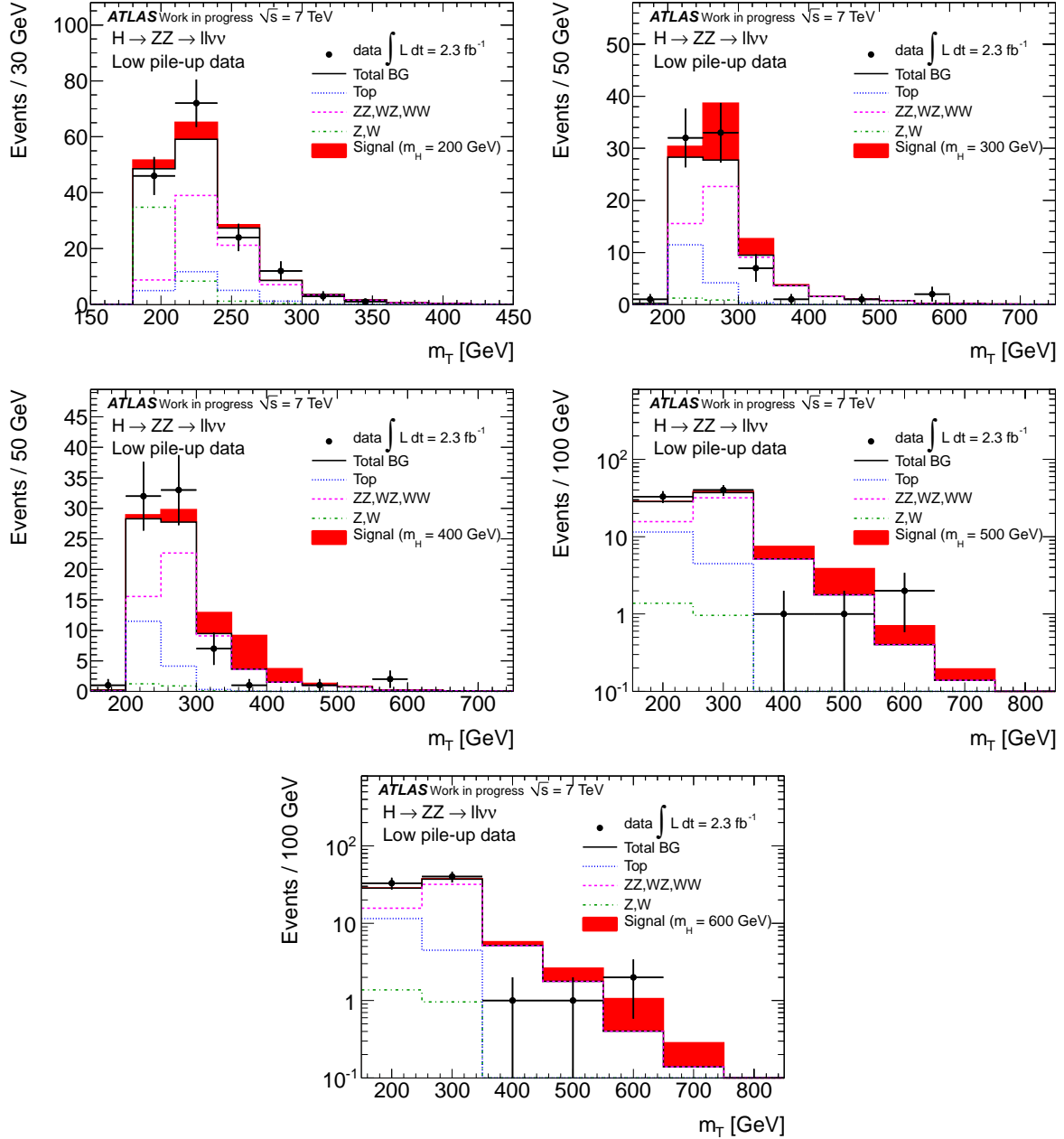


Figure 47: The final transverse mass distribution in the $H \rightarrow ZZ \rightarrow ll\nu\nu$ channel as defined in Equation 53 for the Higgs masses $m_H = 200, 300, 400, 500$ and 600 GeV for low pile-up data.

6.9 Exclusion limits

As there is no significant excess seen in the data above background expectations in all studied decay channels it is possible to place limits on the range of possible values of m_H . The nominal limits are extracted using a fully frequentist profile likelihood treatment described in [96] and implemented in

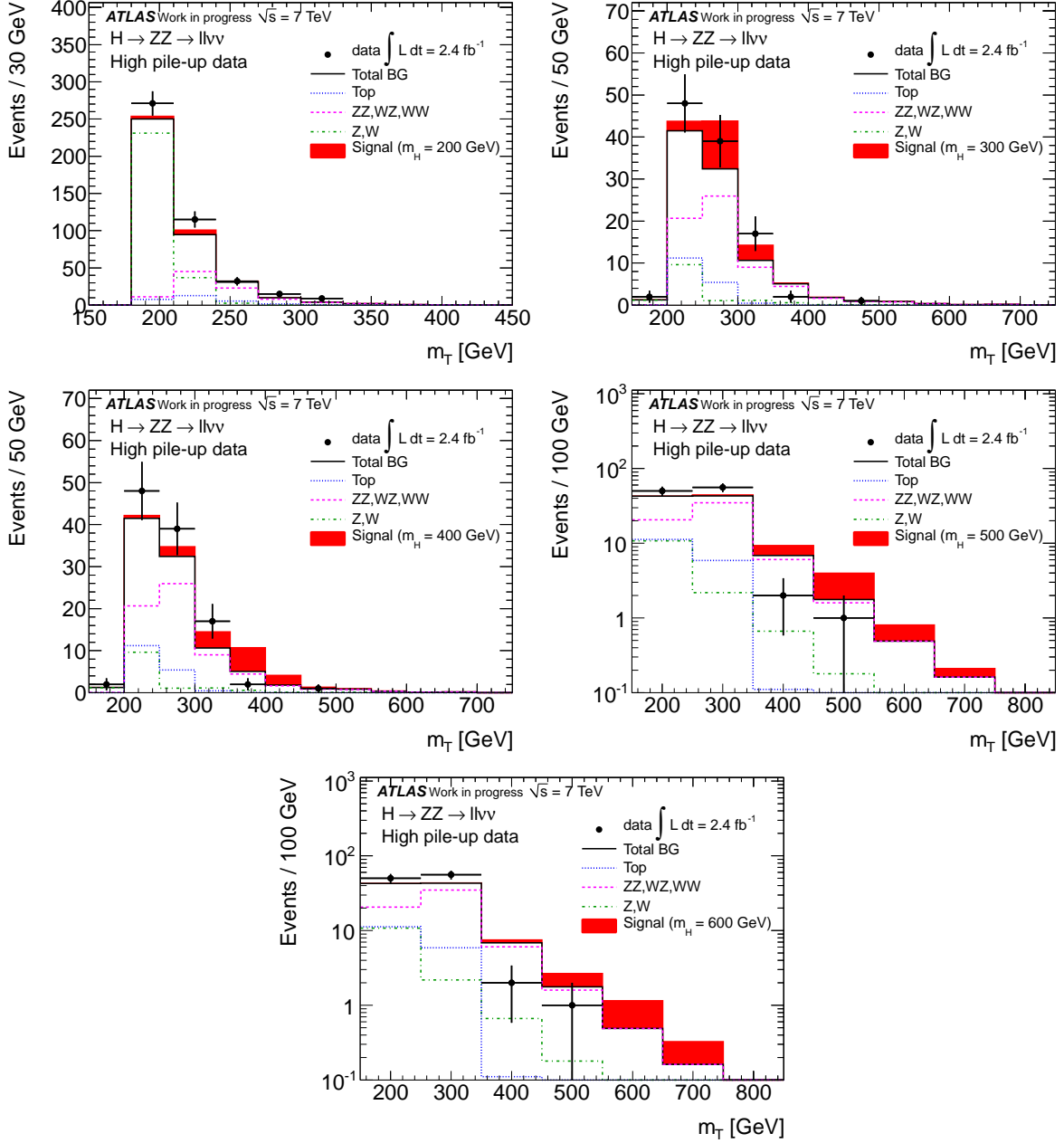


Figure 48: The final transverse mass distribution in the $H \rightarrow ZZ \rightarrow ll\nu\nu$ channel as defined in Equation 53 for the Higgs masses $m_H = 200, 300, 400, 500$ and 600 GeV for high pile-up data.

the RooStats package [97]. The limits are based on the CL_s method introduced in section 5.7. A log likelihood ratio is used as the test statistic, which corresponds to $2 \times \ln(X)$, where X was defined in equation 51. The expected and observed limits are determined by running a simultaneous confidence level determination in which the distributions from the $H \rightarrow ZZ \rightarrow ee\nu\nu$ and $H \rightarrow ZZ \rightarrow \mu\mu\nu\nu$ channels are treated independently. Due to the different signal to background ratio in the high and low pile-up

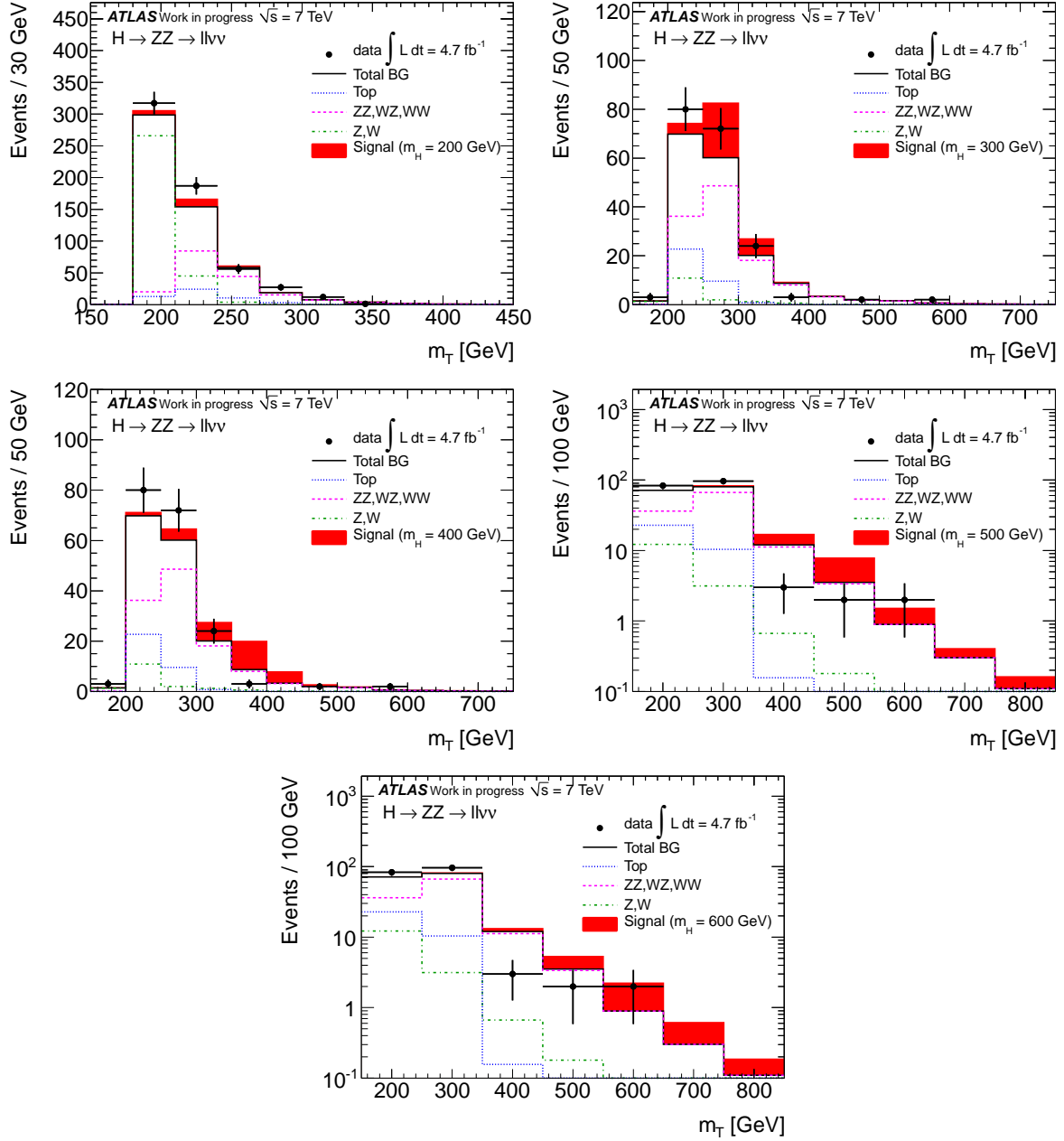


Figure 49: The final transverse mass distribution in the $H \rightarrow ZZ \rightarrow ll\nu\nu$ channel as defined in Equation 53 for the Higgs masses $m_H = 200, 300, 400, 500$ and 600 GeV for the full 2011 dataset.

regions the limits are determined separately for each region, and then combined.

Upper limits are set on the Higgs boson production cross section relative to its predicted SM value as a function of m_H . The limits are extracted from a maximum likelihood fit to the m_T distribution following the CL_s modified frequentist formalism with the profile likelihood test statistic [68, 96]. Table 22 lists all systematic uncertainties that are taken into account in the limit setting software and whether they

are implemented via an alternative histogram or as a normalisation uncertainty. For practical purposes systematics that were found to have a negligible effect on the final limit are not included in the final limit calculation.

Systematic	ggF sig.		VBF sig.		ZZ		WZ/WW		$t\bar{t}$		Z		W		QCD	
	ee	$\mu\mu$	ee	$\mu\mu$	ee	$\mu\mu$	ee	$\mu\mu$	ee	$\mu\mu$	ee	$\mu\mu$	ee	$\mu\mu$	ee	$\mu\mu$
e eff.	norm	no	norm	no	norm	no	norm	no	no	no	no	no	no	no	no	no
e scale	yes	no	yes	no	yes	no	yes	no	yes	no	yes	no	no	no	no	no
e smear	yes	no	yes	no	yes	no	yes	no	yes	no	yes	no	no	no	no	no
μ eff.	no	norm	no	norm	no	norm	no	norm	no	no	no	no	no	no	no	no
μ ID smear	no	yes	no	yes	no	yes	no	yes	no	yes	no	yes	no	no	no	no
μ MS smear	no	yes	no	yes	no	yes	no	yes	no	yes	no	yes	no	no	no	no
b/c -tag eff.	norm.		norm.		norm.		norm.		norm.		norm.		no		no	
light-tag eff.	norm.		norm.		norm.		norm.		norm.		norm.		no		no	
jet scale	yes		yes		yes		yes		yes		yes		no		no	
jet smear	yes		yes		yes		yes		yes		yes		no		no	
shape alt. MC	no		no		no		no		no		shape		no		no	
P_T^H reweight	norm.		no		no		no		no		no		no		no	
Accep. MC model	norm.		no		no		no		no		no		no		no	
PDF	norm.		norm.		norm.		norm.		no		no		no		no	
QCD scale	norm.		norm.		norm.		norm.		no		no		no		no	
Add correction	no		no		norm.		norm.		no		no		no		no	
CR correction	no		no		no		no		norm.		norm.		norm.		norm.	
luminosity	norm.		norm.		norm.		norm.		no		no		no		no	

Table 22: Systematic variations applied in the confidence level fits in the $H \rightarrow ZZ \rightarrow ll\nu\nu$ channel. Yes and no refer to whether or not a shape systematic is used and norm means this uncertainty only impacts normalisation.

The limit setting method differs from the mclimit method presented in section 5.7 in the determination of the log likelihood ratio distributions from the $s + b$ and b hypotheses. In mclimit many toy MC experiments are generated and the log likelihood distribution of each toy experiment is used to form these 2 distributions. This is computationally very expensive. Here, the form of the log likelihood distributions are approximated by asymptotic distributions for the signal plus background and the background only case [96], so that the generation of many MC toy experiments is not required.

The systematic variations are taken into account by allowing the values of the nuisance parameters to shift within their uncertainties with respect to one another such that they maximise the likelihood of the given hypothesis. This is done separately for the signal and signal plus background hypotheses [68]. The systematic variations thus broaden the likelihood distribution given in equation 51.

Fig. 50 shows the expected and observed limits at the 95% confidence level. Fluctuations in the

background can lead to better or worse observed limits and the green and yellow bands indicate the expected sensitivity corresponding to $\pm 1\sigma$ and $\pm 2\sigma$ statistical fluctuations in the data respectively.

A range between 260 and 520 GeV is expected to be excluded while observation shows that a SM Higgs is excluded at the 95% confidence level in the range of 320 and 560 GeV.

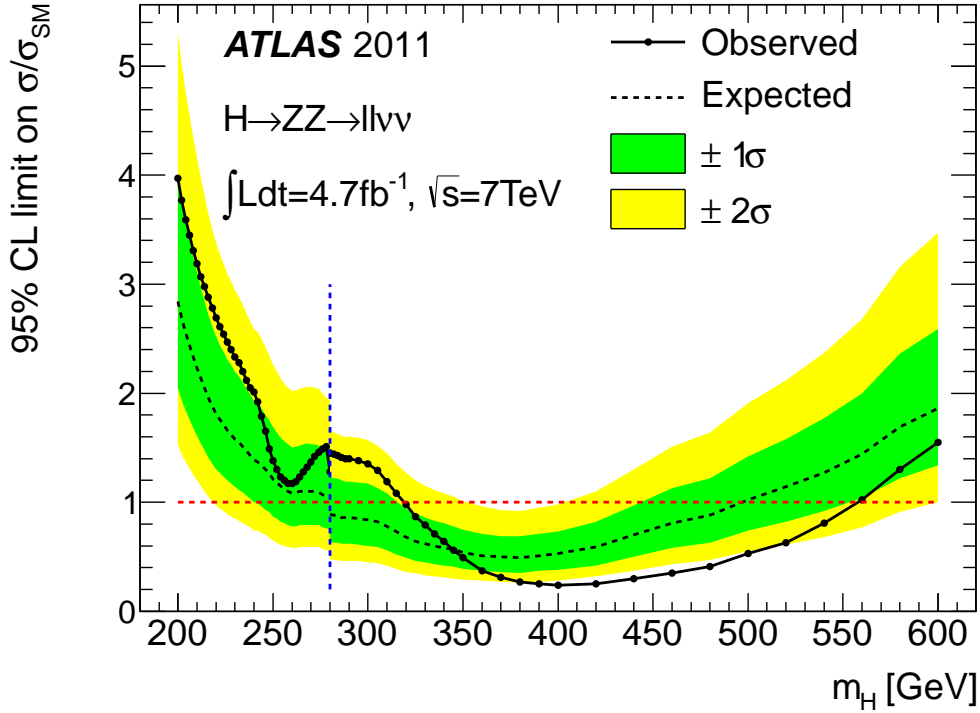


Figure 50: Expected and observed limits for the $H \rightarrow ZZ \rightarrow ll\nu\nu$ channel, expressed as the number of times the Standard Model Higgs cross section that would be excluded at 95% confidence level based on a frequentist Profile Likelihood CLs formalism. The green and yellow bands indicate the expected sensitivity with $\pm 1\sigma$ and $\pm 2\sigma$ fluctuations respectively. The limits correspond to 2.05 fb^{-1} of data at $\sqrt{s} = 7 \text{ TeV}$.

6.10 Conclusion

The search for the SM Higgs boson in the $H \rightarrow ZZ \rightarrow ll\nu\nu$ channel with 4.7 fb^{-1} of data is presented above. This channel alone excludes a Higgs boson with a mass in the range between 320 and 560 GeV. The exclusion limits for the combination of all of the channels used in ATLAS for the search for the SM Higgs boson are shown in fig. 51. It can be seen that for $m_H > 350 \text{ GeV}$ the $H \rightarrow ZZ \rightarrow ll\nu\nu$ channel has the strongest observed exclusion, and dominates entirely at the very high masses.

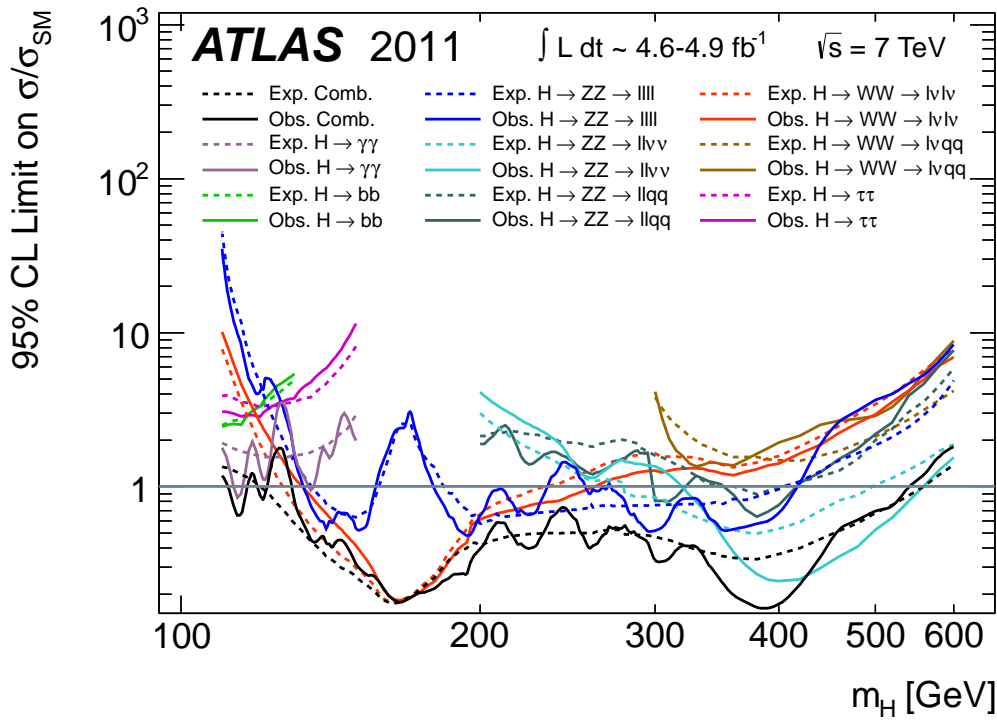


Figure 51: Expected and observed limits for the all of the channels in the ATLAS SM Higgs search expressed as the number of times the Standard Model Higgs cross section that would be excluded at 95% confidence level based on a frequentist Profile Likelihood CLs formalism. The limits correspond to $4.7 - 4.9 \text{ fb}^{-1}$ of data at $\sqrt{s} = 7 \text{ TeV}$ [98].

Chapter 7

Search for the invisible decay of the Higgs boson using the $ZH \rightarrow ll + inv$ channel

This chapter describes the search for anomalous invisible decays of the Higgs boson using the $ZH \rightarrow ll + inv$ channel. This search was adapted from the $H \rightarrow ZZ \rightarrow ll\nu\nu$ search presented in chapter 6, and was conducted using the 7 TeV 2011 and 8 TeV 2012 datasets. It should be noted that only the first 13 fb^{-1} of 2012 data is presented in this search, which when combined with the 4.7 fb^{-1} from 2011 gives a total of integrated luminosity of 17.7 fb^{-1} . The data and MC samples used for the 2011 search were described in chapter 6, the details given in this section are for the 2012 dataset.

Throughout this section the decay of a Higgs to "invisible" particles is discussed. This terminology refers to any particles which are not directly detected by the ATLAS detector, but are inferred from the presence of E_T^{miss} .

7.1 Discovery of a new boson

During the summer of 2012 it was announced that both CMS and ATLAS observe excesses in the final state invariant mass distributions for the $H \rightarrow ZZ \rightarrow llll$ and $H \rightarrow \gamma\gamma$ channels consistent with a SM Higgs boson of mass $m_H = 125 \text{ GeV}$ [99, 100]. Broad excesses were also observed in the $H \rightarrow WW$ channels in both experiments consistent with a Higgs at this mass. Each experiment quoted a confidence level of greater than 5σ , the required level for the discovery of a new particle. The analysis presented in chapter 6 was used in the combination of all the search channels for the Higgs boson in ATLAS. Since then the significance of results from both experiments has increased and couplings and properties of the candidate boson, measured so far, are in good agreement of those expected for a SM Higgs.

7.2 Introduction of the $ZH \rightarrow ll + inv$ decay channel

The SM Higgs boson is predicted to have a negligible branching fraction to an invisible final state. The only contribution from the SM is from the $H \rightarrow ZZ \rightarrow \nu\nu\nu\nu$ channel, which has a branching ratio of 5.3×10^{-3} [101] which for $m_H = 125 \text{ GeV}$ gives a total cross section of 2.96 fb at $\sqrt{s} = 8 \text{ TeV}$. Any excess observed consistent with an invisibly decaying Higgs boson could be an indication of a BSM process.

Results obtained in the $H \rightarrow ZZ \rightarrow ll ll$, $H \rightarrow \gamma\gamma$, $H \rightarrow WW$, $H \rightarrow \tau\tau$ and $V(H \rightarrow bb)$ using the 2011 dataset together with 20.7 fb^{-1} from 2012 on the Higgs boson candidate at $m_H = 125 \text{ GeV}$ do not exclude the possibility of a sizeable branching fraction to invisible particles. The search presented in the following chapter aims to set direct limits on the invisibly decaying branching fraction of the Higgs boson candidate. In addition, the analysis also searches for invisible decays of further Higgs-like particles at masses $m_H > 115 \text{ GeV}$. Prior to this search, the strongest exclusion limit on a Higgs-like particle decaying completely to invisible particles in association with a Z boson was $m_H > 114.1 \text{ GeV}$. This result was obtained from a direct search in the ZH channel at LEP [102], where a SM ZH production cross section and a $H \rightarrow inv$ branching ratio of 100% were assumed.

7.3 Models involving an invisibly decaying Higgs

There are a number of BSM physics models that have a $H \rightarrow inv$ decay signature. For example, a pair of heavy, fourth generation neutrinos would couple to the Higgs boson if the neutrino mass were less than $m_H/2$. The current mass limits on such a neutrino (ν') are $M_{\nu'} > M_Z/2$, a result obtained at LEP [103]. If the mass of the fourth generation neutrino was $M_Z/2 < M_{\nu'} < M_H/2$ one would expect a high branching ratio for $H \rightarrow \nu'\nu'$.

Possible Dark Matter (DM) candidates at the GeV - TeV scale are discussed in [21] and in section 2.5. In order to solve the hierarchy problem the DM candidate must couple to the Higgs boson, and thus would have to be weakly interacting. They also must be stable, and thus not detected by the ATLAS detector. Invisible decays of the Higgs boson would therefore indicate a possible DM candidate. Super symmetry (SUSY) requires 5 Higgs bosons, h , H , A , H^+ and H^- . SUSY provides a natural framework for DM to enter into the SM as the lightest super symmetric particle is a natural candidate for DM. As such an invisibly decaying Higgs would strongly motivate SUSY searches, as well as constraining others.

7.4 Production mechanism and signature

In the $ZH \rightarrow ll + inv$ decay channel the invisibly decaying Higgs boson is produced in association with a leptonically decaying Z boson. The Feynman diagram of the production mechanism for this process is given in fig. 3(c). The search is conducted for the case where the Z boson decays to either electrons or muons. For the search, it is assumed that the ZH production mechanism is that predicted for a SM Higgs.

The kinematics of the final state are similar to those from the $H \rightarrow ZZ \rightarrow ll\nu\nu$ decay described in chapter 6. To distinguish the signal from background this analysis focuses on events with high E_T^{miss} . For signal events the E_T^{miss} is from the invisibly decaying particles, and will be in the opposite direction

to the leptons from the Z decay. The Z boson produced in this process is selected to be highly boosted, and therefore the opening angle between the leptons will be small in the rest frame of the detector.

7.5 The 2012 dataset

In February 2012, after the winter shutdown, the LHC began colliding protons with an increased centre-of-mass energy of $\sqrt{s} = 8$ TeV. A total of 23 fb^{-1} of data were recorded by ATLAS at this energy, the first 13 fb^{-1} of which are used for the $ZH \rightarrow ll + inv$ search presented here. The data are required to pass a Good Runs List that ensures all essential elements of the ATLAS detector were operational with good efficiency during data taking. This is crucial to ensure reliable E_T^{miss} performance.

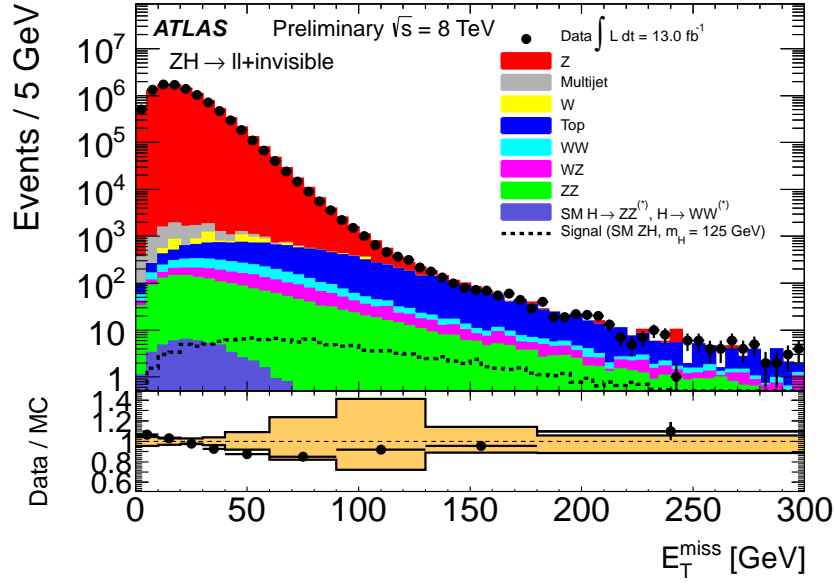
7.6 Event selection

The event selection for the $H \rightarrow ZZ \rightarrow ll\nu\nu$ search was taken as the starting point for this search. To ensure that no bias was introduced the optimisation of the selection cuts was performed on MC. In addition the event selection in the 2012 analysis was blinded, so that the signal region with $E_T^{miss} > 80$ GeV could not be seen until the cuts were frozen. The 2011 dataset was not blinded because the signal region had already been investigated extensively in the $H \rightarrow ZZ \rightarrow ll\nu\nu$ analysis. The optimisation procedure varied the cuts on several variables to maximise the sensitivity defined as $\sqrt{2((S+B)\ln[1+\frac{S}{B}]-S)}$ [96].

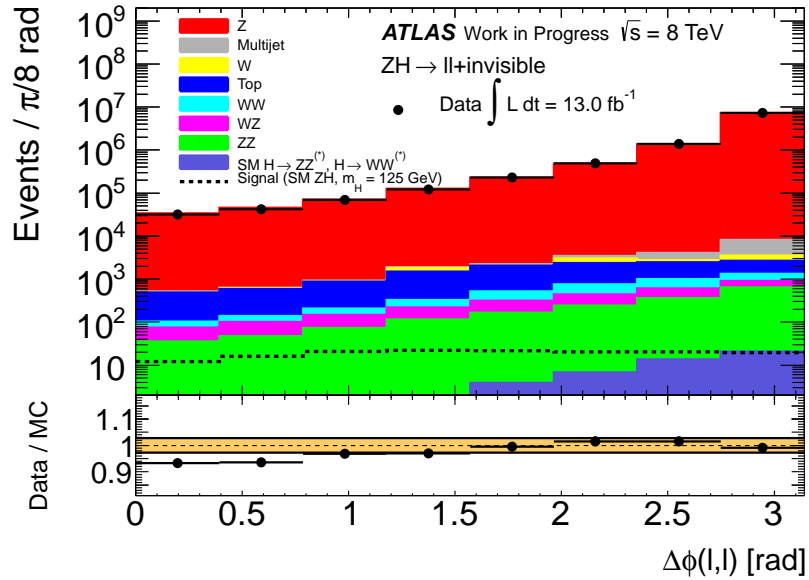
The p_T threshold of the triggers increased with respect to the $H \rightarrow ZZ \rightarrow ll\nu\nu$ analysis. For the electron channel a logical OR is performed between 3 triggers; a single electron trigger which requires an isolated medium++ electron with $p_T \geq 24$ GeV, a di-electron trigger which require 2 isolated loose++ electrons with $p_T \geq 12$ GeV and a further single electron trigger with a p_T threshold at 60 GeV with no isolation requirement. For the muon channel a logical OR is again performed between 3 triggers; two single muon trigger with p_T thresholds at 24 and 36 GeV and a di-muon trigger that requires 2 muons with $p_T \geq 13$ GeV. The trigger efficiency of signal events passing the full selection described below is nearly 100% for the electron channel, and is approximately 94% for the muon channel.

Candidate $ZH \rightarrow ll + inv$ events are selected by first applying the preselection cuts described in section 6.5, with the following modifications:

- To increase the rejection of the WZ background the selection requirements on the third lepton veto were loosened; The momentum threshold for both electrons and muons was lowered to $p_T > 7$ GeV and the identification requirement on electrons was loosened to loose++.
- To aid the separation between signal events and backgrounds that don't contain genuine E_T^{miss} it is required that the invisibly decaying Higgs boson has a significant boost, thus giving rise to a large



(a)



(b)

Figure 52: Kinematic distributions relevant to $ZH \rightarrow ll + inv$ analysis for the Higgs boson signal and the main backgrounds: (a) the E_T^{miss} (b) the opening angle of the two leptons. The bottom plot shows the ratio between data and the combined MC background samples as well as a band formed by adding in quadrature all systematic uncertainties. Both plots are shown after the m_{ll} window has been applied and for the 2012 dataset.

missing transverse energy. For this reason the missing transverse energy is required to exceed 90 GeV. The E_T^{miss} is calculated as described in section 4.6. The distribution of the E_T^{miss} after

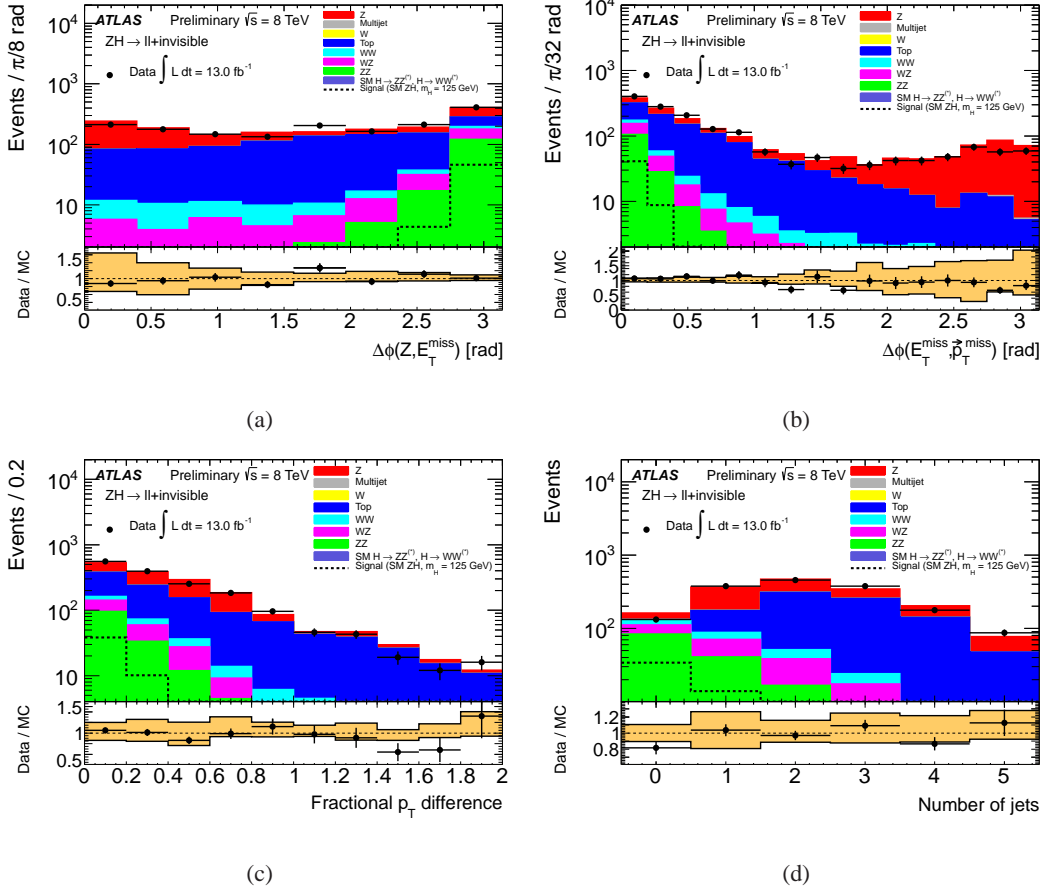


Figure 53: Kinematic distributions relevant to $ZH \rightarrow ll + inv$ analysis for the Higgs boson signal and the main backgrounds: (a) the angle between the Z candidate and the \vec{p}_T^{miss} (b) the opening angle between the \vec{p}_T^{miss} and the track-based E_T^{miss} (c) the fractional difference between the E_T^{miss} and the transverse momentum of the lepton pair and (d) the number of jets in the event, The signal sample shown corresponds to a Higgs with $m_H = 125$ GeV. The bottom plot shows the ratio between data and the combined MC background samples as well as a band formed by adding in quadrature all systematic uncertainties. All plots are shown after the E_T^{miss} cut has been applied and for the 2012 dataset.

the lepton mass window cut is shown in fig. 52(a) for a combination of the $ZH \rightarrow ee + inv$ and $ZH \rightarrow \mu\mu + inv$ channels.

- In signal events the Z bosons are expected to be more boosted than in some of the background processes. Therefore an upper limit is applied to the azimuthal angle between the two leptons, $\Delta\phi_{ll} < 1.7$. The distribution of $\Delta\phi_{ll}$, after the dilepton mass window cut, is shown in fig. 52(b) for a combination of the $ZH \rightarrow ee + inv$ and $ZH \rightarrow \mu\mu + inv$ channels.
- In the signal the E_T^{miss} is expected to be back-to-back with the Z candidate. An additional cut is

therefore applied on the azimuthal angle between the Z candidate and the \vec{p}_T^{miss} , $\Delta\phi_{Z,\vec{p}_T^{miss}} > 2.6$. The distribution of $\Delta\phi_{Z,\vec{p}_T^{miss}}$, after the E_T^{miss} cut, is shown in fig. 53(a) for a combination of the $ZH \rightarrow ee + inv$ and $ZH \rightarrow \mu\mu + inv$ channels.

- Apart from the standard E_T^{miss} , one can also estimate the missing transverse energy using tracks from the primary vertex. As this variable is based on tracks from the primary vertex only, it is expected to be relatively robust against pile-up effects. A disagreement between the direction of the track based missing p_T vector and the standard \vec{p}_T^{miss} vector can indicate that the latter was poorly measured. A cut is therefore applied on the azimuthal angle between these two vectors, $\Delta\phi(\vec{p}_T^{miss}, p_T^{miss,track}) < 0.2$. The distribution of $\Delta\phi(E_T^{miss}, p_T^{miss,track})$, after the E_T^{miss} cut, is shown in fig. 53(b) for a combination of the $ZH \rightarrow ee + inv$ and $ZH \rightarrow \mu\mu + inv$ channels.
- In the absence of initial or final state radiation, the expected signature of signal events is that of a Z boson, recoiling against the invisibly decaying Higgs boson. Thus the E_T^{miss} is expected to be balanced against the P_T of the Z boson. In this analysis events are rejected if $|E_T^{miss} - p_T^l|/p_T^l > 0.2$. The distribution of $|E_T^{miss} - p_T^l|/p_T^l$, after the E_T^{miss} cut, is shown in fig. 53(c) for a combination of the $ZH \rightarrow ee + inv$ and $ZH \rightarrow \mu\mu + inv$ channels.
- Finally to avoid selecting events with high E_T^{miss} originating from a badly measured jet, events are rejected if they have a jet with $p_T > 20$ Gev and $|\eta| < 2.5$. The distribution of the number of such jets, in events after the E_T^{miss} cut, is shown in fig. 53(d).

After the above selection the search for $ZH \rightarrow ll + inv$ is performed by looking for an excess over the background expectation in the E_T^{miss} distribution.

7.7 Signal samples

The $ZH \rightarrow ll + inv$ process is simulated using the HERWIG++ [104] and POWHEG [83] programs. In the simulation, the Higgs boson is produced in association with a Z boson which is forced to decay to two leptons (e , μ , or τ). The invisible decay of the Higgs boson is simulated by forcing the Higgs boson to decay to two Z bosons, which are then forced to decay to neutrinos. The ZH production cross section is taken to be that predicted by the SM, thus assuming that the impact from any BSM physics that might lead to invisible Higgs decays would not significantly affect the production processes. This is a reasonable assumption whenever the invisible particles have weak couplings to all SM particles except to the Higgs boson.

The SM ZH production cross sections as a function of the Higgs mass are listed in table 23. These cross sections are then convoluted with the $Z \rightarrow ll$ branching fractions [58]. For the signal expectation shown on any figure in this chapter the SM ZH cross section is used and a 100% branching ratio to invisible particles is assumed. Samples have been generated for a range of Higgs masses, $m_H = 115, 120, 125, 130, 150, 200$ and 300 GeV, at centre-of-mass energies of both $\sqrt{s} = 7$ and 8 TeV for the 2011 and 2012 analyses respectively.

m_H (GeV)	(7 TeV) $\sigma(ZH)$ (fb)	(8 TeV) $\sigma(ZH)$ (fb)
110	472	587
115	411	512
120	360	448
125	316	394
130	278	347
150	171	216
200	61	78
300	12	15

Table 23: Cross sections at $\sqrt{s} = 7$ and 8 TeV for SM ZH production at different Higgs masses. The cross sections are taken from from Ref. [59].

7.8 Backgrounds

The relevant backgrounds for this search are the same as those presented in section 6.2, and for the 2011 MC the same samples were used, except for the diboson samples for which the HERWIG generator was used. The generators used for the 2012 MC are given in this section.

7.8.1 Standard Model ZZ background

The SM ZZ background contributes the most to the final distribution, and is mostly irreducible. $ZZ \rightarrow ll ll$ and $ZZ \rightarrow ll \nu \nu$ samples are produced using Sherpa [105]. A dilepton mass filter is applied, where the invariant mass of charged lepton pair (ee , $\mu\mu$, or $\tau\tau$) is required to be larger than 4 GeV. The cross sections for the Sherpa ZZ samples are given in table 24.

channel	σ (fb)
$ZZ \rightarrow ll\nu\nu$	504
$ZZ \rightarrow llll$	768.6
$WZ \rightarrow lvll$	2510.2
$WW \rightarrow lvlv$	5679

Table 24: The ZZ, WZ, WW samples generated using the Sherpa Monte Carlo program and cross sections at $\sqrt{s} = 8$ TeV.

7.8.2 Standard Model WZ and WW background

The WZ background also contributes a significant amount to the final distribution. A more modest contribution is expected for the WW background. Both are simulated using Sherpa and details of the samples are given in table 24.

WZ control region To determine a control region for the WZ background the same method is used as that described in section 6.6, in which events with a nominal lepton pair and an additional lepton are selected. Fig. 54 shows the E_T^{miss} distribution for events with an additional lepton, and it can be seen that the high E_T^{miss} region is dominated by the WZ background. For $E_T^{miss} > 110$ GeV, 57 events are observed in data compared to 54.5 ± 3.7 expected events of which 33.0 ± 2.4 are WZ events.

7.8.3 Z+jets background

$Z \rightarrow ee$, $Z \rightarrow \mu\mu$ and $Z \rightarrow \tau\tau$ events are simulated using POWHEG [83] and PYTHIA8 [62]. The simulation of Z production includes both the Drell-Yan γ^* component and the $Z\gamma$ interference term, and a minimum mass of 60 GeV is required for the boson. The cross sections are scaled to NLO by accuracy [79]. The details of this sample are given in table 25.

7.8.4 $t\bar{t}$ and single top background

The background from top pair, Wt and single top events in the final selection is very small. It is simulated using the MC@NLO generator except for the t-channel single top quark production, for which AcerMC [80] generator is used. Details of the $t\bar{t}$ sample are given in table 26.

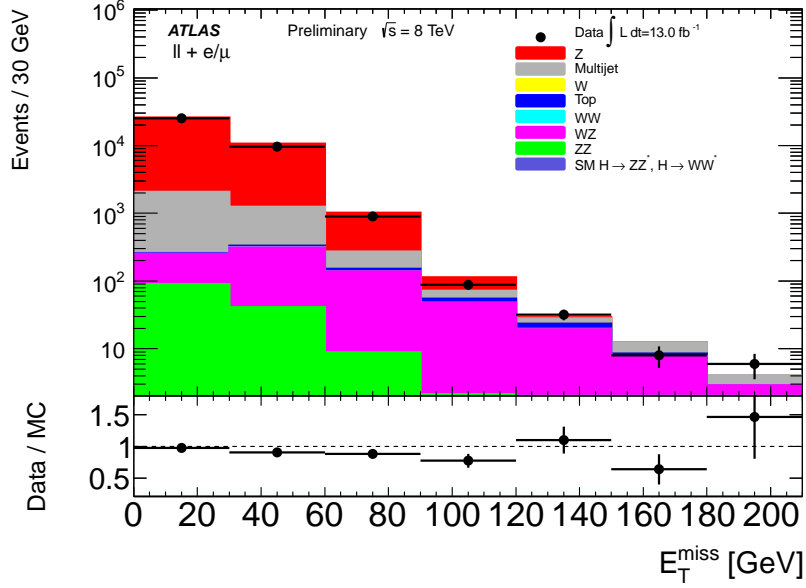


Figure 54: The E_T^{miss} distribution for events with an additional lepton for the 2012 dataset.

channel	$\sigma(\text{pb})$
$Z \rightarrow ee$	1150
$Z \rightarrow \mu\mu$	1150
$Z \rightarrow \tau\tau$	1150

Table 25: The inclusive $Z \rightarrow ll$ ($l = e, \mu, \tau$) samples generated using POWHEG + PYTHIA8. The cross sections are at $\sqrt{s} = 8 \text{ TeV}$ and are evaluated from theoretical calculations for Z production [79] convoluted with the Z branching fractions from [58]. The amount of MC simulated events associated with these samples are about 8.6 fb^{-1} (4.3 fb^{-1}) for the ee and $\mu\mu$ ($\tau\tau$) channels.

Top control region In order to ensure that the top background is well understood in the 2012 data a control region similar to that described in section 6.6 is used. Fig. 55 shows the E_T^{miss} distribution for events containing an electron-muon pair, the high E_T^{miss} region of which is dominated by the top background. For $E_T^{miss} > 90 \text{ GeV}$, 9573 events are observed in data compared to 9756 ± 79 expected events of which 9451 ± 63 are top events. The number of observed $e\mu$ events in data is 1.9% lower than the expected number of events.

channel	σ (fb)	filter	$\sigma_{filtered}$ (fb)
$t\bar{t}$	238060	0.543	129167
single t (s-chan, $W \rightarrow e\nu$)	606		
single t (s-chan, $W \rightarrow \mu\nu$)	606		
single t (s-chan, $W \rightarrow \tau\nu$)	606		
single t (t-chan, $W \rightarrow e\nu$)	9464		
single t (t-chan, $W \rightarrow \mu\nu$)	9464		
single t (t-chan, $W \rightarrow \tau\nu$)	9464		
Wt	22373		

Table 26: The $t\bar{t}$ sample in the lepton-hadron (lh) or lepton-lepton (ll) decay mode and the single top and Wt samples, all generated using the MC@NLO Monte Carlo program except the t -channel single top decays, which use AcerMC. The $t\bar{t}$ filter requires at least one of the W bosons from the top decays to decay leptonically. The cross sections are at $\sqrt{s} = 8$ TeV and are taken from the best known theory estimation recommended by the ATLAS top working group [59]. The cross sections listed are convoluted with the relevant branching fractions [58].

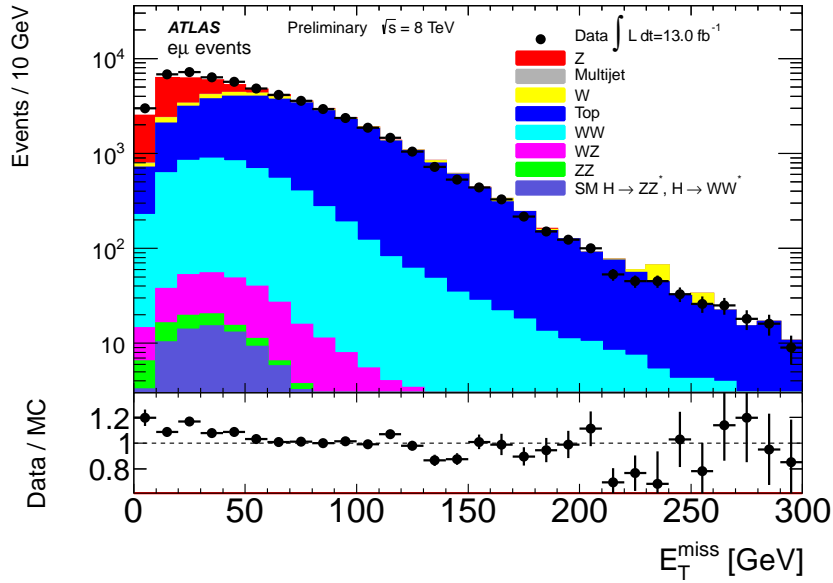


Figure 55: The E_T^{miss} distribution for events with an electron-muon pair for the 2012 dataset.

7.8.5 Inclusive W jet background

The inclusive W background is also expected to be a very small background. It is more likely to contribute to the electron channel than the muon channel as the jets in the event are more likely to fake electrons

than muons. This background is simulated using the ALPGEN MC generator. Details of the generated samples are given in table 27.

process	$\sigma(\text{fb})$
$W + 0p, W \rightarrow e\nu$	9645160
$W + 1p, W \rightarrow e\nu$	1895720
$W + 2p, W \rightarrow e\nu$	572900
$W + 3p, W \rightarrow e\nu$	160664
$W + 4p, W \rightarrow e\nu$	42736
$W + 5p, W \rightarrow e\nu$	12666
$Wb\bar{b} + 0p$	66818
$Wb\bar{b} + 1p$	54292
$Wb\bar{b} + 2p$	27895
$Wb\bar{b} + 3p$	13373
$Wc\bar{c} + 0p$	180228
$Wc\bar{c} + 1p$	159216
$Wc\bar{c} + 2p$	86168
$Wc\bar{c} + 3p$	36317
$Wc + 0p$	1227810
$Wc + 1p$	406767
$Wc + 2p$	106131
$Wc + 3p$	31231
$Wc + 4p$	6546

Table 27: The W +jet samples generated using the ALPGEN Monte Carlo program, where p refers to the number of additional partons generated in the matrix element. The cross sections are given at $\sqrt{s} = 8$ TeV and include a k -factor of 1.20 for W , $Wb\bar{b}$ and $Wc\bar{c}$ samples and 1.52 for Wc samples. The cross sections for $W \rightarrow \mu\nu$ and $W \rightarrow \tau\nu$ are assumed to be the same as those for $W \rightarrow e\nu$.

7.8.6 SM Higgs simulation

An additional background considered is that from the decay of a possible SM Higgs boson with mass $m_H = 125$ GeV. Samples at $m_H = 125$ GeV for the $H \rightarrow ZZ \rightarrow ll\nu\nu$ and $H \rightarrow WW \rightarrow l\nu l\nu$ decay modes,

where $l = e, \mu, \tau$, have been generated using the POWHEG generator interfaced with PYTHIA [62] showering including matrix elements up to NLO. Both gluon-gluon fusion and vector boson fusion production mechanisms are taken into account by the matrix elements. PYTHIA has been interfaced to PHOTOS [77], for initial state radiation, and to TAUOLA [78] for the simulation of the τ decays.

The cross sections for $H \rightarrow ZZ/WW$ via gg fusion are set to NNLO+NNLL accuracy and those for vector boson fusion are evaluated at NLO accuracy. Both production mechanisms include EW corrections [59]. All samples correspond to luminosities that are very high compared the available luminosity in the data ($\sim 150 \text{ fb}^{-1}$ or more). This background is found to be negligible.

7.8.7 QCD data driven estimation

The QCD estimation used for this analysis is similar to that presented in section 6.2. In order to keep the trigger rates at an acceptable level the p_T thresholds for the di-photon trigger used for the QCD estimation in 2011 were increased beyond 20 GeV, and so an alternative di-electron trigger was used for this estimation, with a p_T threshold at 12 GeV and no isolation requirements. This trigger selects events with two electrons with $p_T > 12$ GeV, which pass all of the criteria for a loose++ (section 4.3) electron, except for the isolation cuts. To obtain a QCD dominated sample the isolation requirement on the electrons was inverted with respect to the nominal selection, such that they were required to have $(\sum p_T(\Delta R < 0.2))/p_T > 0.1$. The m_{ll} distribution after this requirement is shown in fig. 56. With this modified selection with respect to the $H \rightarrow ZZ \rightarrow ll\nu\nu$ analysis no evidence of a Z peak is observed in the obtained m_{ll} distribution. The QCD background was estimated (as in section 6.2) by fitting the template to the sidebands of the m_{ll} distribution. This background is found to be negligible for the $Z \rightarrow ee$ channel. The QCD contribution to the $Z \rightarrow \mu\mu$ channel is expected to be much smaller than in the $Z \rightarrow ee$ channel. This background is taken to be negligible.

7.9 Systematic uncertainties

For the 2011 dataset the uncertainties on the luminosity, lepton trigger and identification efficiencies, lepton energy scale and resolution and background normalisation are the same as those described in section 6.7, with minor updates to the numerical values. The uncertainties applied for the 2012 dataset are listed below.

Luminosity uncertainty The luminosity uncertainty used for the 2012 data is 3.6%. It is derived, following the same methodology as that detailed in [85], from a preliminary calibration of the luminosity

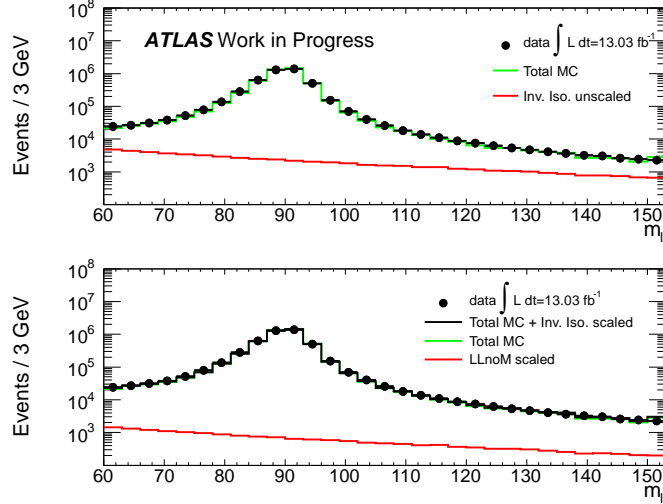


Figure 56: The dilepton invariant mass for events with 2 loose++ anti-isolated electrons for the QCD background estimation.

scale derived from beam-separation scans performed in April 2012. This uncertainty is only applied to MC samples for which the normalisation error is not taken directly from a comparison between data and MC.

Leptons and jets Lepton trigger and identification efficiencies as well as energy scale and resolution uncertainties are derived from high statistics Z samples. These are implemented into the analysis using the same method as described in section 6.7. When propagated to the event selection, these uncertainties contribute typically 1.0 – 1.5% to the overall selection uncertainty in the signal and backgrounds estimated from the MC simulation. Jet energy scale (JES) and resolution (JER) uncertainties are derived using a combination of techniques that use di-jet, photon + jet, and Z + jet events [106]. These uncertainties contribute to the jet-veto uncertainties for jets with $p_T > 20$ GeV and $|\eta| < 2.5$ and to the E_T^{miss} uncertainty for all remaining jets.

Jet veto uncertainty Single Z -boson data are used to reduce uncertainty on the acceptance of the jet veto in Standard Model ZZ background in the ZH analysis. The Z bosons are selected using di-electron and di-muon data with invariant masses within 15 GeV of the Z -boson mass. Object selection criteria are the same as for the nominal analysis. A MC correction is applied to account for the difference of jet veto acceptance between Z and ZZ events. Both the Z sample and the ZZ sample are generated by POWHEG

and showered by PYTHIA 8. The predicted jet veto acceptance for ZZ can be written as

$$\epsilon_{ZZ}^{predicted} = \epsilon_Z^{data} \frac{\epsilon_{ZZ}^{MC}}{\epsilon_Z^{MC}}. \quad (54)$$

The Z boson data provides an effective calibration of the jet energy scale, and the only veto uncertainties are statistical and from potential background to the Z boson data, which are negligible. The veto uncertainties in the Z and ZZ samples are taken to be correlated and thus cancel out in equation 54. The effects of the experimental (mainly JES and JER) and theoretical (QCD scale, PDF set and parton showering) uncertainties can be studied by shifting the corresponding parameter in the Z and ZZ MC samples [5]. The total systematic uncertainties on the jet veto acceptances for ZZ events is 0.77% (0.33% experimental 0.70% theoretical).

Signal sample uncertainties Uncertainties on the ZH production cross section are derived from variations of the QCD scale, α_s and PDF variations [59, 86] combined to give an uncertainty of 4.9-5.1% on the cross section for the SM Higgs boson having a mass between 115 and 300 GeV. This analysis is sensitive to the simulation of the Higgs boson p_T through the E_T^{miss} , and uncertainties in the p_T boost of the Higgs boson can affect the signal yield. Currently, an additional systematic uncertainty of 1.9% is applied to the normalisation [107, 108], and differential uncertainties as a function of the Higgs boson p_T is considered as shape systematics.

ZZ normalisation The normalisation uncertainty on the background Monte Carlo used to estimate the ZZ background is 5% from varying the PDFs. The theoretical uncertainty on the jet veto is estimated as 0.70% (0.77%) for 2011 (2012) in the diboson events from generator studies. The impact of PDF, α_s , and QCD scale uncertainties on the shape of the E_T^{miss} distributions are also considered [86], as are the effects of the missing quark-box diagrams ($gg \rightarrow ZZ$). The theoretical uncertainty of the WZ and WW background is determined in a similar way.

The object and theoretical uncertainties are considered as correlated between the 2011 and 2012 data, and between the signals and all the backgrounds estimated from the MC simulation. The systematic uncertainties in the data-driven methods are also assumed to be correlated between the two datasets. The luminosity uncertainty is considered as uncorrelated between the 2011 and 2012 data.

7.10 Results

The E_T^{miss} distributions, after all of the analysis cuts described in section 7.6 have been applied, are shown in fig. 57 for a Higgs of mass 125 GeV for both the 2011 and 2012 datasets. The E_T^{miss} distributions for

Process	Estimation method	Uncertainty (%)	
		2011	2012
ZH Signal	MC	8	8
ZZ	MC	11	10
WZ	MC	12	14
WW	MC	14	not used
Top quark	MC	50	not used
Top quark, WW and $Z \rightarrow \tau\tau$	$e\mu$ CR	not used	4
Z	ABCD method	56	51
W + jets, multijet	Matrix method	15	6

Table 28: Summary of the systematic uncertainties on each background and on the signal yield. The method used to estimate the backgrounds and the associated sources of systematic uncertainties are given. The total systematic uncertainties for each data taking period are given. For the definition of the ABCD, the matrix and the $e\mu$ CR methods see section 7.11.

the other masses have the same backgrounds and a similar signal shape and thus these mostly vary in the number of expected signal events.

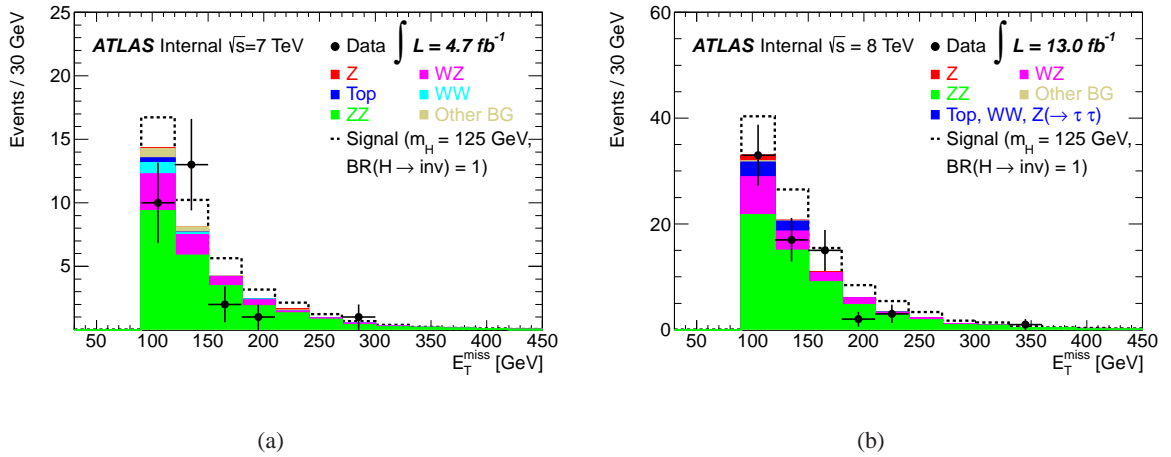


Figure 57: Distributions of E_T^{miss} for signal events in the 2011 data taking period (a) and the 2012 data taking period (b). The observed data are indicated by the black points and the histograms represent the background predictions. The dashed line indicates the prediction from the signal expectation shown and is stacked on the background prediction. The signal model assumes the SM ZH production cross section for a Higgs with a mass of 125 GeV and a 100% branching fraction to invisible particles.

Table 29 gives the total number of expected events for each background with the statistical and systematic uncertainties for both years. The total number of data events is also given and is consistent with the total expected backgrounds within the uncertainties.

Process	2011 (7 TeV)	2012 (8 TeV)
ZZ	$23.5 \pm 0.8 \pm 2.5$	$56.5 \pm 1.2 \pm 5.7$
WZ	$6.2 \pm 0.4 \pm 0.8$	$13.9 \pm 1.2 \pm 1.9$
WW	$1.1 \pm 0.2 \pm 0.2$	$4.7 \pm 0.5 \pm 0.2$
Top quark	$0.4 \pm 0.1 \pm 0.2$	$1.1 \pm 0.6 \pm 0.9$
Z	$0.0 \pm 0.0 \pm 0.0$	$2.4 \pm 2.4 \pm 0.0$
$W + \text{jets}$	$0.0 \pm 0.0 \pm 0.0$	$0.0 \pm 0.0 \pm 0.0$
QCD	$0.0 \pm 0.0 \pm 0.0$	$0.0 \pm 0.0 \pm 0.0$
SM Higgs	$0.0 \pm 0.0 \pm 0.0$	$0.0 \pm 0.0 \pm 0.0$
Total BG	$31.2 \pm 1.0 \pm 3.1$	$78.6 \pm 2.0 \pm 6.8$
Observed	27	71
Signal ($m_H = 125$ GeV)	$8.1 \pm 0.2 \pm \pm 0.3$	$25.4 \pm 0.7 \pm 0.1$

Table 29: Observed number of events and expected contributions from each background source and expected number of signal events for the candidate boson at $m_H = 125$ GeV assuming a SM ZH production cross section and a 100% invisible branching ratio, separated into the 2011 and 2012 data taking periods. Uncertainties associated with the background and signal predictions are presented with the statistical uncertainty first and the systematic uncertainty second.

7.11 Limits

The limits presented in this section are those calculated using the analysis presented in [5]. The differences between this published analysis and that presented in this chapter are small, and are listed below for completeness.

- The Z background is estimated using a data driven method for both years. This method consists of selecting two variables that partially isolate the Z background, the fractional p_T difference and $\Delta\phi(E_T^{miss}, p_T^{miss})$, and defining 4 regions, labelled ABCD, that are made up of combinations of parameter space of the 2 variables with low and high Z concentration. The number of events in the signal region (A) is estimated by measuring the number of events in regions B (high

$\Delta\phi(E_T^{miss}, p_T^{miss})$, C (high fractional p_T diff) and D (high both) and assuming that B/D is equal to A/C.

- The W and QCD backgrounds are estimated by determining the fake rate of leptons faking jets, and using a matrix method to calculate the expected contribution to the W (1 fake lepton) and QCD (2 fake leptons) backgrounds.
- For 2012 a data driven method based on the $e\mu$ control regions presented in section 7.12 is used to estimate the combined WW , $t\bar{t}$, Wt and $Z \rightarrow \tau\tau$ backgrounds. It assumes that the ratio of $e\mu$ events is twice that of the ee and $\mu\mu$ after appropriate corrections for differences in electron and muon selection efficiencies.

It must be noted that all of the above differences effect only the less important backgrounds, and that the estimated number of events in each background are consistent with those obtained from MC in this analysis.

The limit setting procedure used for this analysis is the fully frequentist method implemented using RooStats, and is described in section 6.9. There are two scenarios considered in the limits. The first is to interpret the results as a limit on the invisible branching ratio of the candidate Higgs boson at mass 125 GeV. In this case one uses the distributions shown in fig. 57 and the systematics described in section 7.9 to set an upper limit on the $BR(H \rightarrow inv)$ of the Higgs candidate. Fig. 58 (a) shows the observed and expected $1 - CL$ as a function of the invisible branching ratio, the red lines indicate the 68 and 95% exclusion limits. The observed limit result sets an upper limit of 65% on the invisible branching ratio of the Higgs candidate at 95% confidence level. The expected limit is 84%. This limit assumes a SM production rate. The log likelihood ratio is shown in fig. 58 (b) as a function of branching ratio.

The second scenario considered places exclusion limits on $\sigma_{ZH} \times BR(H \rightarrow inv)$ for other Higgs-like bosons at masses in the range $115 < m_H < 300$ GeV. Fig. 59 shows the 95% CL upper limit on the cross section convoluted with the $Z \rightarrow ll$ and $H \rightarrow inv$ branching ratios. The dashed red line represents the expected cross section for a Higgs candidate assuming the SM ZH production rate and a 100% branching ratio to invisible particles. For masses $m_H \neq 125$ GeV no invisible branching ratio of the 125 GeV candidate is assumed. The dashed black line indicates the expected 95% CL upper limit for a background only experiment. There is a modest deficit in the number of observed events in the final distributions compared to that expected from a background only experiment. Therefore the observed cross section limits are somewhat stronger than expected.

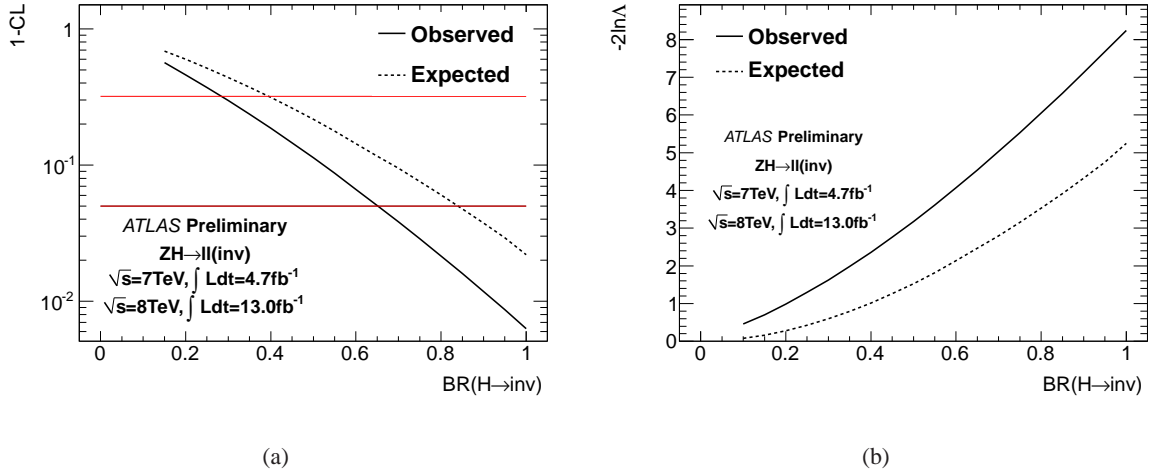


Figure 58: 95% confidence level limits on the cross section times branching fraction of a Higgs-like state decaying to invisible particles. Figure (a) shows limits derived from the 2011 data taking period, figure (b) shows limits for the 2012 data taking period, and figure (c) shows the limits derived from the combination of both periods. Dashed lines show the background only expected limits and solid lines show the observed limit.

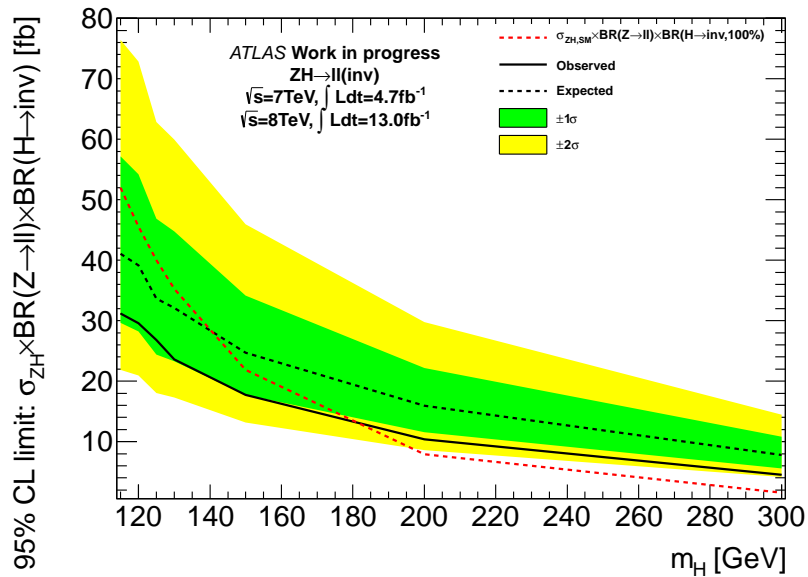


Figure 59: 95% confidence level limits on the cross section times branching fraction of a Higgs-like state decaying to invisible particles. The limits shown are a combination of the 2011 and 2012 data and MC samples. The dashed line show the background only expected limits and the solid line shows the observed limit.

7.12 Conclusion

A direct search for evidence of invisible decays of a Higgs boson at the LHC has been performed. While the invisible branching fraction for a SM Higgs boson is too small to be accessible, this measurement

is sensitive to enhancements of the invisible branching fraction, such as from decays to dark matter particles. After the full selection, 27 events are observed compared to a SM expectation of 32.7 ± 1.0 (stat.) ± 3.1 (syst.) background events in 4.7 fb^{-1} of data taken at $\sqrt{s} = 7 \text{ TeV}$ during the 2011 run and 71 events are observed compared to an expected 78.0 ± 2.0 (stat.) ± 6.8 (syst.) background events in 13 fb^{-1} of data taken at $\sqrt{s} = 8 \text{ TeV}$ during part of the 2012 run. No significant excess over the expected background is observed and limits are set on the allowed invisible branching fraction of the recently observed 125 GeV Higgs boson candidate. Assuming the SM ZH production rate for a 125 GeV SM Higgs boson, limits are set on the maximum allowed invisible branching fraction. The observed upper limit on the $H \rightarrow inv$ branching fraction is 65% at 95% confidence level, and the expected limit is 84%. At the 68% confidence level the observed upper limit is 29%, and the expected limit is 39%. Limits are also set on the cross section times invisible branching fraction of a possible additional Higgs-like boson over the mass range $115 \text{ GeV} < m_H < 300 \text{ GeV}$. No excess is observed over the mass range [5].

Chapter 8

Summary

The LHC stopped colliding protons at the end of 2012, and is not scheduled to start again until 2015. Over the last 3 years it has performed beyond expectations, and has supplied all 4 detectors with vast amounts of data. The ATLAS detector has recorded data with a high efficiency, allowing the collaboration to study the Standard Model to a new level of accuracy, discover a new boson and put stringent limits on many new physics models. Over 130 papers have already been published using the first 3 years of data, and many more are scheduled to appear after the full 2011-2012 dataset has been analysed. The analyses presented in this thesis used the data from all 3 years of collisions.

In chapter 5 a pre-data study on the possibility of excluding a high mass SM Higgs boson with a limited luminosity using the $H \rightarrow ZZ \rightarrow ll ll$ channel was presented. It was found that the most sensitive region for this channel was at around $m_H = 200$ GeV. Using the 2010 dataset this channel was combined with the other high mass channels, $H \rightarrow ZZ \rightarrow ll \nu \nu$ and $H \rightarrow ZZ \rightarrow ll qq$, and it was found that for Higgs masses greater than 200 GeV the $H \rightarrow ZZ \rightarrow ll \nu \nu$ channel has the best sensitivity in the high mass range.

The search for the SM Higgs boson using 4.7 fb^{-1} of data at $\sqrt{s} = 7$ TeV was presented in chapter 6. A SM Higgs boson with a mass between 320 and 560 GeV is excluded at a 95% confidence level using this channel alone. This analysis was one of the channels that went in to the ATLAS Higgs combination which led to the discovery of a new particle consistent with a Higgs boson, at a mass ~ 125 GeV. The observation of a new particle at this mass was a joint effort between the ATLAS and CMS collaborations. Measurements of the spin of the new boson and its couplings to other particles are required in order to confirm that it is indeed the Standard Model Higgs boson. Although early measurements show that the discovered boson is consistent with the SM Higgs boson, a much more detailed confirmation will be possible when data taking starts again in 2015. The centre-of-mass energy after the shutdown will be increased to $\sqrt{s} = 13$ or 14 TeV and a significant amount of luminosity will be collected. This will allow a range of decay and production modes of the Higgs boson candidate to be studied to a high level of accuracy.

Finally a search for anomalous invisible decays of the Higgs boson candidate at $m_H = 125$ GeV using both the 4.7 fb^{-1} 2011 dataset and the 13 fb^{-1} 2012 dataset was presented in chapter 7. This analysis was motivated by the possibility of observing a dark matter candidate. An upper limit of 65% was set

on the allowed $H \rightarrow inv$ branching fraction at 95% confidence level. Limits were also set on further Higgs-like bosons decaying predominantly to invisible particles at masses between 115 and 300 GeV, and no excesses were observed.

The increase in centre-of-mass energy after the shutdown and an expected 300 fb^{-1} of luminosity will allow ATLAS to probe physics beyond the SM at the TeV scale. A further upgrade of the ATLAS detector is planned, aimed at ultimately collecting 3000 fb^{-1} per general purpose experiment. This will allow very high precision tests of the Higgs boson candidate to be performed, and to possibly measure the self-coupling of the Higgs. The self-coupling will give the form of the Higgs potential and is a key test of the electro-weak symmetry breaking mechanism in the SM.

8.1 Current status of the new boson

As of July 2013 the evidence of the discovery of a new boson with a mass of approximately 125 GeV from the two experiments, ATLAS and CMS, is incontrovertible. The significance of the observed peak for each of the channels at $m_H = 125.5 \text{ GeV}$ for ATLAS and $m_H = 125.7 \text{ GeV}$ for CMS is given in table 30.

Higgs Boson Decay	Significance	
	ATLAS ($m_H = 125.5 \text{ GeV}$)	CMS ($m_H = 125.7 \text{ GeV}$)
$H \rightarrow \gamma\gamma$	7.4σ	3.2σ
$H \rightarrow ZZ^{(*)} \rightarrow 4l$	6.6σ	6.7σ
$H \rightarrow WW$	3.8σ	3.9σ
$H \rightarrow \tau\tau$	1.1σ	2.8σ
$VH \rightarrow Vbb$	–	2.0σ

Table 30: The significance of the excess at $m_H = 125.5 \text{ GeV}$ for ATLAS and $m_H = 126.5 \text{ GeV}$ for CMS for each channel [109–115]. As no excess was observed in the ATLAS $VH \rightarrow Vbb$ channel, no significance is quoted.

A summary plot showing the signal strength of the five channels normalised to the SM expectation from ATLAS and CMS is shown in fig. 60. The two plots also contain the signal strength for the combination of the channels for the individual experiments. These plots show that the coupling strength for each of the individual channels does not deviate far from the SM Higgs prediction. Further statistics are required in order to determine the coupling strengths more precisely, and to conclusively confirm that the coupling to fermions. An increase in statistics will also allow a measurement of the rate of the different production mechanisms for each channel to be made.

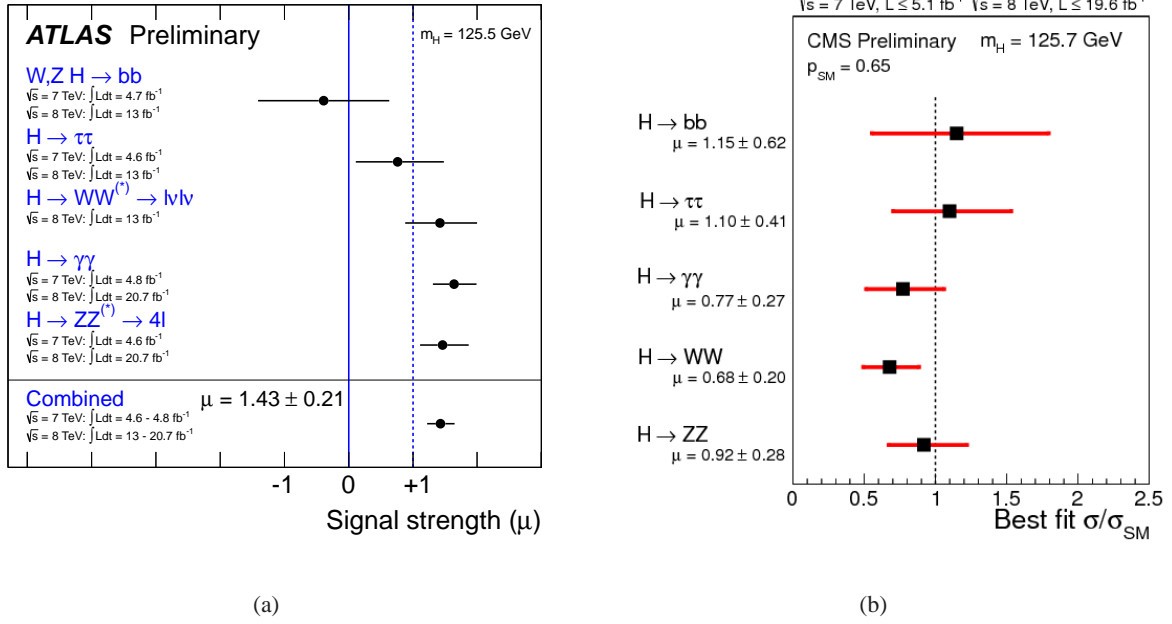


Figure 60: The production strengths as measured by (a) ATLAS and (b) CMS for a Higgs boson of mass $m_H = 125.5$ and 125.7 GeV respectively, normalised to the SM expectations. The data used for the CMS analyses corresponds to the full 2011 and 2012 dataset, and for ATLAS the luminosity used is given on the plot [109–114].

8.2 Mass measurement

The mass of the Higgs boson is determined most precisely by the $H \rightarrow \gamma\gamma$ and the $H \rightarrow ZZ^{(*)} \rightarrow 4l$ channels, as the final state can be fully reconstructed. For ATLAS the combined mass measurement is observed to be $m_H = 125.5 \text{ GeV} \pm 0.2(\text{stat}) {}^{+0.5}_{-0.6}(\text{sys})$ [109], shown in fig. 61 (a). A 2.5σ discrepancy in the mass measurement between the two channels is observed. This is thought to be a statistical fluctuation. No such discrepancy is observed for the CMS mass measurement, which measures the mass of the boson to be $m_H = 125.7 \text{ GeV} \pm 0.3(\text{stat}) \pm 0.3(\text{sys})$ [116] as shown in fig. 61 (a). The measurements of the mass from the two experiments are in agreement.

8.3 Spin and parity measurement

The SM Higgs boson is predicted to be spin 0, and have positive parity, denoted by $J^P = 0^+$. The observation of the Higgs decaying to a final state with two photons rules out the $J = 1$ spin quantum number. The measurements of the spin and parity are done simultaneously, using the angular variables of the final state particles in the $H \rightarrow \gamma\gamma$, the $H \rightarrow ZZ^{(*)} \rightarrow 4l$ and $H \rightarrow WW^{(*)} \rightarrow l\nu l\nu$ channels. The observables used are independent of the coupling strength. The measurement is made separately

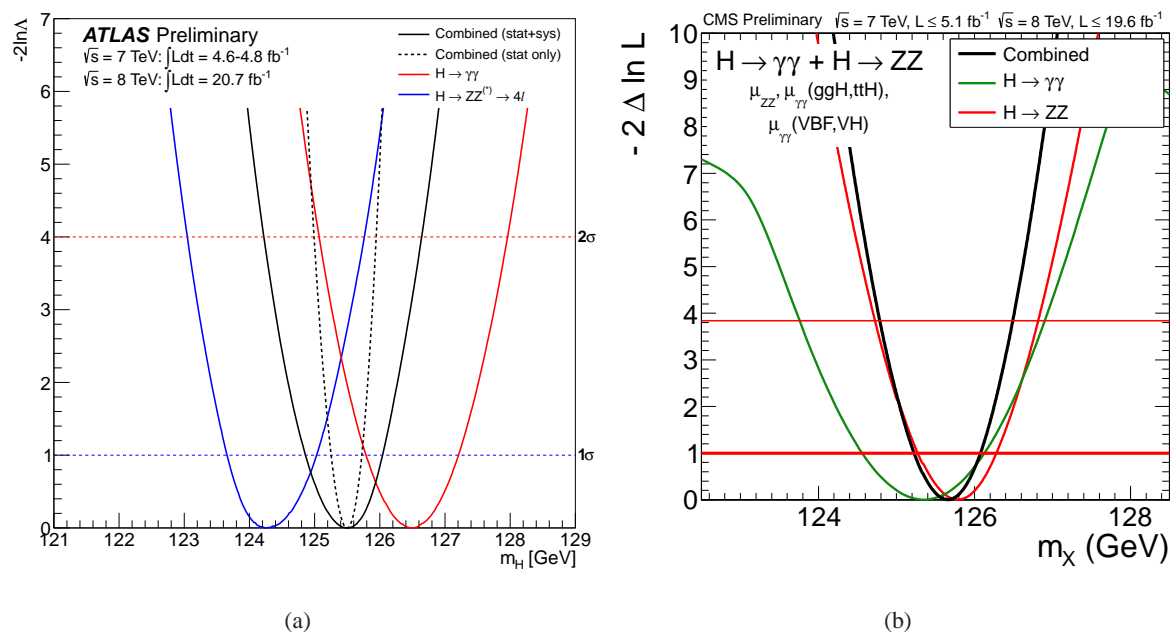


Figure 61: The (a) ATLAS and (b) CMS measurements of the mass of the Higgs boson shown individually for the $H \rightarrow \gamma\gamma$ and the $H \rightarrow ZZ^{(*)} \rightarrow 4l$ channels, and the combination. For ATLAS the difference between the mass measurements corresponds to a significance of 2.5σ [109, 116].

for each experiment using the complete 2011 and 2012 dataset. For ATLAS the data are compatible with the $J^P = 0^+$ scenario, and the alternative spin and parity scenarios, $J^P = 0^-, 1^+, 1^-$ and 2^+ are excluded with a confidence level greater than 97.8% [117]. CMS has excluded the $J^P = 0^-$ scenario with a confidence level of greater than 99.8% [118]. The $J^P = 2^+$ scenario has also been excluded by CMS with a confidence level of greater than 99.4% [116].

References

- [1] ATLAS Collaboration, *Search for a Standard Model Higgs Boson in the Mass Range 200-600 GeV in the Channels $H \rightarrow ZZ \rightarrow l\nu\nu$ and $H \rightarrow ZZ \rightarrow llqq$ with the ATLAS Detector*, ATLAS-CONF-2011-026 (2011).
- [2] ATLAS Collaboration, *Search for a Standard Model Higgs Boson in the $H \rightarrow ZZ \rightarrow ll\nu\nu$ Decay Channel with the ATLAS Detector*, Phys. Rev. Lett. **107** (2011) 221802.
- [3] ATLAS Collaboration, *Search for a Standard Model Higgs boson in the $H \rightarrow ZZ \rightarrow l\nu\nu$ decay channel using 4.7 fb^{-1} of $\sqrt{s} = 7 \text{ TeV}$ data with the ATLAS Detector*, Phys. Lett. B **717** (2012) 29–48.
- [4] ATLAS Collaboration, *Observation of a new particle in the search for the Standard Model Higgs boson with the ATLAS detector at the LHC*, Phys. Lett. B **716** (2012) 1–29.
- [5] ATLAS Collaboration, *Search for invisible decays of a Higgs boson produced in association with a Z boson in ATLAS*, ATLAS-CONF-2013-011 (2013).
- [6] D. J. Griffiths, *Introduction to Elementary Particles*. TextBook Physics. Wiley, New York, NY, 1987.
- [7] The LEP Electroweak Working Group. <http://lepewwg.web.cern.ch/LEPEWWG/stanmod/>.
- [8] Elliot Leader, Enrico Predazzi, *An Introduction to gauge fields and modern particle physics*. Cambridge University Press, 1996.
- [9] R. K. Ellis, W. J. Stirling, and B. R. Webber, *QCD and Collider Physics*. Cambridge monographs on particle physics, nuclear physics, and cosmology. Cambridge Univ. Press, Cambridge, 2003.
- [10] F. Halzen and A. D. Martin, *Quarks and leptons: an introductory course in modern particle physics*. Wiley, New York, NY, 1984.
- [11] P.W Higgs, *Broken symmetries and the masses of gauge bosons*, Phys. Rev. Lett. **13** (1964) 508–509.
- [12] P. Higgs, *Broken symmetries, massless particles and gauge fields*, Phys. Lett. **12** (1964) 132.
- [13] F. Englert and R. Brout, *Broken symmetry and the mass of gauge vector mesons*, Phys. Rev. Lett. **13** (1964) 321.

- [14] D. Kohler, B. A. Watson and J. A. Becker, *Experimental search for a low-mass scalar boson*, Phys. Rev. Lett. **33** (1974) 1628.
- [15] R. Barbieri and T. E. O. Ericson, *Evidence against the existence of a low mass scalar boson from neutron-nucleus scattering*, Phys. Lett. B **57** (1975) 270–272.
- [16] J. Ellis, M. K. Gaillard, and D. V. Nanopoulos, *A Historical Profile of the Higgs Boson*, CERN-PH-TH-2012-009 (2012).
- [17] F. Abe *et al.*, *Observation of top quark production in $\bar{p}p$ collisions with the collider detector at Fermilab*, Phys. Rev. Lett. **74** (1995) 2626–2631.
- [18] CDF and D0, *Combined CDF and D0 Upper Limits on Standard Model Higgs Boson Production with up to 8.6 fb⁻¹ of Data*, FERMILAB-CONF-11-354-E (2011).
- [19] CERN. <https://twiki.cern.ch/twiki/bin/view/LHCPhysics/CrossSections>.
- [20] F. Zwicky, *Spectral displacement of extra galactic nebulae*, Astrophys.J.86 (1937) 217–246.
- [21] J. L. Feng, *Dark Matter Candidates from Particle Physics and Methods of Detection*, UCI-TR-2009-13 (2010).
- [22] Q. Ahmad *et al.*, *Direct Evidence for Neutrino Flavor Transformation from Neutral-Current Interactions in the Sudbury Neutrino Observatory*, Phys. Rev. Lett. **89** (2002) 011301. 6 p.
- [23] A. Ghosh, T. Thakore, and S. Choubey, *Determining the Neutrino Mass Hierarchy with INO, T2K, NOvA and Reactor Experiments*, arXiv:1212.1305 (2012).
- [24] S. Pascoli, S. T. Petcov, and T. Schwetz, *The Absolute Neutrino Mass Scale, Neutrino Mass Spectrum, Majorana CP-Violation and Neutrinoless Double-Beta Decay*, Nucl. Phys. B **734** (2005) 24–49. 28 p.
- [25] LEP Electroweak Working Group Line SHape Subgroup, *Combination procedure for the precise determination of Z boson parameters from results of the LEP experiments*, hep-ex/0101027 (2001).
- [26] P. Fox *et al.*, *LEP Shines Light on Dark Matter*, arXiv:1103.0240 (2011).
- [27] L. Evans and P. Bryant, *The LHC Machine*, PoS EPS-HEP2009 (2009) 004.
- [28] ATLAS public images <http://www.atlas.ch/photos/index.html>.

- [29] *ATLAS: letter of intent for a general-purpose pp experiment at the large hadron collider at CERN*. Letter of Intent. CERN, Geneva, 1992.
- [30] ATLAS Collaboration, *ATLAS Inner Detector: Technical Design Report*, CERN-LHCC-97-016 (1997).
- [31] ATLAS Collaboration, *ATLAS Liquid-Argon Calorimeter: Technical Design Report*, CERN-LHCC-96-041 (1996).
- [32] ATLAS Collaboration, *ATLAS Tile Calorimeter: Technical Design Report*, CERN-LHCC-96-042 (1996).
- [33] ATLAS Collaboration, *ATLAS Muon Spectrometer: Technical Design Report*, CERN-LHCC-96-042 (1996).
- [34] ATLAS Collaboration, *Expected Performance of the ATLAS Experiment - Detector, Trigger and Physics*, arXiv:0901.0512.
- [35] ATLAS Collaboration, *The ATLAS Experiment at the CERN Large Hadron Collider*, J. Instrum. **3** (2008) S08003. 437 p.
- [36] P. A. Coe *et al.*, *Frequency Scanning Interferometry in ATLAS: Remote, Multiple, Simultaneous and Precise Distance Measurements in a Hostile Environment*, Meas. Sci. Tech. **15** 2175–2187.
- [37] F. Meloni, A. Milov, S. Pagan-Griso, K. Prokofiev and A. Wildauer, *Vertexing Performance Data vs MC comparison for LPCC*, ATL-COM-PHYS-2011-1312 (2011).
- [38] ATLAS Collaboration, *Performance of the ATLAS muon trigger in 2011*, ATLAS-CONF-2012-099 (2012).
- [39] ATLAS Collaboration, *Performance of the ATLAS Electron and Photon Trigger in p-p Collisions at $\sqrt{s} = 7$ TeV in 2011*, ATLAS-CONF-2012-048 (2012).
- [40] ATLAS Collaboration, *Search for the Standard Model Higgs boson in the decay channel $H \rightarrow ZZ^{(*)} \rightarrow 4l$ with 40 pb^{-1} of pp collisions at $\sqrt{s} = 7$ TeV*, ATLAS-CONF-2011-048 (2011).
- [41] <https://twiki.cern.ch/twiki/bin/view/AtlasPublic/LuminosityPublicResults>.
- [42] R. Nicolaidou *et al.*, *Muon identification procedure for the ATLAS detector at the LHC using Muonboy reconstruction package and tests of its performance using cosmic rays and single beam data*, J.Phys **219** (2010). part 3.

- [43] ATLAS Collaboration, *Muon reconstruction efficiency in reprocessed 2010 LHC proton-proton collision data recorded with the ATLAS detector*, ATLAS-CONF-2011-063 (2011).
- [44] ATLAS Collaboration, *Electron performance measurements with the ATLAS detector using the 2010 LHC proton-proton collision data*, Eur. Phys. J. C **72** (2012) 1909.
- [45] ATLAS Collaboration, *Improved electron reconstruction in ATLAS using the Gaussian Sum Filter-based model for bremsstrahlung*, ATLAS-CONF-2012-047 (2012).
- [46] W. Lampl *et al.*, *Calorimeter Clustering Algorithms: Description and Performance*, ATL-LARG-PUB-2008-002 (2008).
- [47] M. Cacciari, G. P. Salam and G. Soyez, *The Anti- $k(t)$ jet clustering algorithm*, JHEP **0804** (2008).
- [48] ATLAS Collaboration, *Jet energy scale and its systematic uncertainty for jets produced in proton-proton collisions at $\sqrt{s} = 7$ TeV and measured with the ATLAS detector*, ATLAS-CONF-2010-056 (2010).
- [49] ATLAS Collaboration, *Update on the jet energy scale systematic uncertainty for jets produced in proton-proton collisions at $\sqrt{s} = 7$ TeV measured with the ATLAS detector*, ATLAS-COM-CONF-2011-008 (2011).
- [50] E. Abat *et al.*, *Study of energy response and resolution of the ATLAS barrel calorimeter to hadrons of energies from 20-GeV to 350-GeV*, Nucl. Instrum. Methods Phys. Res., A **621** (2010) 134–150.
- [51] ATLAS Collaboration, *Search for a Standard Model Higgs in the $H \rightarrow ZZ \rightarrow ll\nu\nu$ decay channel with 4.7 fb^{-1} with the ATLAS detector*, ATLAS-CONF-2012-016 (2012).
- [52] ATLAS Collaboration, *Commissioning of the ATLAS high-performance b -tagging algorithms in the 7 TeV collision data*, ATLAS-CONF-2011-102 (2011).
- [53] ATLAS Collaboration, *Measurement of the b -tag Efficiency in a Sample of Jets Containing Muons with 5 fb^{-1} of Data from the ATLAS Detector*, ATLAS-CONF-2012-043 (2012).
- [54] ATLAS Collaboration, *Measurement of the Mistag Rate with 5 fb^{-1} of Data Collected by the ATLAS Detector*, ATLAS-CONF-2012-040 (2012).
- [55] ATLAS Collaboration, *Performance of Missing transverse momentum reconstruction in ATLAS with 2011 proton-proton collisions at $\sqrt{s} = 7$ TeV*, ATLAS-CONF-2012-101 (2012).

- [56] ATLAS Collaboration, *Reconstruction and Calibration of Missing Transverse Energy and Performance in Z and W events in ATLAS Proton-Proton Collisions at 7 TeV*, ATLAS-CONF-2011-080 (2011).
- [57] C. Gwilliam *et al.*, *Discovery prospects for a very high mass Higgs boson in the channels $H \rightarrow ZZ \rightarrow ll\nu\nu$, $H \rightarrow ZZ \rightarrow llbb$ and $H \rightarrow ZZ \rightarrow ll\ell\ell$* , ATL-PHYS-INT-2010-117 (2010).
- [58] Particle Data Group Collaboration, *Review of Particle Physics*, Phys. Lett. **B667** (2008) 1.
- [59] LHC Higgs Cross Section Working Group, S. Dittmaier, C. Mariotti, G. Passarino, and R. T. (Eds.), *Handbook of LHC Higgs Cross Sections: 1. Inclusive Observables*, CERN-2011-002 (2011).
- [60] S. Frixione and B. R. Webber, *Matching NLO QCD computations and parton shower simulations*, JHEP **0206** (2002).
- [61] J. M. Butterworth, J. R. Forshaw and M. H. Seymour, *Multiparton interactions in photoproduction at HERA*, Z. Phys. C **72** (1996).
- [62] T. Sjostrand, S. Mrenna and P. Z. Skands, *PYTHIA 6.4 Physics and Manual*, JHEP **0605** (2006) 026.
- [63] ATLAS Collaboration, *ATLAS sensitivity prospects for the Standard Model Higgs boson in the decay channel $H \rightarrow ZZ^{(*)} \rightarrow 4l$ at $\sqrt{s} = 10$ and 7 TeV*, ATL-PHYS-INT-2010-062 (2010).
- [64] R. Asfandiyarov *et al.*, *Production Cross Sections of the Higgs Boson and Other Standard Model Processes in pp Collisions at Different Centre-of-Mass Energies*, ATL-COM-PHYS-2009-051 (2009).
- [65] T Binoth and N. Kauer and P. Mertsch, *Gluon-induced QCD corrections to $pp \rightarrow ZZ \rightarrow l\bar{l}l'\bar{l}'$* , arXiv:0807.0024 (2008).
- [66] M. L. Mangano *et al.*, *ALPGEN, a generator for hard multiparton processes in hadronic collisions*, JHEP **07** (2003) 001.
- [67] A. Shibata *et al.*, *Understanding Monte Carlo Generators for Top Physics*, ATL-COM-PHYS-2009-334 (2009).
- [68] A. L. Read, *Presentation of search results: The CL_s technique*, J. Phys. **G 28** (2002) 2693–2704.

- [69] T. Junk, *Confidence Level Computation for Combining Searches with Small Statistics*, Nucl. Instrum. Meth. A 434 (1999).
- [70] T. Junk, *Building a more general χ^2* , CDF 7904.
- [71] T. Junk, *Sensitivity, Exclusion and Discovery with Small Signals, Large Backgrounds, and Large Systematic Uncertainties*, CDF 8128 (2007).
- [72] ATLAS Collaboration, *Search for a Standard Model Higgs in the $H \rightarrow ZZ \rightarrow ll\nu\nu$ decay channel with 2.05 fb^{-1} of ATLAS data*, ATLAS-CONF-2011-148 (2011).
- [73] H. Ruiz and M. Bosman, *Discovery potential of a heavy Standard Model Higgs boson through the $H \rightarrow ZZ \rightarrow ll\nu\nu$ channel*, ATL-PHYS-2002-026 (2002).
- [74] ATLAS Collaboration, *Detector and Physics Performance Technical Design Report*, CERN-LHCC/99-14/15.
- [75] J. Butterworth *et al.*, *Single Boson and Diboson Production in pp Collisions at $\sqrt{s} = 7\text{TeV}$* , ATL-COM-PHYS-2010-695 (2010).
- [76] G. Corcella *et al.*, *HERWIG 6.5: an event generator for Hadron Emission Reactions With Interfering Gluons (including supersymmetric processes)*, JHEP **01** (2001) 010.
- [77] E. Barberio and Z. Was, *PHOTOS - a universal Monte Carlo for QED radiative corrections: version 2.0*, Comp. Phys. Comm. **79** (1994) 291.
- [78] S. Jadach, Z. Was, R. Decker and J. H. Kuhn, *The τ decay library TAUOLA, version 2.4*, Comp. Phys. Comm. **76** (1993) 361.
- [79] ATLAS Collaboration, *Measurement of the cross section for jets produced in association with Z bosons*, ATL-COM-PHYS-2010-884 (2010).
- [80] B. P. Kersevan and E. Richter-Was, *The Monte Carlo event generator AcerMC versions 2.0 to 3.8 with interfaces to PYTHIA 6.4, HERWIG 6.5 and ARIADNE 4.1*, Comp. Phys. Comm. **184** **3** (2013) 919 – 985.
- [81] ATLAS Collaboration, *Measurement of the top quark-pair production cross section with ATLAS in pp collisions at $\sqrt{s} = 7 \text{ TeV}$* , Eur. Phys. J. C **71** (2011) 1577.

- [82] M. Smizanska, *PythiaB: An interface to Pythia6 dedicated to simulation of beauty events*, ATL-COM-PHYS-2003-038 (2003).
- [83] S. Alioli *et al.*, *NLO vector-boson production matched with shower in POWHEG*, JHEP **0807** (2008) 060.
- [84] ATLAS Collaboration, *Luminosity Determination in pp Collisions at $\sqrt{s} = 7$ TeV Using the ATLAS Detector at the LHC*, Eur. Phys. J. **C 71** (2011) 1630.
- [85] ATLAS Collaboration, *Luminosity Determination in pp Collisions at $\sqrt{s} = 7$ TeV using the ATLAS Detector in 2011*, ATLAS-CONF-2011-116 (2011).
<http://cdsweb.cern.ch/record/1376384>.
- [86] LHC Higgs Cross Section Working Group, S. Dittmaier, C. Mariotti, G. Passarino, and R. T. (Eds.), *Handbook of LHC Higgs Cross Sections: 2. Differential Distributions*, CERN-2012-002 (2012).
- [87] M. Seymour, *The Higgs boson line shape and perturbative unitarity*, Phys. Lett. **B 354** (1995) 409–414.
- [88] G. Passarino, C. Sturm, and S. Uccirati, *Higgs pseudo-observables, second Riemann sheet and all that*, Nucl. Phys. **B 834** (2010) 77–115.
- [89] S. Gorla and G. Passarino and D. Rosco, *The Higgs Boson Lineshape*, arXiv:1112.5517 (2011).
- [90] J. M. Campbell, R. Ellis, and C. Williams, *Gluon-gluon contributions to W^+W^- production and Higgs interference effects*, JHEP **10** (2011) 005.
- [91] ATLAS Collaboration, *Further ATLAS tunes of PYTHIA6 and Pythia 8*, ATL-PHYS-PUB-2011-014 (2011). <https://cdsweb.cern.ch/record/1400677>.
- [92] P. Z. Skands, *Tuning Monte Carlo Generators: The Perugia Tunes*, Phys. Rev. D **82** (2010) 074018.
- [93] ATLAS Collaboration, *Muon Momentum Resolution in First Pass Reconstruction of pp Collision Data Recorded by ATLAS in 2010*, ATLAS-CONF-2011-046.
- [94] ATLAS Collaboration, *Jet energy resolution and selection efficiency relative to track jets from in-situ techniques with the ATLAS Detector Using Proton-Proton Collisions at a Center of Mass Energy $\sqrt{s} = 7$ TeV*, ATLAS-CONF-2010-054 (2010).

- [95] ATLAS Collaboration, *Commissioning of the ATLAS high-performance b-tagging algorithms in the 7 TeV collision data*, ATLAS-CONF-2011-102 (2011).
- [96] G. Cowan, K. Cranmer, E. Gross, and O. Vitells, *Asymptotic formulae for likelihood-based tests of new physics*, Eur. Phys. J. C **71** (2011) 1554.
- [97] L. Moneta *et al.*, *The RooStats Project*, PoS **ACAT2010** (2010) 057.
- [98] ATLAS Collaboration, *An update to the combined search for the Standard Model Higgs boson with the ATLAS detector at the LHC using up to 4.9 fb⁻¹ of pp collision data at $\sqrt{s} = 7$ TeV*, ATLAS-COM-CONF-2012-039 (2012).
- [99] ATLAS Collaboration, *Observation of a new particle in the search for the Standard Model Higgs boson with the ATLAS detector at the LHC*, Phys. Lett. **B716** (2012) 1–29.
- [100] CMS Collaboration, *Observation of a new boson at a mass of 125 GeV with the CMS experiment at the LHC*, Phys. Lett. **B716** (2012) 30–61.
- [101] G. Belanger *et al.*, *Status of Invisible Higgs decays*, arXiv:1302.5694 (2012).
- [102] LEP Higgs Working Group, *Searches for Invisible Higgs bosons: Preliminary combined results using LEP data collected at energies up to 209 GeV*, LHWG Note 2001-06.
- [103] ALEPH Collaboration, *Determination of the number of light neutrino species*, Phys. Letters B, 231, 4, 519-529.
- [104] M. Bahr *et al.*, *Herwig++ Physics and Manual*, Eur. Phys. J. C **58** (2008) 639.
- [105] T. Gleisberg, S. Hoche, F. Krauss, M. Schonherr, S. Schumann, F. Siegert, and J. Winter, *Event generation with Sherpa 1.1*, JHEP **0902** (2009) 007.
- [106] ATLAS Collaboration, *Jet energy scale and its systematic uncertainty in proton-proton collisions at $\sqrt{s}=7$ TeV with ATLAS 2011 data*, ATLAS-CONF-2013-004 (2013).
- [107] M. Ciccolini, A. Denner and S. Dittmaier, *Strong and electroweak corrections to the production of Higgs+2 jets via weak interactions at the LHC*, Phys. Rev. Lett. **99** (2007) 161803.
- [108] ATLAS Collaboration, *Search for the Standard Model Higgs boson produced in association with a vector boson and decaying to bottom quarks with the ATLAS detector*, ATLAS-CONF-2012-161 (2012).

- [109] ATLAS Collaboration, *Combined measurements of the mass and signal strength of the Higgs-like boson with the ATLAS detector using up to 25 fb^{-1} of proton-proton collision data*, ATLAS-CONF-2013-014 (2013).
- [110] CMS Collaboration, *Updated measurements of the Higgs boson at 125 GeV in the two photon decay channel*, CMS-PAS-HIG-13-001 (2013).
- [111] CMS Collaboration, *Properties of the Higgs-like boson in the decay H to ZZ to $4l$ in pp collisions at $\sqrt{s} = 7$ and 8 TeV* , CMS-PAS-HIG-13-002 (2013).
- [112] CMS Collaboration, *Evidence for a particle decaying to W^+W^- in the fully leptonic final state in a standard model Higgs boson search in pp collisions at the LHC*, CMS-PAS-HIG-13-003 (2013).
- [113] CMS Collaboration, *Search for the Standard-Model Higgs boson decaying to tau pairs in proton-proton collisions at $\sqrt{s} = 7$ and 8 TeV* , CMS-PAS-HIG-13-004 (2013).
- [114] CMS Collaboration, *Search for the standard model Higgs boson produced in association with W or Z bosons, and decaying to bottom quarks for LHCp 2013*, CMS-PAS-HIG-13-012 (2013).
- [115] ATLAS Collaboration, *Search for the bb decay of the Standard Model Higgs boson in associated W/ZH production with the ATLAS detector*, ATLAS-CONF-2013-079 (2013).
- [116] CMS Collaboration, *Combination of standard model Higgs boson searches and measurements of the properties of the new boson with a mass near 125 GeV*, CMS-PAS-HIG-13-005 (2013).
- [117] ATLAS Collaboration, *Evidence for the spin-0 nature of the Higgs boson using ATLAS data*, arXiv:1307.1432 [hep-ex].
- [118] CMS Collaboration, *Study of the Mass and Spin-Parity of the Higgs Boson Candidate Via Its Decays to Z Boson Pairs*, Phys.Rev.Lett. **110** (2013) 081803, arXiv:1212.6639 [hep-ex].